



Determination of the Accommodation Coefficient Using Vapor/Gas Bubble Dynamics in an Acoustic Field

Nail A. Gumerov, Chao-Tsung Hsiao, and Alexei G. Goumilevski
DYNAFLOW, Inc., Fulton, Maryland

Prepared under Contract NAS3-98094

National Aeronautics and
Space Administration

Glenn Research Center

Acknowledgments

The authors would like to recognize the contributions of many colleagues at DYNAFLOW, Inc., to the success of the efforts described in this report. More particularly, Dr. Georges L. Chahine, the President of DYNAFLOW, whose thoughtful comments and advice were very helpful for the progress of the project, and Dr. Kenneth M. Kalumuck, whose discussions and comments helped in better understanding of the phenomena considered. The funding support of the National Aeronautics and Space Administration via award NAS3-98094, Dr. Jeff Allen monitor, is also gratefully acknowledged.

Available from

NASA Center for Aerospace Information
7121 Standard Drive
Hanover, MD 21076
Price Code: A06

National Technical Information Service
5285 Port Royal Road
Springfield, VA 22100
Price Code: A06

Available electronically at <http://gltrs.grc.nasa.gov/GLTRS>

Contents

List of Figures	v
I. Project Summary	1
1. Research Objectives	1
2. Summary of Research	1
3. Problems and Future R&D Objectives	2
4. Potential Applications	3
II. Introduction	5
1. Historical review of measurements of the accommodation coefficient	7
2. Review of publications related to vapor bubble dynamics	8
III. Statement of the Problem	11
1. Model of Vapor-Gas Bubble in Isotropic Acoustic Field	11
2. Model of Vapor Bubble in Isotropic Acoustic Field	14
3. Model of Small Bubble in Standing Acoustic Wave	16
4. Vapor-Gas Bubble Equilibrium in the Absence of an Acoustic Field	17
5. Length Scales and Dimensionless Equations	19
IV. Multiscale Technique For Bubbles in Isotropic Fields	21
1. Transformation of Variables	21
2. Solution of Thermal Problems	23
3. Complex Amplitudes	25
4. Evolution in Slow Time Scales	28
5. First Order Approximation	29
6. Equation for Rectified Heat Transfer in the Second Order Approximation	30
7. Third Order Approximation	31
a. Spatial Matching of Asymptotic Expansions	31
b. Equation for Rectified Heat Transfer	33

c.	Thin Boundary Layers	34
8.	Vapor-Gas Bubbles	35
a.	Thermal and Diffusion Problems	35
b.	Equations for Complex Amplitudes	37
V.	Asymptotic Technique For Standing Waves	39
1.	Asymptotic Expansions	39
2.	Evolution in Slow Time Scales	41
3.	Linear Approximation	43
4.	Equation for Rectified Heat Transfer	44
VI.	Numerical Methods	47
1.	Straight-Forward Finite Difference Scheme	47
2.	Numerical-Analytical Method	50
3.	Analytical Solutions	52
4.	Comparisons of Bubble Dynamics Computed by Various Methods	53
VII.	Analysis of Linear Bubble Dynamics in Acoustic Fields	57
1.	Vapor Bubbles	57
2.	Vapor-Gas Bubbles	61
VIII.	Analysis of Nonlinear Bubble Dynamics in Isotropic Acoustic Fields	77
1.	The Equilibrium Radius and Its Stability	77
2.	Results of Computations	78
IX.	Analysis of Nonlinear Bubble Dynamics in Standing Acoustic Waves	91
1.	Zero Gravity Conditions	91
a.	Saturated Liquids	92
b.	Superheated Liquids	92
c.	Subcooled Liquids	93
2.	Effects of Gravity	93
X.	Conclusions	103
	Bibliography	105

List of Figures

II-1	The ratio of the maximum to the minimum measured values of the accommodation coefficient for five different substances.	8
VI-1	Typical temperature profile inside ($\eta < 1$) and outside ($\eta > 1$) a vapor bubble oscillating in an acoustic field. The dots on the curve correspond to nodes of the computational grid.	50
VI-2	Comparison between computations based on the asymptotic theory with the initial quasisteady temperature profile in the liquid (the lower solid curve), initial uniform temperature profile in the liquid (the upper solid curve), and the numerical results of Hao & Prosperetti (1999) (the dashed curve), which are on top of our results using the purely numerical method and quasi-equilibrium scheme of phase transitions. The bubble radius is normalized with the primary resonance radius, 2.71 mm. The initial mean radius in the computations using the present theory is 0.1 mm.	54
VI-3	Comparisons of computations using the purely numerical method (the dashed curve), numerical-analytical method (the thick solid curve), and the third-order analytical solution (the thin solid curve).	54
VI-4	Comparison between computations using the third order asymptotic theory with the initial temperature jump ($\Phi_{200} = \Phi_{20}(a_{in})$, $a_{in} = 98 \mu\text{m}$; the solid curves) and purely numerical simulations with the initial bubble radius $100 \mu\text{m}$ using the detailed equations (the gray region and the dashed curve). Letters L, M, and U near the curves relates to the lower, mean, and upper slowly changing bubble radius. The curves L and U were computed by addition and subtraction of the amplitude of bubble oscillation predicted by the linear theory. The numerical-analytical method gives results close to the straight-forward computations.	55
VI-5	Comparison between the purely (the dashed curve) and the numerical-analytical method (the solid curve). The other notations and computation parameters correspond to the case shown in the previous figure.	55
VII-1	Relative amplitude of the forced vapor bubble radial oscillation in a 60 kHz acoustic field. The numbers near the curves show the values of the accommodation coefficient, β . The curve marked as "equilibrium" is computed using the quasi-equilibrium scheme of phase transition.	59
VII-2	Phase shift between the driving pressure and forced radial bubble oscillation. Notations are the same as in the previous figure.	59

VII-3	The vapor bubble natural frequency vs the bubble mean radius in an acoustic field at various values of the accommodation coefficient. The curve 'e' corresponds to the quasi-equilibrium scheme of phase transitions.	60
VII-4	Temperature profiles predicted by the linear theory at various values of the accommodation coefficient shown near the curves and the quasi-equilibrium phase transition, marked as "equilibrium". Profiles are computed for a vapor bubble of radius $50\mu\text{m}$ at the phase of oscillation corresponding to $t = 0$	60
VII-5	Relative amplitude of the forced vapor-gas bubble radial oscillation for $10\mu\text{m}$ bubble in water as a function of the acoustic frequency. The numbers near the curves show the value of the inert gas concentration inside the bubble.	65
VII-6	Phase shift between the driving pressure and the forced vapor-gas bubble radial oscillation for $10\mu\text{m}$ bubble in water as a function of the acoustic frequency. The numbers near the curves show the value of the inert gas concentration inside the bubble.	65
VII-7	Relative amplitude of the forced vapor-gas bubble radial oscillation in 1 kHz acoustic field as a function of the bubble radius. The numbers near the curves show the value of the inert gas concentration inside the bubble.	66
VII-8	Phase shift between the driving pressure and the forced vapor-gas bubble radial oscillation in 1 kHz acoustic field as a function of the bubble radius. The numbers near the curves show the value of the inert gas concentration inside the bubble.	66
VII-9	Relative amplitude of the forced vapor-gas bubble radial oscillation in 60 kHz acoustic field as a function of the bubble radius. The numbers near the curves show the value of the inert gas concentration inside the bubble.	67
VII-10	Phase shift between the driving pressure and the forced vapor-gas bubble radial oscillation in 60 kHz acoustic field as a function of the bubble radius. The numbers near the curves show the value of the inert gas concentration inside the bubble.	67
VII-11	Relative amplitude of the forced vapor-gas bubble radial oscillation for $10\mu\text{m}$ bubble in water as a function of the acoustic frequency. Computations are performed for different values of the inert gas accommodation coefficient, β_i , and the Henry constant, H (the values are shown near the curves). The thick curves marked 'equilibrium' correspond to quasi-equilibrium phase transition of the inert component.	68
VII-12	Phase shift between the driving pressure and the forced vapor-gas bubble radial oscillation for $10\mu\text{m}$ bubble in water as a function of the acoustic frequency. Computations are performed for different values of the inert gas accommodation coefficient, β_i , and the Henry constant, H (the values are shown near the curves). The thick curves marked 'equilibrium' correspond to quasi-equilibrium phase transition of the inert component.	68
VII-13	Relative amplitude of the forced vapor-gas bubble radial oscillation in 60 kHz acoustic field as a function of the bubble radius. The numbers near the curves show the value of the vapor accommodation coefficient, β_v . The curves marked 'equilibrium' correspond to quasi-equilibrium phase transition of the vapor.	69

VII-14	Phase shift between the driving pressure and the forced vapor-gas bubble radial oscillation in 60 kHz acoustic field as a function of the bubble radius. The numbers near the curves show the value of the vapor accommodation coefficient, β_v . The curves marked 'equilibrium' correspond to quasi-equilibrium phase transition of the vapor.	69
VII-15	Relative amplitude of the forced vapor-gas bubble radial oscillation for 10 μm bubble in water as a function of the bubble radius. The numbers near the curves show the value of the vapor accommodation coefficient, β_v . The curves marked 'equilibrium' correspond to quasi-equilibrium phase transition of the vapor.	70
VII-16	Phase shift between the driving pressure and the forced vapor-gas bubble radial oscillation for 10 μm bubble in water as functions of the bubble radius. The numbers near the curves show the value of the vapor accommodation coefficient, β_v . The curves marked 'equilibrium' correspond to quasi-equilibrium phase transition of the vapor.	70
VII-17	Relative amplitude of the forced vapor-gas bubble radial oscillation for 20 μm bubble in 60 kHz acoustic field as a function of the vapor accommodation coefficient. The numbers near the curves show the value of the inert gas concentration.	71
VII-18	Phase shift between the driving pressure and the forced vapor-gas bubble radial oscillation for 20 μm bubble in 60 kHz acoustic field as functions of the vapor accommodation coefficient. The numbers near the curves show the value of the inert gas concentration.	71
VII-19	Relative amplitude of the forced vapor-gas bubble radial oscillation in 60 kHz acoustic field as functions of the vapor accommodation coefficient. The numbers near the curves show the mean bubble radius.	72
VII-20	Phase shift between the driving pressure and the forced vapor-gas bubble radial oscillation in 60 kHz acoustic field as functions of the vapor accommodation coefficient. The numbers near the curves show the mean bubble radius.	72
VII-21	Relative amplitude of the forced vapor-gas bubble radial oscillation for 20 μm bubble as a function of the vapor accommodation coefficient. The numbers near the curves show the frequency of the acoustic field.	73
VII-22	Phase shift between the driving pressure and the forced vapor-gas bubble radial oscillation for 20 μm bubble as a function of the vapor accommodation coefficient. The numbers near the curves show the frequency of the acoustic field.	73
VII-23	Relative amplitude of the forced vapor-gas bubble radial oscillation in 60 kHz acoustic field as a function of the bubble radius. The numbers near the curves show the value of the thermodiffusion coefficient k_c	74
VII-24	Phase shift between the driving pressure and the forced vapor-gas bubble radial oscillation in 60 kHz acoustic field as a function of the bubble radius. The numbers near the curves show the value of the thermodiffusion coefficient k_c	74
VII-25	Dimensionless perturbations of temperature profiles inside 50 μm vapor-gas bubble oscillating in 60 kHz acoustic field. Profiles correspond to times $\omega t = 2\pi n$. The numbers near the curves show the value of the thermodiffusion coefficient k_c	75

VII-26	Dimensionless perturbations of inert gas concentration profiles inside 50 μm vapor-gas bubble oscillating in 60 kHz acoustic field. Profiles correspond to times $\omega t = 2\pi n$. The numbers near the curves show the value of the thermodiffusion coefficient k_c	75
VIII-1	Dependence of the growth rate of the vapor bubble on its radius for saturated water. The numbers near the curves show the values of the accommodation coefficient, β . The curve marked as "equilibrium" is computed using the quasiequilibrium scheme of phase transition.	82
VIII-2	The vapor bubble mean growth rate in an acoustic field as a function of the bubble current mean radius at various values of the accommodation coefficient (the second order theory).	82
VIII-3	Relation between the pressure amplitude and the equilibrium mean radius a_* for saturated water. The numbers near the curves show the values of the accommodation coefficient, β . The curve marked as "equilibrium" is computed using the quasi-equilibrium scheme of phase transition.	83
VIII-4	Relation between the pressure amplitude and the equilibrium mean radius a_* for saturated water for 1 kHz, 10 kHz, and 100 kHz acoustic fields and for two values of the accommodation coefficient shown near the curves.	83
VIII-5	Relation between the pressure amplitude and the steady radius a_* for saturated ($\Delta p = 0$) and subcooled ($\Delta p = 0.003$ bar) liquid helium for 100 kHz, 1 MHz, and 10 MHz acoustic fields.	84
VIII-6	Relation between the pressure amplitude and the equilibrium mean radius a_* for subcooled water. The numbers near the curves show the values of the accommodation coefficient, β . The curve marked as "equilibrium" is computed using the quasi-equilibrium scheme of phase transition. The thick lines correspond to the stable equilibrium mean radius while the thin lines show the unstable (threshold) equilibrium mean radius. The dotted line ($P_A = 0.12$ atm) intersects each plotted curve at 2 points, except the curve for $\beta = 1$, which is intersected at 4 points. . .	84
VIII-7	Relation between the pressure amplitude and the equilibrium mean radius a_* for superheated water. The numbers near the curves show the values of the accommodation coefficient, β . The curve marked as "equilibrium" is computed using the quasi-equilibrium scheme of phase transition.	85
VIII-8	Relation between the pressure amplitude and the equilibrium mean radius a_* for superheated water. The numbers near the curves show the values of the accommodation coefficient, β . The curve marked as "equilibrium" is computed using the quasi-equilibrium scheme of phase transition. The thick lines correspond to the stable equilibrium mean radius while the thin lines show the unstable (threshold) equilibrium mean radius. The dotted line ($P_A = 0.15$ atm) intersects each plotted curve at 3 points, except of the curve for $\beta = 0.04$, which is intersected at 1 point. . .	85
VIII-9	Dynamics of bubbles of various initial radii in superheated water at $\beta = 0.01$. The second order theory.	86
VIII-10	Dynamics of bubbles of various initial radii in superheated water at $\beta = 1$. The second order theory.	86

VIII-11	Function $\Phi_{20}(a_0)$ describing initial conditions for the rate of the mean bubble radius growth in the third order approximation at various values of the accommodation coefficient indicated near the curves.	87
VIII-12	The vapor bubble dynamics in an acoustic field at various values of the accommodation coefficient (the third-order theory). The initial radius in all cases was 50 μm	87
VIII-13	Dynamics of the mean vapor bubble radius in water with different initial temperature profiles near the bubble, Φ_{200} , and different initial radii, a_{in} , shown near the curves. The thick lines correspond to the temperature jump at $t = 0$ ($\Phi_{200} = \Phi_{20}(a_{in})$) while the thin lines correspond to the initial quasi-steady temperature profiles near the bubble ($\Phi_{200} = 0$).	88
VIII-14	The dynamics of the mean (period-averaged) vapor bubble radius in an acoustic field at various values of the accommodation coefficient and initial temperature profiles in the liquid. The third order theory for initial quasisteady temperature fields provide the same curves as the second order theory. The asymptotes show a two-term asymptotic expansion near the equilibrium mean radius.	88
VIII-15	Temperature profiles in the liquid during rectified heat transfer (third-order theory, numerical results). The numbers near the curves correspond to the number of cycles of bubble oscillation. The dashed curve shows a hyperbolic profile $(\Psi(a_0) - T_\infty)/\eta$ for $\Psi(a_0)$ at the millionth period of oscillation.	89
VIII-16	Dynamics of the mean vapor bubble radius in liquid helium with different initial temperature profiles near the bubble, Φ_{200} , and different initial radii, a_{in} , shown near the curves. The thick lines correspond to the temperature jump at $t = 0$ ($\Phi_{200} = \Phi_{20}(a_{in})$) while the thin lines correspond to the initial quasi-steady temperature profiles near the bubble ($\Phi_{200} = 0$).	89
IX-1	The amplitudes of 1 kHz and 100 kHz isotropic acoustic fields at which a bubble can experience steady (stable or unstable) oscillations for water at $\beta = 0.04$ and $T = 373$ K.	94
IX-2	The regions of A- and V-stability of bubbles at zero gravity for saturated, superheated, and subcooled water at $\beta = 0.04$ and $T = 373$ K.	95
IX-3	The phase trajectories for saturated water at 0g, $\beta = 0.04$ and $T = 373$ K. 10 kHz acoustic field, $\epsilon = 0.099$	95
IX-4	The phase trajectories for superheated water at 0g, $\Delta p = -0.01$ atm, $\beta = 0.04$ and $T = 373$ K. 60 kHz acoustic field, $\epsilon = 0.123$	95
IX-5	The phase trajectories for subcooled water at 0g, $\Delta p = 0.02$ atm, $\beta = 0.04$ and $T = 373$ K. 1 kHz acoustic field, $\epsilon = 0.088$	96
IX-6	The bubble dynamics corresponding to a phase trajectory from Figure 3.	96
IX-7	The bubble dynamics corresponding to phase trajectories from Figure 4.	96
IX-8	The bubble dynamics corresponding to phase trajectories from Figure 5.	97
IX-9	The phase trajectories for subcooled water at 0.05g, $\Delta p = 0.02$ atm, $\beta = 0.04$ and $T = 373$ K. 1 kHz acoustic field, $\epsilon = 0.088$	97
IX-10	The phase trajectories for subcooled water at 1g, $\Delta p = 0.02$ atm, $\beta = 0.04$ and $T = 373$ K. 1 kHz acoustic field, $\epsilon = 0.088$	97

IX-11	The bubble dynamics in subcooled water at various levels of gravity $\Delta p = 0.02$ atm, $\beta = 0.04$ and $T = 373$ K. 1 kHz acoustic field, $\epsilon = 0.088$	98
IX-12	The phase trajectories for saturated water at 0.05g, $\beta = 0.04$ and $T = 373$ K. 10 kHz acoustic field, $\epsilon = 0.099$	98
IX-13	The phase trajectories for saturated water at 0.1g, $\beta = 0.04$ and $T = 373$ K. 10 kHz acoustic field, $\epsilon = 0.099$	98
IX-14	The phase trajectories for saturated water at 1g, $\beta = 0.04$ and $T = 373$ K. 10 kHz acoustic field, $\epsilon = 0.099$	99
IX-15	The bubble dynamics in saturated water at various levels of gravity, $\beta = 0.04$ and $T = 373$ K. 1 kHz acoustic field, $\epsilon = 0.088$	99
IX-16	Dynamics of a vapor bubble in a standing acoustic wave at different values of the accommodation coefficient and normal gravity conditions.	100
IX-17	Dynamics of a vapor bubble in a standing acoustic wave at different values of the accommodation coefficient and reduced gravity conditions.	100
IX-18	Dynamics of a vapor bubble in a standing acoustic wave at different values of the accommodation coefficient and zero gravity conditions.	101

Chapter I.

Project Summary

1. Research Objectives

The ultimate goal of the project is to theoretically investigate the effect of nonequilibrium phase transitions on vapor and vapor-gas bubble dynamics in acoustic fields to determine the feasibility of the measurement of the accommodation coefficient using bubble dynamics in acoustic fields. The technical objectives include:

- 1. Using a spherical model of a bubble in an isotropic acoustic field including thermal and diffusion effects in the liquid and in the vapor, surface tension, liquid viscosity and compressibility, evaluate the effect of nonequilibrium phase transitions on vapor and vapor-gas bubble dynamics.*
- 2. Evaluate the influence of the accommodation coefficient on the bubble translational motion in a standing acoustic waves and on rectified heat transfer.*
- 3. Conduct a parametric study to evaluate the range of parameters which can be used in design of an experimental setup for determination of the accommodation coefficient.*

2. Summary of Research

The research effort has successfully achieved most the objectives set in the proposal:

- We developed a comprehensive model of a spherical bubble in an acoustic field including the effects of nonequilibrium phase transitions, heat and mass transfer in the liquid and gaseous phases, surface tension, liquid viscosity, and compressibility.
- We developed and implemented asymptotic and numerical methods for solution of the problem and incorporated them into codes convenient for parametric studies.
- We conducted parametric studies of vapor and vapor-gas bubble dynamics in acoustic fields and determined conditions in which the effect of nonequilibrium phase transitions on bubble dynamics is appreciable and can be used for measurements of the accommodation coefficient.

- We uncovered several physical effects which can be used for determination of the accommodation coefficient using bubble dynamics. These include, for example, low frequency bubble mean position/radius oscillations in standing acoustic waves, the possibility of stabilization of the mean bubble radius in acoustic fields, the existence of multiple threshold and stable equilibrium states of the mean vapor bubble radius in acoustic fields and their dependence on the accommodation coefficient, parameters of the acoustic field, and ambient conditions.
- It is commonly thought that nonequilibrium phase transition affects bubble dynamics only in high-frequency fields (at least tens of kilohertz for water; some authors considered even the megahertz range). We, however, found that the range of bubble dynamics sensitivity depends on the bubble size, initial conditions, content of the inert component, and other parameters, which can be selected in experiments to provide measurements over a broad range of acoustic frequencies, and ambient conditions. We found that nonequilibrium phase transitions may affect the dynamics of vapor and vapor-gas bubbles in a broad range of acoustic frequencies and bubble sizes (for water at atmospheric pressure, 1-100 kHz and 10-10000 μm , respectively).
- We found a strong effect of initial conditions on rectified heat transfer for an initial stage that can span millions of cycles of bubble oscillations.
- We found that gravity can substantially affect the bubble dynamics in acoustic fields. Regimes of bubble dynamics in standing waves substantially depend on the magnitude of gravity. Reduced gravity in general is beneficial for measurements of the accommodation coefficient.

3. Problems and Future R&D Objectives

The following research issues still need to be addressed prior to designing an instrument for measurement of the accommodation coefficient.

1. Validation of the developed codes by comparison with available experimental data.
2. Modification of the developed codes to include convective heat transfer due to bubble translational motion in a standing wave.
3. In the space of parameters, determination of the regions of spherical shape stability/applicability of the spherical bubble theory.
4. Evaluation of the effect of bubble nonsphericity on the measurements of the accommodation coefficient.
5. Determination of the optimal parameters/regimes for measurement of the accommodation coefficient.

4. Potential Applications

The research seeks to develop a practical diagnostic technique for measurement of the accommodation coefficient of various substances in various conditions. The technique is based on measurements of bubble size and position in acoustic fields and subsequent processing of the results of measurements. Dependencies of the accommodation coefficient on temperature, surface contamination, and other parameters can be established using the proposed technique and utilized for diagnostic purposes and characterization of liquid/vapor interfaces. Measurement of the accommodation coefficient is important for proper modeling of many natural and technological processes including boiling of liquid metals, film boiling, vacuum vaporization, explosions, aerosol mechanics, meteorology, and others.

Chapter II.

Introduction

Nonequilibrium liquid/vapor phase transformations occur in a wide variety of natural and technological processes. In addition to the problem of interest here, these include evaporation and condensation of high velocity jets [8], film condensation [9], growth of small droplets in clouds [10, 11], sound propagation in vapor-droplet systems [12, 13], nonlinear dynamics of vapor bubbles and condensed droplets in acoustic fields [14, 2], and laser vaporization [15].

Studies of processes with non-equilibrium phase transitions are of great practical importance, because in many advanced technologies it is necessary to predict and control material behavior under extreme conditions. However, the use of most theories and models is limited by the lack of reliable data on material properties, especially coefficients describing nonequilibrium vapor/liquid transformations. Such data can be obtained only from experiments. The experimental facilities used for these measurements are usually complex, expensive, and do not provide repeatable results. For example, data reported on the accommodation coefficient for water obtained by various experimenters during this century vary from $6 \cdot 10^{-3}$ to 1, and experimental data for mercury are in the range from $5 \cdot 10^{-4}$ to 1.

The reason for such a wide range of results is that the accommodation coefficient is very sensitive to the conditions of the experiment. In order to address this shortcoming, the dependence of the accommodation coefficient on temperature, on the concentration of other species, and on other parameters near the interface should be determined. If a reliable and accurate accommodation coefficient measurement technique is available, such dependencies can be found experimentally and tabulated. This will provide a firm basis for modeling of nonequilibrium phase transitions.

In recent microgravity experiments conducted by the European Space Agency using the German drop tower and the Bubble, Drop, and Particle Unit ESA multi-user facility for fluid physics experiments operating onboard IML2 (1994) and LMS (1996), an attempt to determine of the accommodation coefficient of refrigerants R11 and R113 was made by Picker and Straub [16] using observation of vapor bubble dynamics. Typical times of bubble radius variations in these experiments were of order 1 s. These times are several orders of magnitude larger than the interface temperature relaxation times and the evaporation/condensation in these experiments occurred in almost equilibrium conditions (no dependence on the accommodation coefficient). This explains the great dispersion of the values obtained for the accommodation coefficient (from $0.9 \cdot 10^{-2}$ to 0.7 for R11 and from $8 \cdot 10^{-3}$ to 1 for R113 [16]).

It is known that during each cycle of bubble oscillation there are two phase transition stages: evaporation and condensation. For very small amplitude oscillations the amounts of evaporated and condensed liquid are approximately the same, and the vapor bubble oscillates about an equilibrium value. However, at larger amplitudes the nonlinearity of the bubble dynamics causes a difference between the amounts of evaporated and condensed liquid. This difference is small during one period of oscillation, but leads to slow-timescale dynamics of the average bubble size. This is called "rectified heat transfer". The same effect for gas bubbles growing due to mass diffusion is known in literature as "rectified diffusion". For vapor/gas bubbles it can be called "rectified heat and mass transfer". In some regimes the average bubble size can reach an equilibrium value, and the bubble can experience stable oscillations. In this state the amounts of evaporated and condensed liquid over the period are equal even when taking into account all nonlinear effects. The equilibrium mean radius can be defined as the mean radius separating ranges of bubble growth and shrinkage. The mean equilibrium radius can be stable (in this case bubbles of sizes slightly larger than the equilibrium radius shrink and bubbles slightly smaller than the equilibrium radius grow) or unstable (opposite situation). In a standing acoustic wave the bubble also experience a slow drift under the action of the primary Bjerknes force, which is also a nonlinear effect. The present study shows that the effects of bubble drift and rectified heat transfer are strongly coupled.

Accounting for these nonlinear effects in a measurement technique has additional advantages. First, these effects depend strongly on the value of the accommodation coefficient. Second, the characteristic times of the growth of the bubble average radius and of the bubble drift in weak acoustic fields are much larger than the bubble period of oscillation. Also the corresponding spatial scales (of the order of the bubble radius and the acoustic wavelength) are much larger than the amplitude of the bubble radius oscillations. This makes these measurement much easier to accomplish.

Successful completion of this effort will enable the refined theory and codes to be used for development of a simple system for measuring the accommodation coefficient. Such a system could be used not only in fundamental studies of kinetics of phase transitions, but also could have good practical applications, for example for detection of extremely small amounts of contaminants present in pure substances, because of the high sensitivity of the accommodation coefficient to the contaminants. To establish such procedures the dependence of the accommodation coefficient on various contaminants and ambient conditions should be determined first, which also requires a good measurement technique for this coefficient. There could be substantial benefits from using the accommodation coefficient measurement technique for controlling production of pure substances such as semi-conductors, high purity chemicals and isotopes. This technique can be modified for the case of arbitrary aggregate states of matter, and allows consideration of gas-solid, liquid-liquid and liquid-solid non-equilibrium phase transitions (e.g. the crystal growth from melts in acoustic fields under the effect of rectified heat transfer as was considered in [17]).

1. Historical review of measurements of the accommodation coefficient

The kinetic model of evaporation and condensation was first proposed by Hertz [18] and Knudsen [19]. If the difference between the saturation temperature T_s and the temperature of the interface T_a is not too large, the rate of evaporation ξ can be written in the form of the Hertz-Knudsen-Langmuir equation. The accommodation coefficient β is also known as the evaporation or the condensation coefficient. Some authors discriminate between the condensation and accommodation coefficient, while other authors use the same value for both terms. β is a dimensionless thermophysical parameter ranging from 0 to 1 which is a property of the liquid-gas interface (such as the surface tension coefficient).

The history of accommodation coefficient measurements shows many problems, as can be seen in the publications cited in this section and the fundamental monograph of Volmer [1]. All these works and the experimental data show a wide range of possible values of β and show the importance of considering the physicochemical hydrodynamics near surfaces where nonequilibrium condensation occurs. The following examples illustrate this point.

The first experiments of Hertz with mercury [18] gave the value $\beta = 0.11$. Knudsen [19] also experimented with mercury, and his first experiments gave the value $\beta = 0.0005$. He explained this low value of the accommodation coefficient by surface contamination. After improving the conditions of the same experiment he obtained $\beta = 0.11$. Finally, experimenting with falling mercury drops with continuously renewing surfaces he found $\beta = 1$.

Numerous experiments of Langmuir and coworkers performed between 1913 and 1934, showed that the accommodation coefficient for high temperature boiling metals such as wolfram, molybdenum, platinum, nickel, iron, copper, and silver is close to 1. Further analysis of these and other data showed that the value of β for all of the mentioned metals is between 0.25 and 0.33, except for platinum, for which $\beta = 1$ could be true.

The accommodation coefficient for water was measured in the studies of Alty and coworkers [20]. To determine the interface temperature they used a technique based on the measurement of the surface tension and found $\beta = 0.036$. In [9] the water accommodation coefficient was estimated from measurements of filmwise condensation of steam at low pressure on a vertical flat plate and β was found between 0.45 and 1. On the other hand, recent measurements of the water accommodation coefficient using a cooled wall expansion chamber [11] showed values of β that decreased from 1 for $1\ \mu\text{m}$ droplets to 0.006 for $15\ \mu\text{m}$ droplets. This, perhaps, could be due to some diffusion of trace contaminants or inert components to the surface. Nevertheless, the experimenters that took precautions to ensure system and sample purity were not able to identify trace contaminants. The authors of [21] also found a difference in the water accommodation coefficient between a fresh surface (measured β is 0.2) and a "stagnant" surface (measured β is 0.038).

In Fig. II-1 we present some reported data on accommodation coefficient measurements. We plotted the ratio of the maximum reported to the minimum reported value of the accommodation coefficient for five different substances. It is seen that these ratios can be of order 10^2 or even 10^3 .

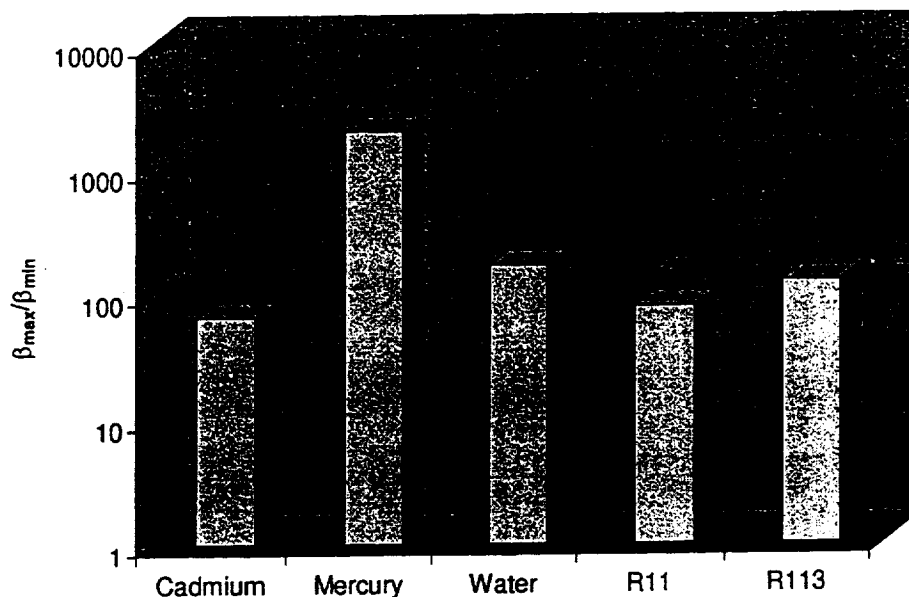


Figure II-1: The ratio of the maximum to the minimum measured values of the accommodation coefficient for five different substances.

2. Review of publications related to vapor bubble dynamics

The acoustics of vapor bubbles and acoustic vapor cavitation were intensively studied theoretically and experimentally in the 1960's and 1970's. Many of these studies were related to the design of cryogenic bubble chambers for registration of the tracks of charged particles [22] and measurements of the tensile strength of liquids [26]. More recent applications include acoustic enhancement of boiling in microgravity [27, 28] and the use of bubble dynamics for determination of liquid-vapor interface properties [4].

Wang [29], Khabeev [30], and Fanelli *et al* [31] performed linear analyses of forced vapor and vapor-gas bubble oscillations and showed a strong difference in acoustic properties of vapor bubbles and bubbles of non-condensable gas. In addition to the primary resonance, vapor bubbles exhibit a second resonance in acoustic fields corresponding to smaller sizes for a given frequency, which is known as the condensation-evaporation resonance. This resonance was first reported by Finch and Neppiras [32]. Hsieh [33], Marston [34], and Hao and Prosperetti [35] provided physical insight into the second resonance.

The effect of rectified heat transfer on vapor bubbles was investigated theoretically by several researchers [3, 5, 35, 36, 37, 39]. Marston and Greene [40] observed stable oscillations of bubbles for several seconds in liquid helium-I. Our recent study sponsored by NASA shows that there can exist multiple threshold and stable equilibrium mean radii of vapor bubbles in isotropic acoustic

waves [5]. Hao and Prosperetti [35] and our study [5] have determined that the development of a “slow” thermal boundary layer in the liquid at large time is a significant mechanism of rectified heat transfer. This means that convective heat transfer can be important for bubbles moving in the liquid. Theories and computational schemes for modeling such processes are available [41, 42, 43].

There are very few publications available on experimental studies of rectified heat transfer. For example, Akulichev *et al* [17] mention some experiments in cryogenic liquids without providing quantitative information. A very recent publication of Ohsaka and Trinh [44] reports results on water vapor bubble growth rate measurements, which perhaps is the first publication of such data. This paper shows that experiments with vapor bubbles in acoustic fields are challenging. Particularly, experiments for “vapor” bubbles were performed at atmospheric pressure and at a temperature of 80°C. Such bubbles consisted approximately of 40% water and 60% air (by weight). Our computations show that such bubbles differ from both pure air and pure vapor bubbles, and a theory of rectified heat and mass transfer to vapor-gas bubbles should be applied in this case.

The above mentioned theoretical studies deal with spherical bubbles. However, due to the parametric resonances between volume and shape modes, a stable spherical bubble shape can be realized only at small amplitudes [45, 46, 47]. Other effects, such as acoustic streaming, translatory bubble motion, and gravity, can also influence the results [48]. To describe shapes of levitating bubbles and drops in standing acoustic waves variational and other methods were applied (e.g. [49, 50]).

Forces acting on the bubble in acoustic fields were studied by several researchers. The major force acting on a bubble in an oscillating pressure field is the primary Bjerknes force [51], which is the time average over a period of the product of the bubble volume and the acoustic pressure gradient. This force is proportional to the energy of the acoustic field. In normal gravity conditions, depending on bubble size, frequency, and amplitude of sound, it can exceed the gravity force [52] and the bubble can levitate [53] or be positioned in the center of a spherical flask such as in sonoluminescence experiments [54]. Other important forces include the added mass force and viscous drag force.

Note that the value and sign of the primary Bjerknes force depend on the response of the bubble volume to the acoustic excitation. Since there exist a substantial difference in resonance properties of gas, vapor, and vapor/gas bubbles, the primary Bjerknes force is different for these three cases. At higher frequencies it depends on the kinetics of phase transition due to its influence on the bubble resonance [6]. Thus the model predicting acoustic forces on the bubble and the resulting bubble motion and shape deformations should include an accurate consideration of bubble forced oscillation including heat and mass transfer inside and outside the bubble, kinetics of phase transitions, liquid inertia, compressibility, viscosity, and surface tension.

Chapter III.

Statement of the Problem

We will consider the dynamics in acoustic fields of a bubble filled with the vapor of the host liquid or a mixture of the vapor and an inert gas. We consider that the boiling point of the inert gas corresponds to substantially lower temperature than the liquid temperature at the same pressure. A mixture of water vapor and air is an example of a such system. We also consider two configurations of the acoustic field: a) an isotropic field; b) a standing wave.

1. Model of Vapor-Gas Bubble in Isotropic Acoustic Field

Consider a spherically-symmetric model of a vapor-gas bubble in an isotropic pressure field, with the wavelength much larger than the bubble size, $\omega a \ll C$, where ω is the circular frequency, a is the bubble radius, and C is the speed of sound in the liquid. For a viscous liquid and inviscid gas the mass, momentum, and energy conservation equations at the interface can be written in the form [38, 58, 59]:

$$\rho_l (\dot{a} - w_{la}) = \rho_{ga} (\dot{a} - w_{ga}) = \xi, \quad \xi = \xi_v + \xi_i, \quad (\text{III-1})$$

$$\Pi_{la}^{rr} = -p_g + \xi (w_{ga} - w_{la}) + 2\frac{\sigma}{a}, \quad (\text{III-2})$$

$$\Pi_{la}^{rr} w_{la} - q_{la} + \frac{1}{2} \xi w_{la}^2 = -p_g w_{ga} - q_{ga} + \frac{1}{2} \xi w_{ga}^2 + \xi_v l_v + \xi_i l_i + \dot{\sigma} + \frac{2\sigma \dot{a}}{a}. \quad (\text{III-3})$$

Here ρ, w , and q are the density, radial velocity, and heat flux, p and Π^{rr} are the pressure and radial component of the stress tensor, and ξ, σ , and l are the rate of phase transition from liquid to gas, surface tension, and heat of phase transformation. Subscripts l and g refer to liquid and gas, respectively, and subscript a denotes parameters on the interface. We assume that the gas consists of two components, vapor and inert gas, which parameters are marked with subscripts v and i .

The dynamic equation describing forced radial oscillation of a bubble of variable mass bubble

in slightly compressible liquid can be found in [60, 5]:

$$\begin{aligned} & \left(1 - \frac{w_{la}}{C}\right) a \dot{w}_{la} + 2 \left(1 - \frac{w_{la}}{4C}\right) \dot{a} w_{la} - \frac{1}{2} w_{la}^2 \\ &= -\frac{1}{\rho_l} \left(1 + \frac{\dot{a}}{C} + \frac{a}{C} \frac{d}{dt}\right) \left[\Pi_{la}^{rr} + p_\infty(t) + \frac{4}{a} \mu_l w_{la}\right]. \end{aligned} \quad (\text{III-4})$$

Here μ_l is the liquid viscosity and $p_\infty(t)$ is the forcing pressure.

In the general model we accept that the gaseous phase is a perfect gas mixture described by the following thermodynamic relations:

$$\mu_i = RT_g \ln p_i, \quad \mu_v = RT_g \ln p_v, \quad \mu_g = \mu_i - \mu_v, \quad (\text{III-5})$$

$$p_i = \rho_i R_i T_g, \quad p_v = \rho_v R_v T_g, \quad p_g = p_v + p_i, \quad (\text{III-6})$$

$$c_i = \frac{\rho_i}{\rho_g}, \quad c_v = \frac{\rho_v}{\rho_g}, \quad \rho_g = \rho_v + \rho_i, \quad c_i + c_v = 1, \quad (\text{III-7})$$

$$R_i = R/M_i, \quad R_v = R/M_v, \quad R_g = c_i R_i + c_v R_v. \quad (\text{III-8})$$

Here μ is the chemical potential, T the temperature, c the mass concentration, R the gas constant, and M the molecular weight.

The resulting mass fluxes of the components from the liquid to gaseous phase, ξ , at the constant interface temperature T_a can be described by [1]:

$$\begin{aligned} \xi_i &= \xi_i^{(l \rightarrow g)} - \xi_i^{(g \rightarrow l)} = \frac{\beta_i^{(l \rightarrow g)}}{\sqrt{2\pi R_i T_a}} \exp \frac{\mu_i^l(T_a)}{RT_a} - \frac{\beta_i^{(g \rightarrow l)}}{\sqrt{2\pi R_i T_a}} \exp \frac{\mu_i(T_a)}{RT_a}, \\ \xi_v &= \xi_v^{(l \rightarrow g)} - \xi_v^{(g \rightarrow l)} = \frac{\beta_v^{(l \rightarrow g)}}{\sqrt{2\pi R_v T_a}} \exp \frac{\mu_v^l(T_a)}{RT_a} - \frac{\beta_v^{(g \rightarrow l)}}{\sqrt{2\pi R_v T_a}} \exp \frac{\mu_v(T_a)}{RT_a}, \end{aligned}$$

where β are the proportion coefficients and the superscripts near j and β denote the direction of the mass flux. At thermodynamic equilibrium, $j_g = j_v = 0$, $p_v = p_{vs}(T_a)$, and $p_i = c_{ia}H$. Thus $\beta_i^{(l \rightarrow g)} = \beta_i^{(g \rightarrow l)} = \beta_i$ and $\beta_v^{(l \rightarrow g)} = \beta_v^{(g \rightarrow l)} = \beta_v$. Using the above expressions for the fluxes and chemical potentials we have

$$\xi_i = \frac{\beta_i}{\sqrt{2\pi R_i T_a}} [c_{ia}H(T_a) - p_{ia}], \quad \xi_v = \frac{\beta_v}{\sqrt{2\pi R_v T_a}} [p_{vs}(T_a) - p_{va}]. \quad (\text{III-9})$$

The last relation is the well-known Hertz-Knudsen-Langmuir equation describing non-equilibrium evaporation of a one-component liquid [1]. The coefficient β_v is the vapor accommodation (condensation) coefficient and can be treated as the fraction of vapor molecules hitting the interface which condense. By analogy β_i can be called 'inert gas accommodation coefficient' and can be measured from experiments on nonequilibrium dissolving.

From a linear analysis described in Chapter 4 and in Chapter 7 we found that Henry's law,

$$p_{ia} = c_{ia}H, \quad (\text{III-10})$$

is applicable for description of bubble dynamics over a broad range of frequencies, while for the vapor component the nonequilibrium evaporation/condensation is important.

For spatially uniform pressure the diffusion flux of the inert component, j_g , and the heat flux, q_g , can be expressed according to [56]:

$$j_g = -\rho_g D_g \left(\frac{\partial c_i}{\partial r} + \frac{k_T}{T_g} \frac{\partial T_g}{\partial r} \right), \quad q_g = -\lambda_g \frac{\partial T_g}{\partial r} + k_c C_{pg} T_g j_g, \quad (\text{III-11})$$

$$k_c = \frac{1}{C_{pg} T_g} \left[k_T \left(\frac{\partial \mu_g}{\partial c_i} \right)_{p_g, T_g} - T_g \left(\frac{\partial \mu_g}{\partial T_g} \right)_{p_g, c_i} + \mu_g \right] = \frac{k_T R}{c_i c_v C_{pg}}, \quad (\text{III-12})$$

where D and λ are the mass diffusivity and thermal conductivity, k_T is the thermal-diffusion ratio, and C_{pg} is the gas specific heat at constant pressure and concentration. Expression (III-12) is obtained using the above model of the gaseous phase (III-5)-(III-8), where μ_g is considered as a function of p_g , T_g , and c_i . Note that in limiting case of one-component gas, $c_i c_v \rightarrow 0$, we have, $k_T \rightarrow 0$, while k_c remains to be a finite quantity. The quantities k_c or k_T can be found from corresponding tables or can be evaluated using the formulas following from the above definitions and found in Ref.[61]:

$$k_c = \frac{\alpha M_i}{M_i c_v + M_v c_i} \frac{R}{C_{pg}}, \quad \alpha = \frac{105 M_i - M_v}{118 M_i + M_v} k_T^0. \quad (\text{III-13})$$

where α is the thermal-diffusion constant, and k_T^0 has been evaluated for several intermolecular force-models. For rigid elastic spheres $k_T^0 = 1$ and we took this value for our computations. Details for computation of the thermal-diffusion ratio based on the first, second, and third order gas-kinetic theories can be found in Ref.[62].

Now we can represent the mass and energy conservation equations in the form:

$$\begin{aligned} \frac{\partial \rho_g}{\partial t} + \frac{1}{r^2} \frac{\partial}{\partial r} (r^2 \rho_g w_g) &= 0, \quad \rho_g \left(\frac{\partial c_i}{\partial t} + w_g \frac{\partial c_i}{\partial r} \right) = -\frac{1}{r^2} \frac{\partial}{\partial r} (r^2 j_g), \\ \rho_g C_{pg} \left(\frac{\partial T_g}{\partial t} + w_g \frac{\partial T_g}{\partial r} \right) - \dot{p}_g(t) &= -\frac{1}{r^2} \frac{\partial}{\partial r} (r^2 q_g). \end{aligned} \quad (\text{III-14})$$

In these equations we assume that the total gas pressure is spatially uniform, which is justifiable when the velocity of the bubble wall is much smaller than the speed of sound in the gas. Note that at the same time the partial pressures of the components depend on the radial coordinate due to dependence of the inert gas concentration on this coordinate.

Assuming that the mass concentration of the dissolved inert gas in the liquid is small, $c_l \ll 1$, we can neglect the effect of thermal diffusion in the liquid. The effect of barodiffusion is also negligible, since the liquid is almost incompressible. Therefore, we can represent the mass and energy conservation equations in the liquid in the form:

$$\rho_l \left(\frac{\partial c_l}{\partial t} + \frac{a^2 w_{la}}{r^2} \frac{\partial c_l}{\partial r} \right) = -\frac{1}{r^2} \frac{\partial}{\partial r} (r^2 j_l), \quad j_l = -\rho_l D_l \frac{\partial c_l}{\partial r}, \quad (\text{III-15})$$

$$\rho_l C_l \left(\frac{\partial T_l}{\partial t} + \frac{a^2 w_{la}}{r^2} \frac{\partial T_l}{\partial r} \right) = -\frac{1}{r^2} \frac{\partial}{\partial r} (r^2 q_l) + \frac{12 \mu_l w_{la}^2 a^4}{r^6}, \quad q_l = -\lambda_l \frac{\partial T_l}{\partial r}, \quad (\text{III-16})$$

where C_l is the liquid specific heat.

Assuming that the temperature jump at the interface is negligibly small (which is true for not too high rates of evaporation or condensation), the following boundary conditions can be imposed:

$$w_g|_{r=a} = w_{ga}, \quad T_g|_{r=a} = T_l|_{r=a} = T_a, \quad T_l|_{r=\infty} = T_\infty, \quad (\text{III-17})$$

$$c_i|_{r=a} = c_{ia}, \quad c_l|_{r=a} = c_{la}, \quad c_l|_{r=\infty} = c_\infty. \quad (\text{III-18})$$

The diffusion mass fluxes at the interface can be represented as

$$j_{ga} = c_{ia}\xi - \xi_i, \quad j_{la} = c_{la}\xi - \xi_i.$$

To specify $p_{vs}(T)$ the Clausius-Clapeyron equation can be used:

$$\frac{dp_{vs}}{dT} = \frac{l_v}{T} \left(\frac{1}{\rho_{vs}(T)} - \frac{1}{\rho_l} \right)^{-1}. \quad (\text{III-19})$$

where ρ_{vs} is the vapor density on the saturation line. In the present study for simplicity we neglect the dependence of σ , H , λ_g , λ_l , D_g , and D_l on the temperature.

Note that if the heat and mass fluxes are known, then these equations together with the Rayleigh-Plesset equation (III-4) form a closed system. These can be found by solving corresponding problems of heat and mass convective diffusion with boundary conditions c_{ia} and c_{la} for concentrations and T_a for temperatures inside and outside the bubble.

We also need to specify the function $p_\infty(t)$, which for an acoustic field of amplitude P_A and circular frequency ω can be written in the form

$$p_\infty(t) = p_{\infty 0} + \text{Re}\{P_A e^{i\omega t}\}. \quad (\text{III-20})$$

2. Model of Vapor Bubble in Isotropic Acoustic Field

The case of pure vapor bubbles is a limiting case of the vapor-gas bubbles at small concentrations of the inert gas. However, it is important to consider this case in parallel with the case of vapor-gas bubbles, due to substantial model simplifications that can be obtained for one-component bubbles. This limiting case can be used for verification of the general results for two-component systems. Simplifications for pure vapor bubbles compared to vapor-gas bubbles include:

- Simplification of kinetics of phase transitions;
- Simplification of bubble thermodynamics. Availability of a simplified energy integral for vapor;
- Absence of mass diffusion;
- Simplification of boundary conditions.

Equations describing the vapor bubble dynamics can be represented in the form:

$$\begin{aligned}\rho_l (\dot{a} - w_{la}) &= \rho_{va} (\dot{a} - w_{va}) = \xi, \\ \Pi_{la}^{rr} &= -p_v + \xi (w_{va} - w_{la}) + 2\frac{\sigma}{a},\end{aligned}\quad (\text{III-21})$$

$$\Pi_{la}^{rr} w_{la} - q_{la} + \frac{1}{2} \xi w_{la}^2 = -p_v w_{va} - q_{va} + \frac{1}{2} \xi w_{va}^2 + \xi l_v + \dot{\sigma} + \frac{2\sigma \dot{a}}{a}. \quad (\text{III-22})$$

$$\begin{aligned}&\left(1 - \frac{w_{la}}{C}\right) a \dot{w}_{la} + 2 \left(1 - \frac{w_{la}}{4C}\right) \dot{a} w_{la} - \frac{1}{2} w_{la}^2 \\ &= -\frac{1}{\rho_l} \left(1 + \frac{\dot{a}}{C} + \frac{a}{C} \frac{d}{dt}\right) \left[\Pi_{la}^{rr} + p_\infty(t) + \frac{4}{a} \mu_l w_{la}\right].\end{aligned}\quad (\text{III-23})$$

$$p_v = \rho_v R_v T_g, \quad (\text{III-24})$$

$$\xi_v = \frac{\beta_v}{\sqrt{2\pi R_v T_a}} [p_{vs}(T_a) - p_{va}], \quad (\text{III-25})$$

$$\begin{aligned}&\frac{\partial \rho_v}{\partial t} + \frac{1}{r^2} \frac{\partial}{\partial r} (r^2 \rho_v w_v) = 0, \\ &\rho_v C_{pv} \left(\frac{\partial T_v}{\partial t} + w_v \frac{\partial T_v}{\partial r}\right) - \dot{p}_v(t) = -\frac{1}{r^2} \frac{\partial}{\partial r} (r^2 q_v), \quad q_v = -\lambda_v \frac{\partial T_v}{\partial r},\end{aligned}\quad (\text{III-26})$$

$$\rho_l C_l \left(\frac{\partial T_l}{\partial t} + \frac{a^2 w_{la}}{r^2} \frac{\partial T_l}{\partial r}\right) = -\frac{1}{r^2} \frac{\partial}{\partial r} (r^2 q_l) + \frac{12\mu_l w_{la}^2 a^4}{r^6}, \quad q_l = -\lambda_l \frac{\partial T_l}{\partial r}, \quad (\text{III-27})$$

$$w_v|_{r=a} = w_{va}, \quad T_v|_{r=a} = T_l|_{r=a} = T_a, \quad T_l|_{r=\infty} = T_\infty. \quad (\text{III-28})$$

Since for one-component bubble content the pressure of the vapor is spatially uniform (for a two component system the inert gas and the vapor pressure are not uniform due to gradients of concentration) the equations for vapor inside the bubble have the following integrals [59, 57, 63]:

$$w_v = \frac{(\gamma_v - 1)\lambda_v}{\gamma_v p_v} \frac{\partial T_v}{\partial r} - \frac{r \dot{p}_v}{3\gamma_v p_v}, \quad (\text{III-29})$$

$$a \dot{p}_v + 3\gamma_v p_v w_{va} + 3(\gamma_v - 1)q_{va} = 0, \quad (\text{III-30})$$

where γ_v is the ratio of the vapor specific heats. These integrals simplify solution of the problem since they explicitly express the vapor velocity through the temperature gradient and vapor pressure, and connect variation of the pressure in the vapor with integral parameters characterizing the bubble (bubble radius, radial bubble wall velocity, and the heat flux through the surface).

3. Model of Small Bubble in Standing Acoustic Wave

Consider the pressure and velocity fields, $p_\infty(x, t)$ and $U_\infty(x, t)$, of a plane standing acoustic wave in a liquid:

$$\begin{aligned} p_\infty(x, t) &= p_{\infty 0} + P_A \cos \omega t \sin kx, \\ U_\infty(x, t) &= -\frac{P_A}{\rho_l C} \sin \omega t \cos kx, \quad k = \frac{\omega}{C}, \end{aligned}$$

where k is the wavenumber. We limit our analysis to bubble radii small compared to the wavelength, $ka \ll 1$. The acoustic field in the liquid described by Eq.(III-31) is obtained using linearized equations for the liquid motion. This approximation assumes that

$$\left| U_\infty \frac{\partial U_\infty}{\partial x} \right| \ll \left| \frac{\partial U_\infty}{\partial t} \right|, \quad (\text{III-31})$$

or $P_A \ll \rho_l C^2$, which holds for a wide variety of situations.

The bubble position, $x_b(t)$, can be found by solving the following equations for bubble motion:

$$\begin{aligned} m_b \frac{dU_b}{dt} &= -\frac{4}{3}\pi a^3 (\nabla p_\infty|_{x=x_b} - \rho_l g) - m_b g + \\ &\quad \frac{2}{3}\pi \rho_l \left[\frac{d(a^3 U_\infty|_{x=x_b})}{dt} - \frac{d(a^3 U_b)}{dt} \right] + \\ &\quad + 4\pi K_\mu \mu_l a (U_\infty - U_b), \\ \frac{dx_b}{dt} &= U_b, \quad \frac{dm_b}{dt} = 4\pi a^2 \xi. \end{aligned}$$

Here U_b and m_b are the bubble velocity and mass, ξ is the rate of evaporation, g is the gravity acceleration, and K_μ is the viscous drag coefficient, which depends on the Reynolds number of the relative bubble motion. According to the Levich formula at high Reynolds numbers $K_\mu = 3$. For small Reynolds numbers it can be set to $K_\mu = 1$ or $K_\mu = 1.5$ for a liquid with and without surfactants. Equations (III-32) are projections of three dimensional equations of motion on the direction of bubble motion. To apply one-dimensional equations we assume that the vector of gravity acceleration is co-linear with the direction of the acoustic wave vector and the direction of the bubble motion.

We also modify the dynamic equation of bubble motion as

$$\begin{aligned} \left(1 - \frac{w_{la}}{C}\right) a \dot{w}_{la} + 2a \dot{w}_{la} - \frac{1}{2} \left(1 + \frac{\dot{a}}{C}\right) w_{la}^2 = \\ -\frac{1}{\rho_l} \left(1 + \frac{\dot{a}}{C} + \frac{a}{C} \frac{d}{dt}\right) \left[\Pi_{la}^{rr} + p_\infty(x_b(t), t) + 4\mu_l w_{la}/a - \frac{1}{4}\rho_l (U_b - U_\infty)^2 \right], \end{aligned} \quad (\text{III-32})$$

to include variation of the liquid pressure at the bubble location and the bubble relative motion.

4. Vapor-Gas Bubble Equilibrium in the Absence of an Acoustic Field

Vapor, gas, and vapor-gas bubbles can grow or shrink in liquids without any acoustic field. This happens due to phase transformations such as condensation or dissolution of a thermodynamically nonequilibrium bubble. A bubble in the bulk of the host liquid also cannot be in equilibrium under action of the gravity force. The buoyancy force will cause bubble motion in the absence of an acoustic field. If the thermodynamical and gravity driving forces are sufficiently high then the external acoustic field may not affect the bubble dynamics and this case can be studied separately without complication of the problem by acoustic action. In the present study we consider the case when the effects of an acoustic field are comparable to or larger than the effects driving the bubble dynamics in the absence of the acoustic field. We limit our study to small amplitude acoustic fields,

$$\frac{P_A}{p_{\infty 0}} = \epsilon \ll 1. \quad (\text{III-33})$$

Therefore in this case the effects of bubble thermodynamic and gravitational instability in the liquid are small, and we assume first that the bubble is in a state close to thermodynamic equilibrium.

For vapor bubbles this means that the mean liquid pressure is close to the saturation pressure at the liquid temperature far from the bubble:

$$p_{\infty 0} = p_s(T_{\infty}) + \Delta p, \quad \Delta = \frac{\Delta p}{p_{\infty 0}} \ll 1, \quad (\text{III-34})$$

where Δp is the liquid supercompression. For superheated liquids we have $\Delta p < 0$ and for subcooled liquids we have $\Delta p > 0$. We allow Δp to be non-zero, but it should be reasonably small (we provide mathematical definition in the sections dedicated to the method of solution). Even if $\Delta p = 0$, the vapor bubble is unstable due to capillary effects. Indeed the pressure inside a bubble of radius a_e in thermodynamic equilibrium is

$$p_v = p_s(T_{\infty}) + \Delta p + \frac{2\sigma}{a_e}. \quad (\text{III-35})$$

The temperature of an equilibrium bubble should be the same as the temperature of the liquid, T_{∞} , and at the same time it should be the saturation temperature at the given vapor pressure (III-35). This means that the equilibrium bubble radius is

$$a_e = -\frac{2\sigma}{\Delta p}, \quad (\text{III-36})$$

and equilibrium bubbles can exist only in superheated liquids. Note that this is an unstable equilibrium. In this and other cases a vapor bubble will grow or shrink in the absence of the acoustic field. We require that

$$\delta = \frac{1}{p_s(T_\infty)} \left| \Delta p + \frac{2\sigma}{a} \right| \ll 1, \quad (\text{III-37})$$

to have comparable effects of the acoustic pressure variations.

The pressure inside an equilibrium vapor-gas bubble is

$$p_g = p_v + p_i = p_{\infty 0} + \frac{2\sigma}{a_e}, \quad p_{\infty 0} = p_s(T_\infty) + \Delta p, \quad (\text{III-38})$$

where the difference between the mean liquid pressure and the saturation pressure may be not small. In an equilibrium state the vapor-gas bubble has the same temperature as the liquid, $T_g = T_\infty$. If effects of inert gas dissolution are neglected, then the inert gas concentration in the bubble can be arbitrary, c_{i0} . In the equilibrium state we have $p_v = p_s(T_\infty)$. Using equations of state (III-5)-(III-8) we can determine the equilibrium pressures of the inert gas and the gas mixture:

$$p_{ie} = \frac{c_{i0}R_i}{c_{v0}R_v} p_s(T_\infty), \quad p_{ge} = \frac{c_{v0}R_v + c_{i0}R_i}{c_{v0}R_v} p_s(T_\infty), \quad c_{v0} = 1 - c_{i0}. \quad (\text{III-39})$$

Then we can determine from (III-38) the equilibrium radius:

$$a_e = \frac{2\sigma}{p_{ie} - \Delta p} = \frac{2\sigma c_{v0}R_v}{c_{i0}R_i p_s(T_\infty) - c_{v0}R_v \Delta p}. \quad (\text{III-40})$$

If we take into account solubility of the inert gas then its concentration inside an equilibrium bubble is not arbitrary, but is determined by the equilibrium relation between the inert gas pressure and the dissolved gas concentration in the liquid, c_∞ (in our model, by Henry's law):

$$p_{ie} = c_\infty H, \quad c_{ie} = \frac{R_v p_{ie}}{R_i p_s(T_\infty) + R_v p_{ie}}, \quad p_{ge} = p_s(T_\infty) + p_{ie}, \quad a_e = \frac{2\sigma}{p_{ie} - \Delta p}. \quad (\text{III-41})$$

In any case a bubble of radius $a \neq a_e$ will grow or collapse in the absence of an acoustic field. The driving thermodynamic force is proportional to the difference between the actual and equilibrium gas pressures, and conditions (III-34) and (III-37) for vapor-gas bubbles become:

$$\Delta = \frac{|p_{ge} - p_{\infty 0}|}{p_{\infty 0}} \ll 1, \quad \delta = \frac{1}{p_{\infty 0}} \left| p_{ge} - p_{\infty 0} + \frac{2\sigma}{a} \right| \ll 1, \quad (\text{III-42})$$

where relations (III-39) or (III-41) can be used to determine p_{ge} .

A parameter responsible for bubble instability due to the buoyancy force can be found by the following reasoning. In a standing wave the hydrostatic pressure drop, Δp_h , along the wavelength should be much smaller than the ambient pressure. Otherwise a small amplitude acoustic pressure cannot balance the hydrostatic pressure drop, and bubble motion will be not influenced by the acoustic field. This condition can be written in the form:

$$g_r = \frac{\Delta p_h}{p_{\infty 0}} = \frac{\rho_l C g}{\omega p_{\infty 0}} \ll 1, \quad \left(\Delta p_h \sim \rho_l g L \sim \frac{\rho_l C g}{\omega} \right). \quad (\text{III-43})$$

5. Length Scales and Dimensionless Equations

The following characteristic length scales can be introduced for the problem considered:

$$L_p = \frac{1}{\omega} \left(\frac{p_{g*}}{\rho_l} \right)^{\frac{1}{2}}, \quad L_\mu = \left(\frac{\mu_l}{\rho_l \omega} \right)^{\frac{1}{2}}, \quad L_\sigma = \frac{\sigma}{p_{g*}}, \quad L_C = \frac{C}{\omega}, \quad (\text{III-44})$$

$$L_{Tg} = \left(\frac{\kappa_{g*}}{\omega} \right)^{\frac{1}{2}}, \quad L_{Tl} = \left(\frac{\kappa_l}{\omega} \right)^{\frac{1}{2}}, \quad L_\beta = \frac{\beta l}{(1-\rho)\omega\sqrt{2\pi R_v T_\infty}}, \quad L_d = \frac{1}{\omega} \left(\frac{\lambda_l T_\infty}{\mu_l} \right)^{\frac{1}{2}}$$

where $\kappa_l = \lambda_l/(\rho_l C_l)$ and $\kappa_{g*} = \lambda_{g*}/(\rho_{g*} C_{pg*})$ are thermal diffusivities of the liquid and the gas, and stars denote characteristic values of parameters used for scaling. L_{Tg} and L_{Tl} are the characteristic lengths of temperature penetration into the gas and liquid, L_p is the characteristic primary resonance length, L_μ is the characteristic thickness of the viscous boundary layer in the liquid, L_σ is the characteristic capillary length, L_C is the inverse wavenumber, and L_β and L_d are the characteristic lengths connected with the non-equilibrium phase transitions and viscous dissipation in the liquid.

The following dimensionless parameters also can be introduced:

$$Le_l = \frac{\kappa_l}{D_l}, \quad Le_g = \frac{\kappa_{g*}}{D_{g*}}, \quad \rho = \frac{\rho_{g*}}{\rho_l}, \quad \lambda = \frac{\lambda_{g*}}{\lambda_l},$$

$$k_\gamma = \frac{R_{g*}}{C_{pg*}}, \quad k_p = \frac{p_{\infty*}}{p_{g*}}, \quad k_H = \frac{H}{p_{g*}}, \quad k_R = \frac{R_i R_v}{R_{g*}^2}, \quad k_s = \frac{R_{g*} T_{g*}}{l_v},$$

$$k_v = \frac{l_v}{R_{g*} T_{g*}} + 1 - \rho, \quad k_i = \frac{l_i}{R_{g*} T_{g*}} + 1 - \rho, \quad k_{ic} = \frac{c_{i*} R_i}{R_{g*}},$$

$$\pi'_s = \frac{T_{g*}}{p_{g*}} \frac{dp_{vs}}{dT} \Big|_{T=T_{g*}}, \quad \pi''_s = \frac{T_{g*}^2}{p_{g*}^2} \frac{d^2 p_{vs}}{dT^2} \Big|_{T=T_{g*}},$$

$$\alpha_g = \frac{R_i - R_v}{R_{g*}}, \quad \alpha_{cp} = \frac{C_{pi} - C_{pv}}{C_{pg*}}.$$

Note that the length scales written above in combination with the dimensionless parameters produce new length scales having physical meaning. For example, characteristic lengths

$$L_{cg} = \left(\frac{D_{g*}}{\omega} \right)^{\frac{1}{2}} = \frac{L_{Tg}}{\sqrt{Le_g}}, \quad L_{cl} = \left(\frac{D_l}{\omega} \right)^{\frac{1}{2}} = \frac{L_{Tl}}{\sqrt{Le_l}}, \quad (\text{III-45})$$

represent the characteristic thicknesses of the mass diffusion boundary layers in the gas and in the liquid. The ratio of the bubble radius to any characteristic length scale listed in (III-44) produces 8 independent dimensionless parameters. Taking into account that all but two of α (III-13), ϵ , (III-33), δ , (III-42), and g_r , (III-43) and parameters (III-45) are also independent we can see that the dynamics of a vapor-gas bubble is controlled by 26 basic dimensionless parameters (!). For a pure vapor bubble this number reduces to 15.

Chapter IV.

Multiscale Technique For Bubbles in Isotropic Fields

To obtain the equation for rectified heat transfer we use a multiscale asymptotic technique for weakly non-linear oscillations of drops and bubbles [14, 2]. However, the method must be modified, since the effect of surface tension neglected in [14, 2] changes the rank of the system matrix for zero-mode of oscillation, and a straight-forward application of the technique is impossible. To demonstrate the method of solution we will start with a simplified system for pure vapor bubbles. Then we show how to include effects of bubble drift in standing waves and two-component effects.

1. Transformation of Variables

First, we reduce the number of variables by eliminating $\rho_v, w_v, \rho_{va}, w_{va}$, and Π_{la}^{rr} from the system. The governing equations can be represented in the following form:

$$\rho_l \dot{a} - \rho_l w_{la} - \xi = 0, \quad (\text{IV-1})$$

$$\begin{aligned} & \left(a + \frac{4\mu_l}{\rho_l C} - \frac{aw_{la}}{C} \right) \dot{w}_{la} + \left(\frac{3}{2} w_{la} + \frac{2\xi}{\rho_l} - \frac{w_{la}^2}{2C} - \frac{w_{la}\xi}{2C\rho_l} + \frac{4\mu_l}{\rho_l a} \right) w_{la} \\ &= \frac{1}{\rho_l} \left[1 + \frac{1}{C} \left(w_{la} + \frac{\xi}{\rho_l} \right) + \frac{a}{C} \frac{d}{dt} \right] \left[p_v - p_\infty(t) + \left(\frac{1}{\rho_l} - \frac{R_v T_a}{p_v} \right) \xi^2 \right] - \frac{2\sigma}{\rho_l a}, \\ & a \dot{p}_v + 3\gamma p_v \dot{a} + 3(\gamma - 1) q_{va} - 3\gamma \xi R_v T_a = 0, \end{aligned} \quad (\text{IV-2})$$

$$\left[\frac{1}{\rho_l} \left(p_v - \frac{2\sigma}{a} \right) - R_v T_a - l \right] \xi + q_{va} - q_{la} = \frac{1}{2} \left(\frac{1}{\rho_l} - \frac{R_v T_a}{p_v} \right)^2 \xi^3, \quad (\text{IV-3})$$

$$\xi - \frac{\beta}{\sqrt{2\pi R_v T_a}} [p_s(T_a) - p_v] = 0. \quad (\text{IV-4})$$

We then transform $(r, t) \rightarrow (\eta, t)$ with $\eta = r/a(t)$ to fix the moving boundary in the heat transfer problems:

$$\begin{aligned} & \frac{p_v T_\infty a^2}{p_s(T_\infty) \kappa_v} \left[\frac{\partial T_v}{\partial t} - \frac{(\gamma - 1) \dot{p}_v T_v}{\gamma p_v} - \left(\frac{\dot{a}}{a} + \frac{\dot{p}_v}{3\gamma p_v} \right) \eta \frac{\partial T_v}{\partial \eta} \right] \\ &= \frac{T_v}{\eta^2} \frac{\partial}{\partial \eta} \left(\eta^2 \frac{\partial T_v}{\partial \eta} \right) - \left(\frac{\partial T_v}{\partial \eta} \right)^2, \end{aligned} \quad (\text{IV-5})$$

$$q_{va} = - \frac{\lambda_v}{a} \frac{\partial T_v}{\partial \eta} \Big|_{\eta=1}, \quad T_v|_{\eta=1} = T_a.$$

$$\frac{a^2}{\kappa_l} \frac{\partial T_l}{\partial t} - \frac{1}{\eta^2} \frac{\partial}{\partial \eta} \left(\eta^2 \frac{\partial T_l}{\partial \eta} \right) = \left[\frac{a \dot{a}}{\kappa_l} \left(\eta - \frac{1}{\eta^2} \right) + \frac{a \xi}{\rho_l \kappa_l \eta^2} \right] \frac{\partial T_l}{\partial \eta} + \frac{12 \mu_l w_{la}^2}{\lambda_l \eta^6}. \quad (\text{IV-6})$$

$$T_l|_{\eta=1} = T_a, \quad T_l|_{\eta=\infty} = T_\infty, \quad q_{la} = - \frac{\lambda_l}{a} \frac{\partial T_l}{\partial \eta} \Big|_{\eta=1},$$

where κ_l and κ_v are the thermal diffusivities of the liquid and vapor (at ambient conditions).

Next, we introduce dimensionless fast and slow time scales, $t_0 = \omega t$, and $t_n = \epsilon^n \omega t$, $n = 1, 2, \dots$. All unknowns are considered now as functions of this set of times and the temporal derivatives are represented as series:

$$\frac{d}{dt} = \omega \left(\frac{\partial}{\partial t_0} + \epsilon \frac{\partial}{\partial t_1} + \epsilon^2 \frac{\partial}{\partial t_2} + \dots \right). \quad (\text{IV-7})$$

Finally, we expand the unknowns in the following asymptotic series:

$$a(t) = a_0(t_1, t_2, \dots) [1 + \epsilon a_1(t_0, t_1, \dots) + \dots], \quad (\text{IV-8})$$

$$w_{la}(t) = \omega a_0(t_1, t_2, \dots) [\epsilon w_1(t_0, t_1, \dots) + \dots], \quad (\text{IV-9})$$

$$p_v(t) = p_s(T_\infty) [1 + \epsilon p_1(t_0, t_1, \dots) + \dots], \quad (\text{IV-10})$$

$$T_a(t) = T_\infty [1 + \epsilon T_1(t_0, t_1, \dots) + \dots], \quad (\text{IV-11})$$

$$\xi(t) = \omega \rho_{v\infty} a_0(t_1, t_2, \dots) [\epsilon \xi_1(t_0, t_1, \dots) + \dots], \quad (\text{IV-12})$$

$$q_{la}(t) = \lambda_l T_\infty [a(t_0, t_1, \dots)]^{-1} [\epsilon q_1(t_0, t_1, \dots) + \dots], \quad (\text{IV-13})$$

$$q_{va}(t) = \lambda_v T_\infty [a(t_0, t_1, \dots)]^{-1} [\epsilon r_1(t_0, t_1, \dots) + \dots], \quad (\text{IV-14})$$

$$T_l(\eta, t) = T_\infty [1 + \epsilon u_1(\eta, t_0, t_1, \dots) + \dots], \quad (\text{IV-15})$$

$$T_v(\eta, t) = T_\infty [1 + \epsilon v_1(\eta, t_0, t_1, \dots) + \dots], \quad (\text{IV-16})$$

where $\rho_{v\infty}$ is the vapor density at $T_v = T_\infty$ and $p_v = p_s(T_\infty)$.

2. Solution of Thermal Problems

Formally, as $\epsilon \rightarrow 0$, the convective and source terms in the energy equations are small and, in the m -th order approximation, we have the following inhomogeneous linear equations to determine the temperatures outside and inside the bubble, respectively:

$$\frac{a_0^2}{L_{Tl}^2} \frac{\partial u_m}{\partial t_0} - \frac{1}{\eta^2} \frac{\partial}{\partial \eta} \left(\eta^2 \frac{\partial u_m}{\partial \eta} \right) = f_m, \quad (\text{IV-16})$$

$$\frac{a_0^2}{L_{Tv}^2} \frac{\partial v_m}{\partial t_0} - \frac{k_\gamma a_0^2}{L_{Tv}^2} \frac{\partial p_m}{\partial t_0} - \frac{1}{\eta^2} \frac{\partial}{\partial \eta} \left(\eta^2 \frac{\partial v_m}{\partial \eta} \right) = g_m, \quad (\text{IV-17})$$

These are subject to the boundary conditions:

$$u_m|_{\eta=1} = T_m, \quad u_m|_{\eta=\infty} = 0, \quad v_m|_{\eta=1} = T_m, \quad v_m|_{\eta=0} < \infty, \quad (\text{IV-18})$$

where $f_m(\eta, t_0, t_1, \dots)$ and $g_m(\eta, t_0, t_1, \dots)$ are functions that depend on approximations of order less than m .

Let us evaluate the range of frequencies, where this scheme is valid. Since for vapor bubbles the heat transfer in the liquid plays the major role, consider as an example the energy equation for the liquid (IV-6), for which the terms can be evaluated as follows:

$$\begin{aligned} \frac{a^2}{\kappa_l} \frac{\partial T_l}{\partial t} &\sim \frac{a_0^2 \Delta T}{\kappa_l t_*}, & \frac{1}{\eta^2} \frac{\partial}{\partial \eta} \left(\eta^2 \frac{\partial T_l}{\partial \eta} \right) &\sim \frac{a_0^2 \Delta T}{d_l^2}, \\ \frac{a \dot{a}}{\kappa_l} \left(\eta - \frac{1}{\eta^2} \right) \frac{\partial T_l}{\partial \eta} &\sim \frac{(\eta - 1) a_0 \Delta a \Delta T}{\kappa_l d_l t_*}, & \frac{\alpha \xi}{\rho_l \kappa_l \eta^2} \frac{\partial T_l}{\partial \eta} &\sim \frac{\rho a_0^2 \Delta a \Delta T}{\kappa_l t_* d_l}, \\ \frac{12 \mu_l w_{la}^2}{\lambda_l \eta^6} &\sim \frac{10 (\Delta a)^2 \mu_l}{t_*^2 \lambda_l}. \end{aligned} \quad (\text{IV-19})$$

Here Δa and ΔT are the characteristic variations of the bubble size and liquid temperature, d_l is the thermal boundary layer thickness, and t_* is the characteristic time. Consider fast bubble oscillations. In this case we have $\Delta a \sim \epsilon a_0$, $\Delta T \sim \epsilon T_\infty$, $d_l \sim L_{Tl}$ and $t_* \sim \omega^{-1}$. At $\epsilon \sim 0.1$ the latter term in (IV-19) is small compared with the first term for $\omega \ll \omega_d = \rho_l c_l T_\infty / \mu_l$. Normally this limitation is not restrictive (e.g. for water and helium at atmospheric pressures we have $\omega_d / 2\pi \sim 10^{11}$ Hz). The convective term is related to the liquid motion generated by the moving bubble surface (the third term) and condensation or evaporation (the fourth term). The third term (IV-19) is small at small ϵ even at high frequencies, since in this case high temperature gradients of order $\epsilon T_\infty / L_{Tl}$ are realized in a thin boundary layer $\eta - 1 \sim L_{Tl} / a_0$ and $(\eta - \eta^{-2}) \partial T_l / \partial \eta \sim \epsilon T_\infty$. The fourth term (IV-19) is small compared to the first term (IV-19) if $\epsilon \rho a_0 \ll L_{Tl}$. For $\epsilon \sim 0.1$, $\rho \sim 10^{-3}$, and bubbles of typical radius $a_0 \lesssim 1$ mm, the thickness of the thermal boundary layer in the liquid should be much larger than $0.1 \mu\text{m}$. For water at atmospheric pressures this limits the theory to frequencies $\omega / 2\pi \ll 1$ MHz. Note that the acoustic wavelength is of order 1 mm at frequencies $\omega / 2\pi \sim 1$ MHz, and the theory is limited by such frequencies for 1 mm bubbles.

We assume that all functions in (IV-16) - (IV-18) are periodic with respect to t_0 . For example

$$u_m(\eta, t_0, t_1, \dots) = \text{Re} \left\{ \sum_{n=0}^m u_{mn}(\eta, t_1, t_2, \dots) e^{in t_0} \right\}, \quad (\text{IV-20})$$

$$p_m(t_0, t_1, \dots) = \text{Re} \left\{ \sum_{n=0}^m p_{mn}(t_1, t_2, \dots) e^{in t_0} \right\}, \quad (\text{IV-21})$$

where u_{mn} and p_{mn} are the complex amplitudes (the number of modes increases with the number of approximations because of non-linear generation of subharmonics).

We should also notice that the first two orders of approximation of the present theory do not depend on initial conditions. This assumes that the bubble resides in the liquid for a long time and a quasi-steady slowly changing average temperature profile is developed near the bubble. In the m -th order approximation equation (IV-16) written for zero-mode

$$\frac{1}{\eta^2} \frac{\partial}{\partial \eta} \left(\eta^2 \frac{\partial u_{m0}}{\partial \eta} \right) = -f_{m0} \quad (\text{IV-22})$$

shows that the non-stationary, $\chi \frac{\partial u_{m0}}{\partial t_k}$, and convective, $Pe_0(\eta - \eta^{-2}) \frac{\partial u_{m0}}{\partial \eta}$, terms are considered to be small compared to the conductive term $\frac{1}{\eta^2} \frac{\partial}{\partial \eta} \left(\eta^2 \frac{\partial u_{m0}}{\partial \eta} \right)$ and are passed to the approximations of order higher than m . Here $Pe_0 = \frac{\epsilon^k a_0}{L_{T1}^2} \frac{\partial a_0}{\partial t_k}$ is the Peclet number of the slow bubble motion, and $\chi = \frac{\epsilon^k a_0^2}{L_{T1}^2}$ (we show later that nothing in the present theory depends on t_1 , so $k \geq 2$). This is correct from the point of view of the current formal asymptotic procedure, however, is questionable from the physical view point, because actual values of χ and Pe_0 may be not small. Bringing these terms into the m -th order approximation creates a mathematical problem, which solution currently is not available. Note that Fyrrillas & Szeri [64] obtained a solution for transient slowly evolving fields considering the non-stationary term to be of the same order as the conductive term, but for constant a_0 ($Pe_0 = 0$). If significant growth or shrinkage of the bubble occur in some time scale t_k (so $\partial a_0 / \partial t_k \sim a_0$), then in that scale $Pe_0 \sim \chi$, and the convective term is of the same order of magnitude as the non-stationary term.

The assumption on periodicity of functions in the fast time scale is not valid for initial value problems at times of order of one period of oscillation. Fyrrillas & Szeri [64] evaluated that time as a few periods of oscillation. The depth of penetration of temperature perturbations into the vapor and liquid due to oscillations of the bubble surface temperature is much smaller than the thickness of the thermal boundary layer evolving in slow time scales. That is why the stage of establishment of a periodical solution is not important when we consider slowly changing temperature fields. Since slowly changing fields depend only on slow variables the initial conditions for their evolution should also be formulated in slow time scales. In the present theory the initial conditions appear in the third-order approximation, which also requires a spatial matching procedure and is described in a separate section.

For each mode, Equations (IV-16) and (IV-17) are replaced by equations of the same form, but with the factor in in place of the operator $\partial / \partial t_0$. Solution of these linear problems are available

[14, 2] and can be represented in the following form:

$$\begin{aligned} u_{mn} &= \frac{1}{\eta} \left\{ A_{mn} \exp \left[-(\eta - 1) \frac{a_0}{L_{Tl}} \sqrt{in} \right] + F_{mn}(\eta) \right\}, \\ v_{mn} &= k_\gamma p_{mn} + \frac{1}{\eta} \left[B_{mn} \sinh \left(\eta \frac{a_0}{L_{Tv}} \sqrt{in} \right) + G_{mn}(\eta) \right], \end{aligned} \quad (IV-23)$$

$$F_{mn}(\eta) = \frac{1}{2\sqrt{in}} \frac{L_{Tl}}{a_0} \int_1^\infty \exp \left[-|x - \eta| \frac{a_0}{L_{Tl}} \sqrt{in} \right] x f_{mn}(x) dx, \quad (IV-24)$$

$$G_{mn}(\eta) = \frac{1}{\sqrt{in}} \frac{L_{Tv}}{a_0} \int_0^\eta \sinh \left[(x - \eta) \frac{a_0}{L_{Tv}} \sqrt{in} \right] x g_{mn}(x) dx, \quad (IV-25)$$

$$A_{mn} = T_{mn} - F_{mn}(1),$$

$$B_{mn} = \left[\sinh \left(\frac{a_0}{L_{Tv}} \sqrt{in} \right) \right]^{-1} [T_{mn} - G_{mn}(1) - k_\gamma p_{mn}].$$

Here we consider that $\text{Re}\{\sqrt{i}\} > 0$.

The complex amplitudes of the heat fluxes can be determined as:

$$q_{mn} = H_n T_{mn} - C_{mn}, \quad r_{mn} = I_n (k_\gamma p_{mn} - T_{mn}) + D_{mn}, \quad (IV-26)$$

$$H_n = 1 + \frac{a_0}{L_{Tl}} \sqrt{in}, \quad I_n = \frac{a_0}{L_{Tv}} \sqrt{in} \coth \left(\frac{a_0}{L_{Tv}} \sqrt{in} \right) - 1,$$

$$C_{mn} = 2 \frac{a_0}{L_{Tl}} \sqrt{in} F_{mn}(1), \quad (IV-27)$$

$$D_{mn} = \left[\sinh \left(\frac{a_0}{L_{Tv}} \sqrt{in} \right) \right]^{-1} \int_0^1 \sinh \left(\frac{a_0 x}{L_{Tv}} \sqrt{in} \right) x g_{mn}(x) dx. \quad (IV-28)$$

3. Complex Amplitudes

Substituting asymptotic series (IV-8) - (IV-15) and (IV-7) into (IV-1) - (IV-4) and collecting terms for the same powers of ϵ , we obtain the following linear inhomogeneous equations to determine the unknowns in the m th order approximation:

$$\frac{\partial a_m}{\partial t_0} - w_m - \rho \xi_m = Y_m^{(1)}, \quad (IV-29)$$

$$-\frac{2L_\sigma}{a_0} a_m + \frac{a_0^2}{L_p^2} \left[\left(1 + 4 \frac{L_\mu^2}{L_C a_0} \right) \frac{\partial}{\partial t_0} + \frac{4L_\mu^2}{a_0^2} \right] w_m - \left(1 + \frac{a_0}{L_C} \frac{\partial}{\partial t_0} \right) p_m = Y_m^{(2)}, \quad (IV-30)$$

$$3\gamma \frac{\partial a_m}{\partial t_0} + \frac{\partial p_m}{\partial t_0} - 3\gamma \xi_m + 3\gamma \frac{L_{Tv}^2}{a_0^2} r_m = Y_m^{(3)}, \quad (IV-31)$$

$$-\frac{\lambda k_\gamma a_0^2}{k_s L_{Tv}^2} \left\{ 1 + k_s \left[1 - \rho \left(1 - \frac{2L_\sigma}{a_0} \right) \right] \right\} \xi_m - q_m + \lambda r_m = Y_m^{(4)}, \quad (\text{IV-32})$$

$$\xi_m + \frac{L_\beta}{a_0} [k_s (1 - \rho) p_m - T_m] = Y_m^{(5)}, \quad (\text{IV-33})$$

where the right-hand sides, $Y_m^{(j)}$, $j = 1, \dots, 5$, depend on the low-order approximations.

To obtain equations for the complex amplitude of the n th mode of oscillations we can replace $\partial/\partial t_0$ in these equations with in . Consequently, equations (IV-29) - (IV-33) and (IV-26) for the complex amplitudes can be represented in the following matrix form:

$$\mathbf{M}_n \mathbf{X}_{mn} = \mathbf{Y}_{mn}, \quad (\text{IV-34})$$

$$\mathbf{M}_n = \begin{pmatrix} in & -1 & 0 & -\rho & 0 & 0 & 0 \\ -2L_\sigma/a_0 & M_{22} & M_{23} & 0 & 0 & 0 & 0 \\ 3\gamma in & 0 & in & -3\gamma & 0 & 0 & 3\gamma L_{Tv}^2/a_0^2 \\ 0 & 0 & 0 & M_{44} & 0 & -1 & \lambda \\ 0 & 0 & M_{53} & 1 & -L_\beta/a_0 & 0 & 0 \\ 0 & 0 & 0 & 0 & H_n & -1 & 0 \\ 0 & 0 & -k_\gamma I_n & 0 & I_n & 0 & 1 \end{pmatrix},$$

$$\mathbf{X}_{mn} = \begin{pmatrix} a_{mn} \\ w_{mn} \\ p_{mn} \\ \xi_{mn} \\ T_{mn} \\ q_{mn} \\ r_{mn} \end{pmatrix}, \quad \mathbf{Y}_{mn} = \begin{pmatrix} Y_{mn}^{(1)} \\ Y_{mn}^{(2)} \\ Y_{mn}^{(3)} \\ Y_{mn}^{(4)} \\ Y_{mn}^{(5)} \\ Y_{mn}^{(6)} \\ Y_{mn}^{(7)} \end{pmatrix},$$

where

$$\begin{aligned} M_{22} &= \frac{a_0^2}{L_p^2} \left[\left(1 + 4 \frac{L_\mu^2}{L_C a_0} \right) in + \frac{4L_\mu^2}{a_0^2} \right], & M_{23} &= -1 - \frac{ina_0}{L_C}, \\ M_{44} &= -\frac{\lambda k_\gamma a_0^2}{L_{Tv}^2} \left[\frac{1}{k_s} + 1 - \rho \left(1 - \frac{2L_\sigma}{a_0} \right) \right], & M_{53} &= \frac{(1 - \rho) k_s L_\beta}{a_0}, \\ Y_{mn}^{(6)} &= C_{mn}, & Y_{mn}^{(7)} &= D_{mn}. \end{aligned} \quad (\text{IV-35})$$

Let us now specify the structure of the right hand side terms \mathbf{Y}_{mn} . We can represent them as:

$$\mathbf{Y}_{mn} = \mathbf{S}_{mn} + \mathbf{N}_{mn} + \mathbf{F}_{mn}, \quad (\text{IV-36})$$

where \mathbf{S}_{mn} is generated by slow time scale evolution of linear terms, \mathbf{N}_{mn} is generated by non-linear terms, and \mathbf{F}_{mn} is the external forcing. \mathbf{S}_{mn} can be found from linear equations (IV-29) -

(IV-33), (IV-16), (IV-17), (IV-24), (IV-25), (IV-27), and (IV-28) and asymptotic series (IV-7) and (IV-8) - (IV-15):

$$\begin{aligned}
S_{mn}^{(1)} &= -\frac{1}{a_0} \left[\delta_{n0} \frac{\partial a_0}{\partial t_m} + \sum_{j=1}^{m-1} \frac{\partial(a_0 a_{jn})}{\partial t_{m-j}} \right], \\
S_{mn}^{(2)} &= -\frac{a_0^2}{L_p^2} \left(1 + 4 \frac{L_\mu^2}{L_C a_0} \right) \sum_{j=1}^{m-1} \frac{\partial w_{jn}}{\partial t_{m-j}} - \frac{a_0}{L_C} \sum_{j=1}^{m-1} \frac{\partial p_{jn}}{\partial t_{m-j}}, \\
S_{mn}^{(3)} &= -\frac{3\gamma}{a_0} \left[\delta_{n0} \frac{\partial a_0}{\partial t_m} + \sum_{j=1}^{m-1} \frac{\partial(a_0 a_{jn})}{\partial t_{m-j}} \right] - \sum_{j=1}^{m-1} \frac{\partial p_{jn}}{\partial t_{m-j}}, \\
S_{mn}^{(4)} &= S_{mn}^{(5)} = 0, \\
S_{mn}^{(6)} &= -\frac{a_0^2}{L_{Tl}^2} \int_1^{\infty} \sum_{j=1}^{m-1} \frac{\partial u_{jn}}{\partial t_{m-j}} \exp \left[-(\eta - 1) \frac{a_0}{L_{Tl}} \sqrt{in} \right] \eta d\eta, \\
S_{mn}^{(7)} &= -\frac{a_0^2}{L_{Tv}^2} \int_0^1 \left(\sum_{j=1}^{m-1} \frac{\partial v_{jn}}{\partial t_{m-j}} - k_\gamma \sum_{j=1}^{m-1} \frac{\partial p_{jn}}{\partial t_{m-j}} \right) \frac{\sinh \left(\frac{a_0}{L_{Tv}} \eta \sqrt{in} \right)}{\sinh \left(\frac{a_0}{L_{Tv}} \sqrt{in} \right)} \eta d\eta,
\end{aligned}$$

where the superscript in the brackets near S_{mn} shows the number of the vector S_{mn} component and δ_{ij} is the Kronecker delta.

In our case, F_{mn} is non-zero only for $n = 0, 1$. The order m for which $F_{m0} \neq 0$ depends on the relation between the small parameters ϵ and δ determined by (III-33) and (III-37). For $\delta \sim \epsilon^{m_*}$ we have $F_{m0} \neq 0$ only at $m = m_*$. Since ϵ and δ are independent parameters, m_* can be selected arbitrarily. However, a better way is to set m_* using the characteristic asymptotic form. This can be done by the following physical reasoning. ϵ and δ are parameters responsible for two instabilities regarding a vapor bubble. The former is responsible for the instability due to rectified heat transfer and the latter for the instability due to the surface tension and deviation from the saturation state. The characteristic times required for development of these two instabilities are proportional, respectively, to the energy of the acoustic field, or ϵ^2 , and to the deviation from the equilibrium state, or δ . These two instabilities can be brought to the same order of approximation if

$$\delta \sim \epsilon^2. \quad (\text{IV-37})$$

This is a condition for the characteristic asymptotic form. Accepting (IV-37) we have the following expressions for the non-zero components of F_{mn} :

$$F_{20}^{(2)} = -\frac{1}{\epsilon^2} \left(\Delta + \frac{2L_\sigma}{a_0} \right), \quad F_{11}^{(2)} = -\left(1 + \frac{ia_0}{L_C} \right). \quad (\text{IV-38})$$

An expression for N_{mn} can also be derived using governing equations and asymptotic representations. We do not reproduce them in general form here since they are too unwieldy.

4. Evolution in Slow Time Scales

To obtain equations describing evolution of the unknowns in slow time scales, let us consider the operator \mathbf{M}_0 ,

$$\mathbf{M}_0 = \begin{pmatrix} 0 & -1 & 0 & -\rho & 0 & 0 & 0 \\ -2L_\sigma/a_0 & 4L_\mu^2/L_p^2 & -1 & 0 & 0 & 0 & 0 \\ 0 & 0 & 0 & -3\gamma & 0 & 0 & 3\gamma L_{Tv}^2/a_0^2 \\ 0 & 0 & 0 & M_{44} & 0 & -1 & \lambda \\ 0 & 0 & M_{53} & 1 & -L_\beta/a_0 & 0 & 0 \\ 0 & 0 & 0 & 0 & 1 & -1 & 0 \\ 0 & 0 & 0 & 0 & 0 & 0 & 1 \end{pmatrix}. \quad (\text{IV-39})$$

The determinant of this matrix is non-zero:

$$\det \mathbf{M}_0 = \frac{6\gamma(1-\rho)k_s L_\beta L_\sigma}{a_0^2}. \quad (\text{IV-40})$$

From (IV-37) we have $L_\sigma/a_0 \sim \delta \sim \epsilon^2 \ll 1$, or $\det \mathbf{M}_0 = O(\epsilon^2)$. According Cramer's rule the zero-mode components of solution, $X_{m0}^{(i)}$, are

$$X_{m0}^{(i)} = \frac{\det \mathbf{M}_{0m}^{(i)}}{\det \mathbf{M}_0}, \quad i = 1, \dots, 7, \quad (\text{IV-41})$$

where $\mathbf{M}_{0m}^{(i)}$ is the matrix \mathbf{M}_0 with the i th column replaced by the right hand side vector, \mathbf{Y}_{m0} . By definition of an asymptotic expansion $X_{m0}^{(i)}$ should be of order of unity. Thus

$$\det \mathbf{M}_{0m}^{(i)} = O(\epsilon^2), \quad i = 1, \dots, 7.$$

The form of matrix \mathbf{M}_0 (IV-39) shows that this condition automatically holds for $i = 2, \dots, 7$. However for $i = 1$ it becomes non-trivial. Calculating $\det \mathbf{M}_0^{(1)}$, we have:

$$\begin{aligned} \det \mathbf{M}_{0m}^{(1)} &= -3\gamma M_{53} \left(\frac{4L_\mu^2}{L_p^2} Y_{m0}^{(1)} + Y_{m0}^{(2)} \right) + \frac{3\gamma L_\beta}{a_0} \left(Y_{m0}^{(4)} - Y_{m0}^{(6)} - \lambda Y_{m0}^{(7)} \right) \\ &\quad - \left(1 - \frac{4\rho L_\mu^2}{L_p^2} M_{53} - \frac{L_\beta}{a_0} M_{44} \right) \left(Y_{m0}^{(3)} - \frac{3\gamma L_{Tv}^2}{a_0^2} Y_{m0}^{(7)} \right) - 3\gamma Y_{m0}^{(5)}. \end{aligned}$$

where $Y_{m0}^{(6)}$ and $Y_{m0}^{(7)}$ can be found as limits of (IV-24), (IV-25), and (IV-27) at $n \rightarrow 0$:

$$Y_{m0}^{(6)} \equiv C_{m0} = \int_1^\infty \eta f_{m0}(\eta) d\eta, \quad Y_{m0}^{(7)} \equiv D_{m0} = \int_0^1 \eta^2 g_{m0}(\eta) d\eta. \quad (\text{IV-42})$$

To avoid secular terms in expansion (IV-8), a_{m0} and $\det \mathbf{M}_{0m}^{(1)}$ should be limited at $t_j \rightarrow \infty, j = 1, 2, \dots$. This is the only requirement for the uniform asymptotic expansion which is not unique. The

non-uniqueness of the asymptotic expansion can be easily demonstrated for the case of $L_\sigma = 0$ (the effect of surface tension is neglected). In this case $\det \mathbf{M}_0 = 0$, $\det \mathbf{M}_{0m}^{(1)} = 0$, and a_{m0} is determined as an arbitrary limited function of slow times. If we set $a_{m0} = 0$, for $m = 1, 2, \dots$, then we uniquely select the expansion in which a_0 is the bubble radius averaged over the period of oscillation, $\langle a \rangle$, since $\langle a \rangle = a_0 (1 + \epsilon a_{10} + \epsilon^2 a_{20} + \dots)$. Such a definition of arbitrary a_{m0} was used in a previous investigation [2]. Similarly, for the case $L_\sigma \neq 0$ we can specify

$$\det \mathbf{M}_{0m}^{(1)} = 0. \quad (\text{IV-43})$$

According (IV-41) this leads to

$$a_{m0} = 0, \quad \text{for } m = 1, 2, \dots, \quad \langle a \rangle = a_0, \quad (\text{IV-44})$$

which is a convenient definition of a_0 .

5. First Order Approximation

In the first-order approximation the non-linear term \mathbf{N}_{1n} in (IV-36) is zero, the components of the external forcing are given by (IV-38), while the slow-scale evolution vector \mathbf{S}_{1n} has only two non-zero components (IV-37):

$$S_{10}^{(1)} = -\frac{1}{a_0} \frac{\partial a_0}{\partial t_1}, \quad S_{10}^{(3)} = -\frac{3\gamma}{a_0} \frac{\partial a_0}{\partial t_1}. \quad (\text{IV-45})$$

Using (IV-38) we can explicitly resolve (IV-34) for the first-mode using Cramer's rule:

$$X_{11}^{(j)} = - \left(1 + \frac{ia_0}{L_C} \right) \frac{\Delta^{(j)}}{\det \mathbf{M}_1}, \quad (\text{IV-46})$$

$j = 1, \dots, 7$, where $X_{11}^{(j)}$ are the components of the vector \mathbf{X}_{11} and $\Delta^{(j)}$ can be represented as:

$$\begin{aligned} \Delta^{(1)} &= \frac{L_\beta}{a_0} (iM_{44} + 3\gamma k_\gamma \lambda I_1) - (i + 3\gamma M_{53}) (H_1 + \lambda I_1) \\ &\quad + \frac{3\gamma L_{Tv}^2}{a_0^2} \left(\frac{k_\gamma L_\beta}{a_0} M_{44} - M_{53} M_{44} - k_\gamma H_1 \right) I_1, \\ \Delta^{(2)} &= i\Delta^{(1)} - \rho\Delta^{(4)}, \quad \Delta^{(3)} = 3i\gamma \left(H_1 + \lambda I_1 - \frac{L_\beta}{a_0} M_{44} \right), \\ \Delta^{(4)} &= 3i\gamma \left[\frac{k_\gamma L_\beta \lambda}{a_0} I_1 - M_{53} (H_1 + \lambda I_1) \right], \\ \Delta^{(5)} &= 3i\gamma (k_\gamma \lambda I_1 - M_{53} M_{44}), \\ \Delta^{(6)} &= H_1 \Delta^{(5)}, \quad \Delta^{(7)} = I_1 (k_\gamma \Delta^{(3)} - \Delta^{(5)}), \\ \det \mathbf{M}_1 &= \frac{a_0^2}{L_p^2} \left[\left(1 + 4 \frac{L_\mu^2}{L_C a_0} \right) i + \frac{4L_\mu^2}{a_0^2} \right] \Delta^{(2)} - \left(1 + \frac{ia_0}{L_C} \right) \Delta^{(3)} - \frac{2L_\sigma}{a_0} \Delta^{(1)}. \end{aligned}$$

Note that these equations are consistent with previous results [30, 17, 3, 59, 2].

From (IV-42) and (IV-43) we have using (IV-36), (IV-38), (IV-45), and (IV-35):

$$\frac{\partial a_0}{\partial t_1} = 0, \quad a_0 = a_0(t_2, t_3, \dots). \quad (\text{IV-47})$$

To determine a slow-time evolution of the mean bubble radius we need to consider the second-order approximation.

6. Equation for Rectified Heat Transfer in the Second Order Approximation

Since a_0 does not depend on t_1 , the same is true for all other variables. Thus, the non-zero components of vector S in the second order approximation are

$$S_{20}^{(1)} = -\frac{1}{a_0} \frac{\partial a_0}{\partial t_2}, \quad S_{20}^{(3)} = -\frac{3\gamma}{a_0} \frac{\partial a_0}{\partial t_2}. \quad (\text{IV-48})$$

The non-zero forcing term is (IV-38), while the components of the non-linear term N_{2n} can be found in the second-order approximation from quadratic non-linearities. The non-zero components include modes 0 and 2 which correspond to the average fluxes and nonlinear doubling of the oscillation frequency. To obtain the equation of rectified heat transfer it is sufficient to consider just zero-mode vector N_{20} . After some algebra one can find the components of this vector in the following form:

$$\begin{aligned} N_{20}^{(1)} &= 0, \\ N_{20}^{(2)} &= \text{Re} \left\{ \frac{4L_\mu^2 + ia_0^2}{2L_p^2} a_{11}^* w_{11} \right\} + \frac{a_0^2}{4L_p^2} |w_{11}|^2 - \frac{L_\sigma}{a_0} |a_{11}|^2 - \frac{\rho(1-\rho)a_0^2}{2L_p^2} |\xi_{11}|^2, \\ N_{20}^{(3)} &= \frac{3\gamma}{2} \text{Re} \left\{ \left(1 - \frac{2}{3\gamma} \right) ip_{11} a_{11}^* + \xi_{11} a_{11}^* + \xi_{11}^* T_{11} \right\}, \\ N_{20}^{(4)} &= \frac{\lambda k_\gamma a_0^2}{2L_{Tv}^2} \text{Re} \left\{ T_{11} \xi_{11}^* - \rho p_{11} \xi_{11}^* + \left(\frac{1}{k_s} + 1 - \rho \right) a_{11} \xi_{11}^* \right\}, \\ N_{20}^{(5)} &= \frac{L_\beta}{4a_0} k_s (1-\rho) \pi_s'' |T_{11}|^2 - \frac{1}{4} \text{Re} \{ \xi_{11}^* T_{11} \}, \\ N_{20}^{(6)} &\equiv C_{20} = \frac{a_0^2}{2L_{Ti}^2} \text{Re} \left\{ ia_{11}^* T_{11} - \left[E \left(\frac{a_0}{L_{Ti}} \sqrt{i} \right) - 1 \right] w_{11}^* T_{11} \right\} + \frac{3a_0^2}{2L_d^2} |w_{11}|^2, \\ N_{20}^{(7)} &\equiv D_{20} = \frac{a_0^2}{2L_{Tv}^2} \text{Re} \left\{ \left(1 - \frac{2}{3\gamma} \right) ip_{11} a_{11}^* - \xi_{11} a_{11}^* + \xi_{11}^* T_{11} \right\}. \end{aligned}$$

Here $E(z)$ is the third-order exponential integral,

$$E(z) = \int_1^\infty \frac{1}{\eta^3} e^{-z(\eta-1)} d\eta,$$

and π_s'' is the dimensionless second derivative of the saturation pressure along the saturation curve. Using the Clapeyron-Clausius equation (III-19) for a perfect gas, we have

$$\pi_s'' = \frac{T^2}{p_s} \frac{d^2 p_s}{dT^2} \Big|_{T=T_\infty} = \frac{1 - k_s (1 - \rho) (2 - \rho)}{k_s^2 (1 - \rho)^3}.$$

From (IV-36), (IV-38), (IV-48), (IV-42), and (IV-49) we can obtain the following equation for rectified heat transfer:

$$\begin{aligned} \frac{\partial a_0}{\partial t_2} &= W_2(a_0), \quad V(a_0) = \left[1 + \frac{4(1-\rho)L_\mu^2}{L_p^2} M_{53}(a_0) - \frac{L_\beta}{a_0} M_{44}(a_0) \right]^{-1} \quad (\text{IV-49}) \\ W_2(a_0) &\equiv a_0 V(a_0) \left[-\frac{1}{\epsilon^2} M_{53} \left(\Delta + \frac{2L_\sigma}{a_0} \right) + M_{53} N_{20}^{(2)} - \frac{L_\beta}{a_0} \left(N_{20}^{(4)} - N_{20}^{(6)} - \lambda N_{20}^{(7)} \right) + \right. \\ &\quad \left. \left(1 - \frac{4\rho L_\mu^2}{L_p^2} M_{53} - \frac{L_\beta}{a_0} M_{44} \right) \left(\frac{1}{3\gamma} N_{20}^{(3)} - \frac{L_{Tv}^2}{a_0^2} N_{20}^{(7)} \right) + N_{20}^{(5)} \right]. \end{aligned}$$

This equation agrees in limiting cases with the equation for rectified heat transfer obtained using simplified models [37, 3, 17, 2]. Note that Equation (4.2) in Reference [2] contains misprints.

7. Third Order Approximation

It is noteworthy that the asymptotic scheme used does not provide uniformly valid expansions in orders higher than 2. The source of asymptotic singularity is connected with the infinite spatial region for the thermal problem in the liquid. Below we consider this problem in detail.

a. Spatial Matching of Asymptotic Expansions

The above procedure for solution of the thermal problem is correct for determination of the n th modes of fluxes when $n \neq 0$. At $n = 0$ the temporal derivatives with respect to t_0 in the left-hand side parts of equations (IV-16) and (IV-17) are zero. In this case the temporal derivative is treated in a straightforward way which causes a singularity of the asymptotic expansion (small parameter near the highest derivative). In the slow time scales a temperature perturbation propagates from the bubble to the bulk of liquid to characteristic distances $\eta \gg 1$, and the slow spatial scales should be considered. For the boundary value problem matching of inner and outer asymptotic expansions is an appropriate asymptotic procedure.

The inner problem for u_{m0} follows from (IV-16):

$$\frac{1}{\eta^2} \frac{\partial}{\partial \eta} \left(\eta^2 \frac{\partial u_{m0}}{\partial \eta} \right) = -f_{m0}, \quad u_{m0}|_{\eta=1} = T_{m0}, \quad u_{m0}|_{\eta=\infty} = \vartheta_{m0}, \quad (\text{IV-50})$$

where ϑ_{m0} is the matching constant to be determined. Solution of this problem is

$$u_{m0} = \vartheta_{m0} + \int_{\eta}^{\infty} x f_{m0}(x) dx + \frac{1}{\eta} \left\{ T_{m0} - \vartheta_{m0} - \int_1^{\infty} x f_{m0}(x) dx + \int_1^{\eta} x^2 f_{m0}(x) dx \right\}. \quad (\text{IV-51})$$

and for zero mode of the heat flux we have

$$q_{m0} = - \left. \frac{\partial u_{m0}}{\partial \eta} \right|_{\eta=1} = T_{m0} - \vartheta_{m0} - \int_1^{\infty} \eta f_{m0}(\eta) d\eta. \quad (\text{IV-52})$$

Comparing with (IV-26) we can determine

$$C_{m0} = \vartheta_{m0} + \int_1^{\infty} \eta f_{m0}(\eta) d\eta. \quad (\text{IV-53})$$

For simplicity we limit ourselves to the third order approximation requiring a one-term outer expansion. In this case it is enough to introduce one slow variable $\eta_2 = \epsilon \eta$ (otherwise we introduce for each time scale, t_k , its own slow spatial variable, $\eta_k = \epsilon^{k/2} \eta$, $k = 2, 3, \dots$) and consider a zero-order approximation, $u_0^{(o)}$, to outer solution $u^{(o)}$ (otherwise we consider a series, $u^{(o)} = u_0^{(o)} + \epsilon u_1^{(o)} + \dots$). The outer problem in slow scale (t_2, η_2) is therefore

$$\frac{a_0}{L_{T1}^2} \left(a_0 \frac{\partial u_0^{(o)}}{\partial t_2} - \eta_2 \frac{\partial a_0}{\partial t_2} \frac{\partial u_0^{(o)}}{\partial \eta_2} \right) - \frac{1}{\eta_2^2} \frac{\partial}{\partial \eta_2} \left(\eta_2^2 \frac{\partial u_0^{(o)}}{\partial \eta_2} \right) = 0, \quad (\text{IV-54})$$

Solution of this problem with the following initial and boundary conditions:

$$u_0^{(o)} \Big|_{t_2=0} = 0, \quad u_0^{(o)} \Big|_{\eta_2=\infty} = 0, \quad (\text{IV-55})$$

can be represented in the form

$$u_0^{(o)} = \frac{\epsilon^3 L_{T1}}{a_0(t_2) \eta_2} \left\{ \Phi_{20} \Big|_{t_2=0} \operatorname{erfc} \left[\frac{a_0(t_2, \dots) \eta_2}{2 L_{T1} \sqrt{t_2}} \right] + \int_0^{t_2} \frac{\partial \Phi_{20}(\zeta, \dots)}{\partial \zeta} \operatorname{erfc} \left(\frac{a_0(t_2, \dots) \eta_2}{2 L_{T1} \sqrt{t_2 - \zeta}} \right) d\zeta \right\},$$

where Φ_{20} is an arbitrary function of time.

To match this solution with the inner solution, we substitute $\eta_2 = \epsilon \eta$ and expand this expression at $\epsilon \rightarrow 0$:

$$u_0^{(o)} = \frac{\epsilon^2 L_{T1}}{a_0 \eta} \Phi_{20} - \frac{\epsilon^3}{\sqrt{\pi}} \left[\frac{\Phi_{20} \Big|_{t_2=0}}{\sqrt{t_2}} + \int_0^{t_2} \frac{\partial \Phi_{20}}{\partial \zeta} \frac{d\zeta}{\sqrt{t_2 - \zeta}} \right] + \dots \quad (\text{IV-56})$$

At the same time the two-term outer expansion of two terms of the inner solution, $u_0^{(i)}$, (IV-51) is:

$$u_0^{(i)} = \epsilon^2 u_{20} + \epsilon^3 u_{30} + \dots = \epsilon^2 \left\{ \vartheta_{20} + \frac{1}{\eta} \left[T_{20} - \vartheta_{20} + \int_1^{\infty} x(x-1) f_{20}(x) dx \right] \right\} + \epsilon^3 \vartheta_{30} + \dots \quad (\text{IV-57})$$

Here we used the fact that $f_{30} = 0$. This is true for harmonic oscillations, since the regular non-linearity of the equations generates modes 0 and 2 in the second order and modes 1 and 3 in the third order approximation.

Comparing (IV-56) and (IV-57) one can find:

$$\begin{aligned} \vartheta_{20} &= 0, & \Phi_{20} &= \frac{a_0}{L_{Tl}} (T_{20} + E_{20}), & E_{20} &= \int_1^\infty x(x-1) f_{20}(x) dx, \\ \vartheta_{30} &= -\frac{1}{\sqrt{\pi}} \left[\frac{\Phi_{200}}{\sqrt{t_2}} + \int_0^{t_2} \frac{\partial \Phi_{20}}{\partial \zeta} \frac{d\zeta}{\sqrt{t_2 - \zeta}} \right], & \Phi_{200} &= \Phi_{20}|_{t_2=0}. \end{aligned} \quad (\text{IV-58})$$

b. Equation for Rectified Heat Transfer

In the third order approximation we have

$$\begin{aligned} Y_{30}^{(1)} &= -\frac{1}{a_0} \frac{\partial a_0}{\partial t_3}, & Y_{30}^{(2)} &= 0, & Y_{30}^{(3)} &= -\frac{3\gamma}{a_0} \frac{\partial a_0}{\partial t_3}, \\ Y_{30}^{(4)} &= Y_{30}^{(5)} = 0, & Y_{30}^{(6)} &\equiv C_{30} = \vartheta_{30}, & Y_{30}^{(7)} &= 0. \end{aligned}$$

General conditions (IV-43) and (IV-42) provide us with the following equation:

$$\frac{\partial a_0}{\partial t_3} = W_3, \quad W_3 = L_\beta V(a_0) \vartheta_{30}. \quad (\text{IV-59})$$

The zero mode of temperature in the second order approximation can be found using (IV-39)-(IV-41), (IV-36), (IV-48) and (IV-49):

$$T_{20} = C_{20} + \lambda D_{20} - N_{20}^{(4)} + M_{44} \left(\frac{1}{a_0} W_2(a_0) + \frac{L_{T_v}^2}{a_0^2} D_{20} - \frac{1}{3\gamma} N_{20}^{(3)} \right). \quad (\text{IV-60})$$

We also can determine

$$E_{20} = \frac{1}{2} \operatorname{Re} \left\{ a_{11}^* T_{11} \left[1 + \frac{a_0 \sqrt{i}}{L_{Tl}} \right] + \frac{a_0^2}{L_{Tl}^2} E \left(\frac{a_0}{L_{Tl}} \sqrt{i} \right) w_{11}^* T_{11} \right\} + \frac{a_0^2}{2L_d^2} |w_{11}|^2. \quad (\text{IV-61})$$

Equations (IV-58), (IV-60) and (IV-61) specify Φ_{20} as a function of a_0 .

Generally, if we know equations in time scales t_2, t_3, \dots then we can introduce one slow time, $\tau = \epsilon^2 \omega t$, and represent the equation for rectified heat transfer in the form:

$$\frac{\partial a_0}{\partial \tau} = \frac{\partial a_0(t_2, t_3, \dots)}{\partial t_2} + \epsilon \frac{\partial a_0(t_2, t_3, \dots)}{\partial t_3} + \dots = W_2(a_0(\tau, \epsilon\tau, \dots)) + \epsilon W_3(\tau, \epsilon\tau, \dots; a_0(\tau, \epsilon\tau, \dots)) + \dots \quad (\text{IV-62})$$

Thus, we have for a_0 the following equation:

$$\frac{\partial a_0}{\partial \tau} = W_2(a_0) - \frac{\epsilon L_\beta V(a_0)}{\sqrt{\pi}} \left[\frac{\Phi_{200}}{\sqrt{\tau}} + \int_0^\tau \frac{d\Phi_{20}(a_0)}{da_0} \frac{\partial a_0(\zeta)}{\partial \zeta} \frac{d\zeta}{\sqrt{\tau - \zeta}} \right] + O(\epsilon^2). \quad (\text{IV-63})$$

The term W_3 reflects an important physical effect which shows that the growth rate depends not only on the current value of the bubble radius, but also on the history of the development of the thermal boundary layer. Mathematically the type of equation also changes from an ordinary differential equation in the second order approximation to a non-linear integro-differential equation in the third order approximation.

c. Thin Boundary Layers

The case $L_{Tl} \sim \epsilon a_0$ corresponds to a thin oscillating thermal boundary layer in the liquid and requires some special asymptotic treatment. In this case the thickness of the 'fast' boundary sublayer is of order $L_{Tl}/a_0 \ll 1$. The evolution of the 'slow' thermal boundary layer in the liquid occurs at $\eta - 1 \gg L_{Tl}/a_0$, which, therefore, is not limited by the case $\eta \gg 1$, which we considered earlier to treat the outer problem. Instead for the outer problem we need to consider in the third order approximation a general case $\eta \sim 1$.

Introducing the boundary layer variable, $\zeta_f = a_0(\eta - 1)/L_{Tl}$, we can represent the inner problem (IV-50) up to the third order approximation in the form

$$\begin{aligned} \frac{\partial^2 u_{20}}{\partial \zeta_f^2} &= -\frac{a_0^2}{L_{Tl}^2} f_{20}, & \frac{\partial^2 u_{30}}{\partial \zeta_f^2} &= 2 \frac{L_{Tl}}{\epsilon a_0} \frac{\partial u_{20}}{\partial \zeta_f}, \\ u_{20}|_{\zeta_f=0} &= T_{20}, & u_{20}|_{\zeta_f=\infty} &= u_0^{(o)}|_{\eta=1}, \\ u_{30}|_{\zeta_f=0} &= T_{30} = 0, & \frac{\partial u_{20}}{\partial \zeta_f} + \epsilon \frac{\partial u_{30}}{\partial \zeta_f} \Big|_{\zeta_f=\infty} &= \frac{\partial u_0^{(o)}}{\partial \eta} \Big|_{\eta=1}, \end{aligned}$$

where $u_0^{(o)}$ is the outer solution. Solving this problem and taking into account that $f_{30} = 0$ and $T_{30} = 0$ we can determine the zero-mode heat flux in the third order approximation (IV-52)

$$q_{30} = -\frac{a_0}{L_{Tl}} \frac{\partial u_{30}}{\partial \zeta_f} \Big|_{\zeta_f=0} = -\vartheta_{30}. \quad (\text{IV-64})$$

Solution of these equations allows us to determine the following relations between the outer problem and the boundary conditions and the heat flux:

$$u_0^{(o)}|_{\eta=1} = T_{20} + E_{20}, \quad \vartheta_{30} = \left(u_0^{(o)} + \frac{\partial u_0^{(o)}}{\partial \eta} \Big|_{\eta=1} \right), \quad (\text{IV-65})$$

where the function E_{20} can be computed using (IV-61) since it is a limiting form of (IV-58) at $L_{Tl}/a_0 \ll 1$.

Consider now the outer problem (the problem at $\eta \sim 1$). For simplicity we pass the mass flux term proportional to $\rho \ll 1$ and the heat source due to viscous dissipation $(L_{Tl}/L_d)^2 \ll 1$ to higher order approximations (see estimations (IV-19)). The outer problem will be then:

$$\frac{\epsilon^2 a_0^2}{L_{Tl}^2} \left[\frac{\partial u_0^{(o)}}{\partial t_2} - \frac{\partial \ln a_0}{\partial t_2} \left(\eta - \frac{1}{\eta^2} \right) \frac{\partial u_0^{(o)}}{\partial \eta} \right] - \frac{1}{\eta^2} \frac{\partial}{\partial \eta} \left(\eta^2 \frac{\partial u_0^{(o)}}{\partial \eta} \right) = 0, \quad (\text{IV-66})$$

subject to the following boundary conditions:

$$u_0^{(o)}|_{\eta=1} = T_{20} + E_{20}, \quad u_0^{(o)}|_{\eta=\infty} = 0. \quad (\text{IV-67})$$

This problem can be solved with the following initial conditions:

$$u_0^{(o)} \Big|_{t_2=0} = H(\eta), \quad (\text{IV-68})$$

where $H(\eta)$ is some initial temperature profile near the bubble. For a bubble generated in a liquid of uniform temperature one can set $H(\eta) \equiv 0$.

Generally solution of problem (IV-66)-(IV-68) can be obtained only numerically. This is the essence of a numerical-analytical method, which treats the problem in the third order approximation and requires numerical solution of the boundary value problem (IV-66)-(IV-68). Numerical solution allows us to determine ϑ_{30} in (IV-65) and evolve the bubble meanradius in a slow time scale according (IV-59) and (IV-62):

$$\frac{\partial a_0}{\partial \tau} = W_2(a_0) + \epsilon L_\beta V(a_0) \vartheta_{30}. \quad (\text{IV-69})$$

Note that this method generalizes the consideration given above. If we drop the asymptotic assumption $L_{T1}/a_0 \sim \epsilon \ll 1$ (consider $L_{T1}/a_0 \sim 1$) then we obtain analytical solution (IV-63).

8. Vapor-Gas Bubbles

The basic asymptotic technique for vapor-gas bubbles is similar to that described above for pure vapor bubbles. There are several differences, which we address in this section. The major difference is in the heat and mass transfer in the gas where the energy and diffusion equations are strongly coupled. The energy and diffusion equations in the liquid are also coupled, but only through the boundary conditions. They also have similarity, which does not require special solution of the diffusion problem, and equations for the energy equation can be used (a small term representing the heat source due to viscous dissipation may be dropped). Therefore the complex amplitudes of the boundary temperature and concentrations can be determined by solving a general system of linear equations in the m th order approximation, while the zero-modes of the heat and mass fluxes in the liquid will be related to the boundary values by similar relations as for a pure vapor. Such system can be solved in the second and the third order approximations to obtain an evolution equation of type (IV-69). In the present study we, however, limit ourselves to the first-order approximation to evaluate the influence of the inert gas component on the bubble forced oscillations.

a. Thermal and Diffusion Problems

In the first order approximation we seek solutions of the governing equations in the form:

$$\begin{aligned}
T_m &= T_\infty(1 + \epsilon \operatorname{Re} \{T'_m e^{i\omega t}\}), \quad T_{m0} = T_\infty, \quad m = l, g, a, \\
c_l &= c_{l0} + \epsilon \operatorname{Re} \{c'_l e^{i\omega t}\}, \quad c_i = c_{i0} + \epsilon \operatorname{Re} \{c'_i e^{i\omega t}\}, \quad c_{l0} = c_\infty, \\
p_g &= p_{g0}(1 + \epsilon \operatorname{Re} \{p'_g e^{i\omega t}\}), \quad a = a_0(1 + \epsilon \operatorname{Re} \{a'_g e^{i\omega t}\}), \\
w_{la} &= \omega a_0 \epsilon \operatorname{Re} \{w'_l e^{i\omega t}\}, \quad \xi = \omega \rho_{g0} a_0 \epsilon \operatorname{Re} \{\xi'_g e^{i\omega t}\}, \\
\xi_m &= \omega \rho_{g0} a_0 \epsilon \operatorname{Re} \{\xi'_m e^{i\omega t}\}, \quad m = i, v, \\
q_{ma} &= \frac{\lambda_{m0} T_{m0}}{a_0} \epsilon \operatorname{Re} \{q'_{ma} e^{i\omega t}\}, \quad j_{ma} = \frac{\rho_{m0} D_{m0}}{a_0} \epsilon \operatorname{Re} \{j'_{ma} e^{i\omega t}\}, \quad m = l, g.
\end{aligned}$$

Liquid

The heat and mass transfer in the liquid is described by equations

$$\begin{aligned}
iT'_l - \left(\frac{LT_l}{a_0}\right)^2 \frac{1}{\eta^2} \frac{\partial}{\partial \eta} \left(\eta^2 \frac{\partial T'_l}{\partial \eta}\right) &= 0, \quad T'_l|_{\eta=1} = T'_a, \quad T'_l|_{\eta=\infty} = 0, \\
ic'_l - \frac{1}{Le_l} \left(\frac{LT_l}{a_0}\right)^2 \frac{1}{\eta^2} \frac{\partial}{\partial \eta} \left(\eta^2 \frac{\partial c'_l}{\partial \eta}\right) &= 0, \quad c'_l|_{\eta=1} = c'_{la}, \quad c'_l|_{\eta=\infty} = 0.
\end{aligned}$$

Solution of these problems is well-known and can be found elsewhere [30]:

$$\begin{aligned}
T'_l &= \frac{T'_a}{\eta} \exp\left(-\frac{1+i a_0(\eta-1)}{\sqrt{2}} \frac{LT_l}{a_0}\right), \quad c'_l = \frac{c'_{la}}{\eta} \exp\left(-\frac{1+i a_0(\eta-1)}{\sqrt{2}} \frac{LT_l}{a_0}\right), \\
q'_{la} &= T'_a h \left(\frac{a_0}{LT_l}\right) = T'_a h_T, \quad j'_{la} = c'_{la} h \left(\frac{a_0 \sqrt{Le_l}}{LT_l}\right) = c'_{la} h_c, \quad h(z) = 1 + \frac{1+i}{\sqrt{2}} z.
\end{aligned}$$

Gas

The thermal and diffusion problems in the gas are coupled. It is convenient to represent them in the form

$$\begin{aligned}
i(T'_g - k_c c'_i - k_\gamma p') - \left(\frac{LT_g}{a_0}\right)^2 \frac{1}{\eta^2} \frac{\partial}{\partial \eta} \left(\eta^2 \frac{\partial T'_g}{\partial \eta}\right) &= 0, \quad T'_g|_{\eta=1} = T'_a, \quad (\text{IV-70}) \\
ic'_i - \frac{1}{Le_g} \left(\frac{LT_g}{a_0}\right)^2 \left[\frac{1}{\eta^2} \frac{\partial}{\partial \eta} \left(\eta^2 \frac{\partial c'_i}{\partial \eta}\right) + \frac{k_T}{\eta^2} \frac{\partial}{\partial \eta} \left(\eta^2 \frac{\partial T'_g}{\partial \eta}\right) \right] &= 0, \quad c'_i|_{\eta=1} = c'_{ia}.
\end{aligned}$$

Solution of these equations can be sought in the form

$$T'_g - k_\gamma p' \sim \frac{1}{\eta} \exp \lambda \eta, \quad c'_i \sim \frac{1}{\eta} \exp \lambda \eta.$$

The eigen values λ can be found from the characteristic equation

$$\left(\frac{LT_g}{a_0}\right)^4 \lambda^4 - i(Le_g + 1 + k_T k_c) \left(\frac{LT_g}{a_0}\right)^2 \lambda^2 - Le_g = 0.$$

This equation has four roots:

$$\begin{aligned}\lambda_m &= \frac{1+i}{\sqrt{2}} \frac{a_0}{Le_g} \sqrt{s_m}, & \lambda_{m+2} &= -\lambda_m, & m &= 1, 2, \\ s_{1,2} &= \frac{1}{2} \left\{ (Le_g + 1 + k_T k_c) \pm [(Le_g - 1)^2 + 2k_T k_c (Le_g + 1) + k_T^2 k_c^2]^{1/2} \right\}.\end{aligned}\quad (IV-71)$$

A non-singular solution in the domain $0 \leq \eta \leq 1$ can be written in the form:

$$\begin{aligned}T'_g - k_\gamma p' &= \frac{1}{\eta} [A_1 \sinh(\lambda_1 \eta) + A_2 \sinh(\lambda_2 \eta)], \\ c'_i &= \frac{1}{\eta} [B_1 \sinh(\lambda_1 \eta) + B_2 \sinh(\lambda_2 \eta)],\end{aligned}$$

where the constants of integration A_m and B_m can be found from equations and boundary conditions (IV-70). The heat and mass fluxes then can be found using relations (III-11). The dimensionless complex amplitudes of these fluxes can be represented in the following form

$$\begin{aligned}j'_{ga} &= c'_a f_c + (T'_a - k_\gamma p') f_T, & q'_{ga} &= c'_a g_c + (T'_a - k_\gamma p') g_T, \\ f_c &= 1 + \frac{r_1 - r_2}{s_1 - s_2}, & f_T &= k_T + i \frac{(1 - s_2) r_1 - (1 - s_1) r_2}{k_c (s_1 - s_2)}, \\ g_c &= \frac{k_c}{Le_g} \left(1 + \frac{q_1 - q_2}{s_1 - s_2} \right), & g_T &= \frac{1}{Le_g} \left[Le_g + k_T k_c + i \frac{(1 - s_2) q_1 - (1 - s_1) q_2}{s_1 - s_2} \right], \\ q_m &= [1 - s_m + i (Le_g + k_c k_T)] \lambda_m \coth \lambda_m, & r_m &= (1 - s_m + i k_c k_T) \lambda_m \coth \lambda_m, & m &= 1, 2.\end{aligned}$$

These relations can be substantially simplified for small concentrations of one of the components, when we have $k_T \rightarrow 0$ and, correspondingly :

$$s_1 = Le_g, \quad s_2 = 1,$$

$$\begin{aligned}f_c &= 1 - \lambda_1 \coth \lambda_1, & g_T &= 1 - \lambda_2 \coth \lambda_2, & f_T &= 0, \\ g_c &= \frac{k_c}{Le_g (1 - Le_g)} [(1 - Le_g) f_c + i Le_g (\lambda_2 \coth \lambda_2 - \lambda_1 \coth \lambda_1)].\end{aligned}$$

Note that since $g_c \neq 0$ we have some influence of the concentration profile on the heat flux. However, this influence is small (since c'_a should be small at small c_{a0}) and can be also neglected. So in this limiting case we can consider a decoupled system.

b. Equations for Complex Amplitudes

The set of linearized equations for complex amplitudes can be represented in the following dimensionless form

$$ia' - w' - \rho (\xi'_i + \xi'_v) = 0,$$

$$\begin{aligned}
-\frac{2L_\sigma}{a_0}a' + \left[i \left(1 + \frac{4L_\mu^2}{L_C a_0} \right) \left(\frac{a_0}{L_p} \right)^2 + 4 \left(\frac{L_\mu}{L_p} \right)^2 \right] w' - \left(1 + \frac{ia_0}{L_C} \right) p' &= -k_p \left(1 + \frac{ia_0}{L_C} \right), \\
(1 - k_\gamma) ip' + 3ia' + 3 \left(\frac{L_{Tg}}{a_0} \right)^2 \left(q'_{ga} + \frac{\alpha_g}{Le_g} j'_{ga} \right) - 3(\xi'_i + \xi'_v) &= 0, \\
\frac{1}{k_\gamma} \left(\frac{L_{Tg}}{a_0} \right)^2 \left(q'_{ga} - \frac{1}{\lambda} q'_{la} \right) - \frac{iL_{\sigma T}}{a_0} T'_a - \left(k_v + \frac{2\rho L_\sigma}{a_0} \right) \xi'_v - \left(k_i + \frac{2\rho L_\sigma}{a_0} \right) \xi'_i &= 0, \\
\chi_s T'_a + k_H c'_{la} - k_R c'_{ia} - k_{ic} p' - k_\beta \frac{a_0}{L_{\beta 1}} \xi'_i &= 0, \\
\pi'_s T'_a + k_R c'_{ia} - (1 - k_{ic}) p' - \frac{a_0}{L_{\beta 1}} \xi'_v &= 0, \\
\frac{1}{Le_g} \left(\frac{L_{Tg}}{a_0} \right)^2 j'_{ga} - c_{i0} \xi'_v + c_{v0} \xi'_i &= 0, \\
\frac{1}{\rho Le_i} \left(\frac{L_{Ti}}{a_0} \right)^2 j'_{la} - c_{i0} \xi'_v + (1 - c_{i0}) \xi'_i &= 0.
\end{aligned}$$

where

$$L_{\beta 1} = \frac{(1 - \rho) L_\beta}{k_v - 1 + \rho}.$$

From a computational viewpoint, it is easier to solve a 8x8 linear algebraic system directly than to derive an analytical form. We tried two standard routines: LU decomposition and Gauss-Jordan [71]. Both work well and provide fast and accurate solution of the above system.

Chapter V.

Asymptotic Technique For Standing Waves

For description of the vapor bubble motion in a standing acoustic wave we use the same multi-scale technique as for bubbles in isotropic acoustic fields. We limit ourselves to the second order approximation. There are some peculiarities for standing waves which we consider below in detail.

1. Asymptotic Expansions

In the case of standing waves we have additional unknowns compared to the case of vapor bubbles in isotropic fields, which we expand in the following asymptotic series:

$$x_b(t) = k^{-1}x_0(t_1, t_2, \dots) [1 + \epsilon x_1(t_0, t_1, \dots) + \dots], \quad (\text{V-1})$$

$$U_b(t) = p_s(T_\infty)(\rho_l C)^{-1} [\epsilon U_1(t_0, t_1, \dots) + \dots], \quad (\text{V-2})$$

$$m_b(t) = \frac{4}{3}\pi\rho_{v\infty}a_0^3 [1 + \epsilon\mu_1(t_0, t_1, \dots) + \dots]. \quad (\text{V-3})$$

We also have

$$\begin{aligned} \sin \{x_0 [1 + \epsilon x_1 + \dots]\} &= \sin x_0 \cos [\epsilon x_0 x_1 + \dots] + \cos x_0 \sin [\epsilon x_0 x_1 + \dots] \\ &= \sin x_0 + \epsilon x_0 x_1 \cos x_0 + \dots \\ \cos \{x_0 [1 + \epsilon x_1 + \dots]\} &= \cos x_0 \cos [\epsilon x_0 x_1 + \dots] - \sin x_0 \sin [\epsilon x_0 x_1 + \dots] \\ &= \cos x_0 - \epsilon x_0 x_1 \sin x_0 + \dots \end{aligned}$$

We can substitute these expansions together with expansions of variables used for description of bubble dynamics in isotropic fields into the governing equations and collect terms near the same powers of the small parameter ϵ . This yields the following additional equations related to the bubble translational motion:

$$\begin{aligned}
\frac{\partial \mu_m}{\partial t_0} - 3\xi_m &= Y_m^{(8)}, \\
x_0 \frac{\partial x_m}{\partial t_0} - \frac{L_p^2}{L_C^2} U_m &= Y_m^{(9)}, \\
\left(\frac{1}{2} + \rho\right) \frac{\partial U_m}{\partial t_0} + \frac{3K_\mu L_\mu^2}{a_0^2} U_m - g_r (3a_m - \rho\mu_m) &= Y_m^{(10)}.
\end{aligned}$$

The system matrix will be then modified:

$$\mathbf{M}_n \mathbf{X}_{mn} = \mathbf{Y}_{mn}, \quad (\text{V-4})$$

$$\begin{aligned}
\mathbf{M}_n &= \begin{pmatrix} in & -1 & 0 & -\rho & 0 & 0 & 0 & 0 & 0 & 0 \\ -2L_\sigma/a_0 & M_{22} & M_{23} & 0 & 0 & 0 & 0 & 0 & 0 & 0 \\ 3\gamma in & 0 & in & -3\gamma & 0 & 0 & 3\gamma L_{Tv}^2/a_0^2 & 0 & 0 & 0 \\ 0 & 0 & 0 & M_{44} & 0 & -1 & \lambda & 0 & 0 & 0 \\ 0 & 0 & M_{53} & 1 & -L_\beta/a_0 & 0 & 0 & 0 & 0 & 0 \\ 0 & 0 & 0 & 0 & H_n & -1 & 0 & 0 & 0 & 0 \\ 0 & 0 & -k_\gamma I_n & 0 & I_n & 0 & 1 & 0 & 0 & 0 \\ 0 & 0 & 0 & -3 & 0 & 0 & 0 & in & 0 & 0 \\ 0 & 0 & 0 & 0 & 0 & 0 & 0 & 0 & in x_0 & -L_p^2/L_C^2 \\ -3g_r & 0 & 0 & 0 & 0 & 0 & 0 & \rho g_r & 0 & M_{1010} \end{pmatrix}, \\
\mathbf{X}_{mn} &= \begin{pmatrix} a_{mn} \\ w_{mn} \\ p_{mn} \\ j_{mn} \\ T_{mn} \\ q_{mn} \\ r_{mn} \\ M_{mn} \\ x_{mn} \\ U_{mn} \end{pmatrix}, \quad \mathbf{Y}_{mn} = \begin{pmatrix} Y_{mn}^{(1)} \\ Y_{mn}^{(2)} \\ Y_{mn}^{(3)} \\ Y_{mn}^{(4)} \\ Y_{mn}^{(5)} \\ Y_{mn}^{(6)} \\ Y_{mn}^{(7)} \\ Y_{mn}^{(8)} \\ Y_{mn}^{(9)} \\ Y_{mn}^{(10)} \end{pmatrix},
\end{aligned}$$

$$M_{1010} = \frac{3K_\mu L_\mu^2}{a_0^2} + \left(\frac{1}{2} + \rho\right) in. \quad (\text{V-5})$$

The matrix \mathbf{M}_n has a non-zero determinant, and solution, \mathbf{X}_{mn} , can be obtained either analytically, or (which is easier due to unwieldy analytical formulas) numerically by standard methods of matrix inversion. Note that the first seven equations form an independent subsystem (similar

to the system for bubbles in isotropic acoustic fields). If solutions $X_{mn}^{(j)}$, $j = 1, \dots, 7$ are found then the rest of unknowns can be determined as

$$\begin{aligned} X_{mn}^{(8)} &= \frac{1}{in} (3X_{mn}^{(4)} + Y_{mn}^{(8)}), \\ X_{mn}^{(9)} &= \frac{1}{in x_0} \left(\frac{L_p^2}{L_C^2} X_{mn}^{(10)} + Y_{mn}^{(9)} \right), \\ X_{mn}^{(10)} &= \frac{1}{M_{1010}} \left[\rho g_r \frac{1}{in} \left(-3 \frac{in}{\rho} X_{mn}^{(1)} + 3X_{mn}^{(4)} + Y_{mn}^{(8)} \right) + Y_{mn}^{(10)} \right]. \end{aligned}$$

Let us now be more specific about the structure of the right hand side vector. As before we can represent the right hand side terms Y_{mn} in the form:

$$Y_{mn} = S_{mn} + N_{mn} + F_{mn}, \quad (V-6)$$

where S_{mn} is generated by slow time scale evolution of linear terms, N_{mn} is generated by non-linear terms, and F_{mn} is the external forcing. Slow time scale evolution components, $S_{mn}^{(k)}$, for $k = 1, \dots, 7$ are the same as in (IV-37), while the other $S_{mn}^{(k)}$ are:

$$\begin{aligned} S_{mn}^{(8)} &= -\frac{1}{a_0^3} \left[\delta_{n0} \frac{\partial a_0^3}{\partial t_m} + \sum_{j=1}^{m-1} \frac{\partial (a_0^3 \mu_{jn})}{\partial t_{m-j}} \right], \\ S_{mn}^{(9)} &= - \left[\delta_{n0} \frac{\partial x_0}{\partial t_m} + \sum_{j=1}^{m-1} \frac{\partial (x_0 \mu_{jn})}{\partial t_{m-j}} \right], \\ S_{mn}^{(10)} &= -\rho \sum_{j=1}^{m-1} \frac{\partial U_{jn}}{\partial t_{m-j}} - \frac{1}{2a_0^3} \sum_{j=1}^{m-1} \frac{\partial (a_0^3 U_{jn})}{\partial t_{m-j}}. \end{aligned}$$

Using the same notation for F_{mn} we can find that in our case only F_{m0} , F_{11} , and $F_{mn}^{(10)}$ are non-zero. As we showed in the previous section to realize the characteristic asymptotic form we need to satisfy condition (IV-37). We also have the instability of the undisturbed state due to the gravity. To bring it to the second order approximation we accept the following condition:

$$g_r \sim \epsilon^2. \quad (V-7)$$

2. Evolution in Slow Time Scales

To obtain equations describing evolution of the unknowns in slow time scales let us consider operator M_0 :

$$\mathbf{M}_0 = \begin{pmatrix} 0 & -1 & 0 & -\rho & 0 & 0 & 0 & 0 & 0 & 0 & 0 \\ -2L_\sigma/a_0 & 4L_\mu^2/L_p^2 & -1 & 0 & 0 & 0 & 0 & 0 & 0 & 0 & 0 \\ 0 & 0 & 0 & -3\gamma & 0 & 0 & 3\gamma L_{T_v}^2/a_0^2 & 0 & 0 & 0 & 0 \\ 0 & 0 & 0 & M_{44} & 0 & -1 & \lambda & 0 & 0 & 0 & 0 \\ 0 & 0 & M_{53} & 1 & -L_\beta/a_0 & 0 & 0 & 0 & 0 & 0 & 0 \\ 0 & 0 & 0 & 0 & 1 & -1 & 0 & 0 & 0 & 0 & 0 \\ 0 & 0 & 0 & 0 & 0 & 0 & 1 & 0 & 0 & 0 & 0 \\ 0 & 0 & 0 & -3 & 0 & 0 & 0 & 0 & 0 & 0 & 0 \\ 0 & 0 & 0 & 0 & 0 & 0 & 0 & 0 & 0 & -L_p^2/L_C^2 & 0 \\ -3g_r & 0 & 0 & 0 & 0 & 0 & 0 & 0 & \rho g_r & 0 & 3K_\mu L_\mu^2/a_0^2 \end{pmatrix} \quad (\text{V-8})$$

Note that the first 7 equations form a closed subsystem with a non-zero system matrix, $\mathbf{M}_{0,sub}$, having determinant

$$\det \mathbf{M}_{0,sub} = \frac{6\gamma(1-\rho)k_s L_\beta L_\sigma}{a_0^2}. \quad (\text{V-9})$$

Thus we can determine using Cramer's rule:

$$X_{m0}^{(i)} = \frac{\det \mathbf{M}_{0m,sub}^{(i)}}{\det \mathbf{M}_{0,sub}}, \quad i = 1, \dots, 7. \quad (\text{V-10})$$

All other equations including the slow-time scale evolution condition for the 7x7 subsystem are similar to those obtained for isotropic fields (??)-(IV-43).

The last two rows form of the system matrix \mathbf{M}_0 (see (IV-39)) correspond to equations

$$\begin{aligned} \frac{L_p^2}{L_C^2} U_{m0} &= -Y_{m0}^{(9)}, \\ -g_r(3a_{m0} - \rho\mu_{m0}) + 3K_\mu \frac{L_\mu^2}{a_0^2} U_{m0} &= Y_{m0}^{(10)}. \end{aligned}$$

Due to $a_{m0} = 0$ we can determine m_{m0} :

$$\rho g_r \mu_{m0} = 3K_\mu \frac{L_\mu^2 L_C^2}{L_p^2 a_0^2} Y_{m0}^{(9)} + Y_{m0}^{(10)}. \quad (\text{V-11})$$

We should notice however, that $\rho g_r \ll 1$. Thus we can set, as in the case with a_{m0} :

$$3K_\mu \frac{L_\mu^2 L_C^2}{L_p^2 a_0^2} Y_{m0}^{(9)} + Y_{m0}^{(10)} = 0, \quad \mu_{m0} = 0, \quad m = 1, 2, \dots \quad (\text{V-12})$$

The third and the last condition for the right hand side vector can be obtained if we consider the eighth equation:

$$-3\xi_{m0} = Y_{m0}^{(8)}. \quad (\text{V-13})$$

We have using (IV-41) and (IV-40):

$$Y_{m0}^{(8)} = -3 \frac{\det M_{0m,sub}^{(4)}}{\det M_{0,sub}} = \frac{1}{\gamma} Y_{m0}^{(3)} - 3 \frac{L_{Tv}^2}{a_0^2} Y_{m0}^{(7)}. \quad (\text{V-14})$$

Solutions of the system are not unique, and, as in the case with a_{m0} , arbitrary x_{m0} can be assigned. To specify a solution we set $x_{m0} = 0$ for $m = 1, 2, \dots$. In this case we also have $\langle x \rangle = x_0$.

3. Linear Approximation

In the linear approximation we have

$$\begin{aligned} S_{10}^{(1)} &= -\frac{1}{a_0} \frac{\partial a_0}{\partial t_1}, \quad S_{10}^{(3)} = -\frac{3\gamma}{a_0} \frac{\partial a_0}{\partial t_1}, \quad S_{10}^{(8)} = -\frac{1}{a_0^3} \frac{\partial a_0^3}{\partial t_1}, \quad S_{10}^{(9)} = -\frac{\partial x_0}{\partial t_1}, \\ S_{1n}^{(2)} &= S_{1n}^{(4)} = S_{1n}^{(5)} = S_{1n}^{(6)} = S_{1n}^{(7)} = S_{1n}^{(10)} = 0. \\ F_{11}^{(2)} &= -\left(1 + \frac{ia_0}{L_C}\right) \sin x_0, \quad F_{11}^{(10)} = -\frac{3}{2} \left(1 - \frac{2iK_\mu L_\mu^2}{a_0^2}\right) \cos x_0, \end{aligned}$$

Other $F_{1n}^{(j)}$ are zero.

Thus,

$$\frac{\partial a_0}{\partial t_1} = 0, \quad \frac{\partial x_0}{\partial t_1} = 0.$$

We can explicitly resolve (III-39) for the first-mode using Cramer's rule:

$$X_{11}^{(j)} = -\left(1 + \frac{ia_0}{L_C}\right) \frac{\Delta^{(j)}}{\det \mathbf{M}_1} \sin x_0, \quad j = 1, \dots, 7, \quad (\text{V-15})$$

where $\Delta^{(j)}$ are the same as (IV-47) for isotropic fields.

Then we can determine the complex amplitudes describing the bubble mass, position, and translational velocity:

$$\begin{aligned} \mu_{11} &= \frac{3}{i} \xi_{11}, \\ x_0 x_{11} &= \frac{1}{i} \frac{L_p^2}{L_C^2} U_{11}, \\ U_{11} &= -\frac{3}{L_{1010}} \left[g_r (a_{11} + i\rho \xi_{11}) + \frac{1}{2} \left(1 - \frac{2iK_\mu L_\mu^2}{a_0^2}\right) \cos x_0 \right]. \end{aligned}$$

4. Equation for Rectified Heat Transfer

Since a_0 does not depend on t_1 , the same is true for all other variables. Thus, the non-zero components of vector S in the second order approximation are

$$S_{20}^{(1)} = -\frac{1}{a_0} \frac{\partial a_0}{\partial t_2}, \quad S_{20}^{(3)} = -\frac{3\gamma}{a_0} \frac{\partial a_0}{\partial t_2}, \quad S_{20}^{(8)} = -\frac{3}{a_0} \frac{\partial a_0}{\partial t_2}, \quad S_{20}^{(9)} = -\frac{\partial x_0}{\partial t_2}. \quad (\text{V-16})$$

The non-zero forcing terms are

$$F_{20}^{(2)} = -\frac{1}{\epsilon^2} \left(\Delta + \frac{2L_\sigma}{a_0} \right) - \frac{1}{2} \left[\text{Re} \{x_0 x_{11}\} + \frac{a_0}{L_C} \text{Im} \{x_0 x_{11}\} \right] \cos x_0 + \frac{L_p^2}{8L_C^2} |U_{11} - i \cos x_0|^2$$

$$F_{20}^{(10)} = \frac{1-\rho}{\epsilon^2} g_r - \frac{3}{2} \left(\text{Re} \{a_{11}\} - \frac{K_\mu l_\mu^2}{a_0^2} \text{Im} \{a_{11}\} \right) \cos x_0$$

$$+ \frac{3}{4} \left(\text{Re} \{x_{11}\} - \frac{2K_\mu l_\mu^2}{a_0^2} \text{Im} \{x_{11}\} \right) x_0 \sin x_0.$$

The components of non-linear term N_{2n} (V-6) can be found in the second-order approximation from quadratic nonlinearities. The non-zero components include modes 0 and 2 which corresponds to the average fluxes and nonlinear doubling of the oscillation frequency. To obtain the equation of rectified heat transfer it is sufficient to consider just zero-mode vector N_{20} . After some algebra one can find the components of this vector in the following form:

$$N_{20}^{(8)} = 3 \text{Re} \{a_{11}^* \xi_{11}\}, \quad (\text{V-17})$$

$$N_{20}^{(9)} = 0,$$

$$N_{20}^{(10)} = -\frac{3}{2} \text{Re} \left\{ \left(\frac{K_\mu L_\mu^2}{a_0^2} a_{11}^* - \rho \xi_{11}^* \right) U_{11} \right\}.$$

Components $N_{20}^{(k)}, k = 1, \dots, 7$ are similar to those for isotropic fields (IV-49).

Therefore from conditions of existence of periodical solutions (IV-42) and (V-12) we can obtain the following equation for rectified diffusion in a standing acoustic wave:

$$\frac{\partial a_0}{\partial t_2} = W_2(a_0, x_0), \quad \frac{\partial x_0}{\partial t_2} = V_2(a_0, x_0), \quad (\text{V-18})$$

$$W_2(a_0, x_0) \equiv a_0 \left(1 + \frac{4(1-\rho)L_\mu^2}{L_p^2} M_{53} - \frac{L_\beta}{a_0} M_{44} \right)^{-1} \times$$

$$\left[M_{53} F_{20}^{(2)} + M_{53} N_{20}^{(2)} - \frac{L_\beta}{a_0} \left(N_{20}^{(4)} - C_{20} - \lambda D_{20} \right) + \right.$$

$$\left. \left(1 - \frac{4\rho L_\mu^2}{L_p^2} M_{53} - \frac{L_\beta}{a_0} M_{44} \right) \left(\frac{1}{3\gamma} N_{20}^{(3)} - \frac{L_{Tv}^2}{a_0^2} D_{20} \right) + N_{20}^{(5)} \right],$$

$$V_2 = \frac{L_p^2 a_0^2}{3K_\mu L_\mu^2 L_C^2} \left(F_{20}^{(10)} + N_{20}^{(10)} \right). \quad (\text{V-19})$$

Chapter VI.

Numerical Methods

For computation of bubble dynamics in acoustic fields we applied the following three numerical methods: a purely numerical integration of the detailed governing equations, the numerical-analytical method, and the analytical solutions described above. Each of these method has its own advantages and deficiencies, and the best method to use depends on the task performed. For example, for computation of bubble dynamics during relatively short times (of the order of hundreds of oscillation cycles) a purely numerical integration provides the best results in terms of accuracy and reasonable utilization of computational resources. This method, however, is not applicable for computation of bubble dynamics during the many thousands, and even millions of oscillation cycles required for bubble stabilization in an acoustic field. In this case the best results were obtained using the numerical-analytical method, which approximately utilizes the same computational resources as computations using analytical formulae. Despite the fact that the numerical-analytical method is much faster than the straight-forward numerical integration (computation of a test case of 3600 cycles of bubble oscillation required 30,000 times less CPU time for the numerical-analytical method than for the straight-forward method), it is still too slow for parametric studies such as the investigation of the equilibrium states, and the investigation of dependencies of bubble parameters in acoustic fields on multi-parameter inputs (say the accommodation coefficient, liquid superheat, acoustic amplitude, and frequency). For this task the best method is the analytical method.

We have developed several codes based on different models of vapor-gas bubbles. However here we describe the methods for pure vapor bubbles only which were the best tested and validated by comparisons with each other and with the methods used by other authors.

1. Straight-Forward Finite Difference Scheme

The system to be solved can be considered as a system of two algebraic equations and five time-derivative equations that include the mass conservation equation at the bubble surface (IV-1) to determine \dot{a} , the modified Rayleigh-Plesset equation (IV-2) to determine \dot{w}_{la} , the vapor energy integral (IV-2) to determine \dot{p}_v , and the two energy equations, (IV-5) and (IV-6), for the vapor and liquid temperature, respectively. Among the five time-derivative equations, the first three are ordinary differential equations, while the last two are partial differential equations. To solve the

partial differential equations, one can apply a finite difference scheme for the spatial derivative terms in equations (IV-5) and (IV-6). The infinite computational domain required in equation (IV-6), however, may cause difficulty in numerical implementation. For numerical convenience, we can further transform equation (IV-6) by specifying $\zeta = 1/\eta$, such that the computational domain of equation (IV-6) is from 1 to 0. In terms of ζ the liquid energy equation (IV-6) becomes

$$\frac{a^2}{\kappa_l} \frac{\partial T_l}{\partial t} - \zeta^4 \frac{\partial^2 T_l}{\partial \zeta^2} = \frac{a}{\kappa_l} (\dot{a}\zeta - w_{la}\zeta^4) \frac{\partial T_l}{\partial \zeta} + \frac{12\mu_l w_{la}^2}{\lambda_l} \zeta^6. \quad (\text{VI-1})$$

By applying the second order central differencing scheme for the spatial derivative terms, one can rewrite equations (IV-5) and (VI-1) as

$$\frac{\partial T_v}{\partial t} = \frac{(\gamma - 1)\dot{p}_v T_v}{\gamma p_v} + \left(\frac{\dot{a}}{a} + \frac{\dot{p}_v}{3\gamma p_v} \right) \eta \delta_\eta (T_v) + \frac{p_s(T_\infty) \kappa_v}{p_v T_\infty a^2} \left[\frac{T_v}{\eta^2} \delta_\eta (\eta^2 \delta_\eta (T_v)) - (\delta_\eta (T_v))^2 \right], \quad (\text{VI-2})$$

$$\frac{\partial T_l}{\partial t} = \frac{\kappa_l}{a^2} \left[\zeta^4 \delta_{\zeta\zeta} (T_l) - \frac{a}{\kappa_l} (\dot{a}\zeta - w_{la}\zeta^4) \delta_\zeta (T_l) + \frac{12\mu_l w_{la}^2}{\lambda_l} \zeta^6 \right], \quad (\text{VI-3})$$

where

$$\begin{aligned} \delta_\eta ()_i &= \frac{()_{i+1} - ()_{i-1}}{\eta_{i+1} - \eta_{i-1}}, & \delta_{\eta\eta} ()_i &= \frac{2}{\eta_{i+1} - \eta_{i-1}} \left[\frac{()_{i+1} - ()_i}{\eta_{i+1} - \eta_i} - \frac{()_i - ()_{i-1}}{\eta_i - \eta_{i-1}} \right], \\ \delta_\zeta ()_i &= \frac{()_{i+1} - ()_{i-1}}{\zeta_{i+1} - \zeta_{i-1}}, & \delta_{\zeta\zeta} ()_i &= \frac{2}{\zeta_{i+1} - \zeta_{i-1}} \left[\frac{()_{i+1} - ()_i}{\zeta_{i+1} - \zeta_i} - \frac{()_i - ()_{i-1}}{\zeta_i - \zeta_{i-1}} \right], \end{aligned}$$

If there are N_v and N_l nodes used for discretization in equations (VI-2) and (VI-3), respectively, then equations (VI-2) and (VI-3) can be considered as two sets of ordinary differential equations in the unknowns. Arranging a , w_{la} , p_v , and all T_{vi} and T_{li} into a single vector of unknowns \mathbf{X} , we can write equations (IV-1)-(IV-2), (VI-2), and (VI-3) in the form:

$$\dot{\mathbf{X}} = \mathbf{F}(\mathbf{X}, t). \quad (\text{VI-4})$$

The vector function \mathbf{F} is shorthand for the right hand sides of the equations. A fourth-order Runge-Kutta scheme is applied to integrate equation (VI-4) over time.

To start the time integration, the initial condition for the temperature distribution inside the bubble and in the liquid need to be specified. Usually we assume that the vapor and liquid temperature are initially uniform,

$$T_l|_{t=0} = T_v|_{t=0} = T_\infty. \quad (\text{VI-5})$$

During the time integration the boundary conditions for the temperature are satisfied by enforcing the zero flux at $\eta = 0$, and the temperatures at the interface and far from the bubble:

$$T_v|_{\eta=1} = T_l|_{\zeta=1} = T_a, \quad T_l|_{\zeta=0} = T_\infty. \quad (\text{VI-6})$$

To satisfy the zero flux boundary condition we specify $\dot{T}_{v1} = \dot{T}_{v2}$.

To obtain the bubble wall temperature, T_a , we solve two algebraic equations (IV-3) and (IV-4), where we use the following approximations for the saturation pressure and temperature consistent with the Clausius-Clapeyron equation:

$$p_s(T) = p_s(T_\infty) \exp \left[\pi'_s \left(1 - \frac{T_\infty}{T} \right) \right],$$

$$T_s(p) = T_\infty \left[1 - \frac{1}{\pi'_s} \ln \frac{p}{p_s(T_\infty)} \right].$$

Since (IV-3) and (IV-4) are nonlinear equations, an iteration procedure to determine T_a is required using p_v , q_{va} , and q_{la} obtained from the previous time step. We use the following converging scheme:

$$T_a^{n+1} = \frac{E_1(T_a^n)}{E_2(T_a^n)}, \quad (\text{VI-7})$$

where the superscript shows the number of iteration (for initial approximation we use the value of T_a from the previous time step), and functions $E_1(T_a)$ and $E_2(T_a)$ are calculated using the following formulae:

$$E_1(T_a) = E_0(T_a) + \frac{1}{a} \left(\frac{\lambda_v T_{v,N_v-1}}{\eta_{N_v} - \eta_{N_v-1}} - \frac{\lambda_l T_{l,2} (\zeta_2 + \zeta_1)^2}{4 (\zeta_2 - \zeta_1)} \right),$$

$$E_2(T_a) = E_0(T_a) + \frac{1}{a} \left(\frac{\lambda_v}{\eta_{N_v} - \eta_{N_v-1}} - \frac{\lambda_l (\zeta_2 + \zeta_1)^2}{4 (\zeta_2 - \zeta_1)} \right),$$

$$E_0(T_a) = \frac{\pi'_s \beta l p_s(T_\infty) T_s(p_v)}{T_\infty \sqrt{2\pi R_v T_a}} \left[\frac{T_\infty + k_s T_a}{T_\infty} - \frac{p_v a - 2\sigma}{\rho_l l a} + \frac{1}{2l} \left(\frac{1}{\rho_l} - \frac{R_v T_a}{p_v} \right)^2 \xi^2(T_a, p_v) \right] f(T_a, p_v),$$

$$\xi(T_a, p_v) = \frac{\beta p_s(T_\infty) \pi'_s T_a - T_s(p_v)}{\sqrt{2\pi R_v T_a} T_\infty} f(T_a, p_v),$$

$$f(T_a, p_v) = \frac{T_\infty}{\pi'_s (T_a - T_s(p_v))} \left[\exp \left\{ \pi'_s \left(1 - \frac{T_\infty}{T_a} \right) \right\} - \exp \left\{ \pi'_s \left(1 - \frac{T_\infty}{T_s(p_v)} \right) \right\} \right].$$

Since the thermal boundary layers on both sides of the bubble wall are very small and the gradient of temperature is usually large, a very fine grid must be created near the bubble wall on both sides to adequately resolve the thermal boundary layers. To avoid the use of large number of grid points in the computational domain, an unequal-spaced grid which has highly clustered points near the bubble wall on both sides is applied. Figure VI-1 shows a typical temperature distribution during the bubble oscillation and the grid distribution along the space.

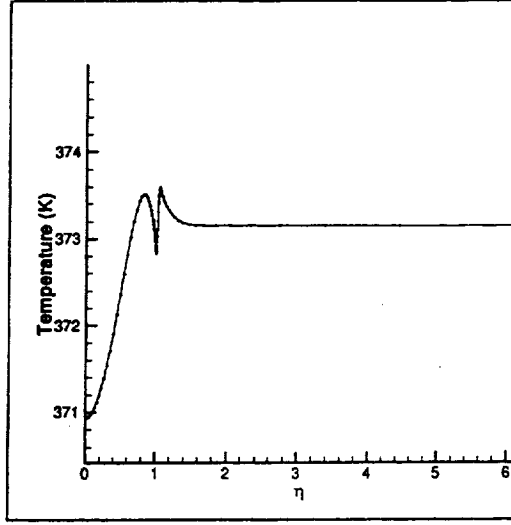


Figure VI-1: Typical temperature profile inside ($\eta < 1$) and outside ($\eta > 1$) a vapor bubble oscillating in an acoustic field. The dots on the curve correspond to nodes of the computational grid.

2. Numerical-Analytical Method

In this section we describe a numerical algorithm suitable for solution of the linear partial differential equation (IV-66). For convenience, we rewrite this equation in the form,

$$\epsilon \left[\frac{\partial u_0^{(o)}}{\partial t} - V \frac{\partial u_0^{(o)}}{\partial \eta} \right] - \frac{1}{\eta^2} \frac{\partial}{\partial \eta} \left(\eta^2 \frac{\partial u_0^{(o)}}{\partial \eta} \right) = 0, \quad (\text{VI-8})$$

where

$$\epsilon = \frac{\epsilon^2 a_0^2}{L_{T1}^2}, \quad V = \frac{\eta - 1}{\eta^2} \frac{\partial \ln a_0}{\partial t_2}.$$

The conversion, $u = \eta u_0^{(o)}$ transforms this equation into the one-dimensional heat conduction equation,

$$\epsilon \left[\frac{\partial u}{\partial t} - V \left(\frac{\partial u}{\partial \eta} - \frac{u}{\eta} \right) \right] - \frac{\partial^2 u}{\partial \eta^2} = 0, \quad (\text{VI-9})$$

with the same boundary conditions given by equation (IV-68).

We discretize time and the radial coordinate and approximate the first and the second spatial derivatives with second order of accuracy:

$$\frac{\partial u}{\partial \eta} \Big|_{\eta=\eta_m} = G_1 (u_{m+1} - u_m) - G_2 (u_{m-1} - u_m) \quad (\text{VI-10})$$

$$\frac{\partial^2 u}{\partial \eta^2} \Big|_{\eta=\eta_m} = S_1 (u_{m+1} - u_m) + S_2 (u_{m-1} - u_m), \quad (\text{VI-11})$$

where:

$$\begin{aligned} S_1 &= \frac{2}{(\eta_{m+1} - \eta_m)(\eta_{m+1} - \eta_{m-1})}, \\ S_2 &= \frac{2}{(\eta_m - \eta_{m-1})(\eta_{m+1} - \eta_{m-1})}, \\ G_1 &= \frac{1}{2} S_1 (\eta_m - \eta_{m-1}), \\ G_2 &= \frac{1}{2} S_2 (\eta_{m+1} - \eta_m). \end{aligned}$$

Applying the first order approximation to the time derivative and writing equation (VI-9) in the implicit manner results in a system of algebraic equations of the form,

$$-\alpha u_{m+1}^n + \beta u_m^n - \gamma u_{m-1}^n = u_m^{n-1}, \quad (\text{VI-12})$$

where

$$\begin{aligned} \alpha &= S_1 \Delta t / \varepsilon + G_1 p_m \Delta t, \\ \gamma &= S_2 \Delta t / \varepsilon - G_2 p_m \Delta t, \\ \beta &= 1 + \alpha + \gamma + p_m \Delta t / \eta_m. \end{aligned}$$

The tridiagonal system (VI-12) can be solved effectively by using a standard algorithm [71]. It assumes that the values of function u at the neighbouring nodes are linearly dependent,

$$u_{m-1}^n = A_{m-1} u_m^{n-1} + B_{m-1}. \quad (\text{VI-13})$$

Substituting equation (VI-13) into (VI-12) one can find that the coefficients A_m, B_m satisfy the following recurrent relations:

$$A_m = \frac{\alpha}{\beta - \gamma A_{m-1}}, B_m = \frac{u_m^{n-1} + \gamma B_{m-1}}{\beta - \gamma A_{m-1}}. \quad (\text{VI-14})$$

We assume that the temperature at the bubble boundary is prescribed, i.e., $A_1 = 0, B_1 = u_a(t_n)$, while at "infinity" the heat flux is zero, i.e. $u_M = B_M / (1 - A_M)$. Then, by applying successively

equations (VI-14) one can find the coefficients A, B and then back substitute them to find the sought function u . The outlined numerical procedure is absolutely stable because the coefficients A_m are less than unity, $|A_m| \leq 1$. This statement can be proven by deduction, since $A_1 = 0$ and $\beta - \gamma = 1 + \alpha > \alpha$.

The index M corresponds to the right boundary of the computational domain. The size of the computational domain expanded in time as the thickness on the bubble's boundary layer grows up. We used the following algorithm to track this expansion. First, we specified the dimension size L of the array corresponding to temperature, $u = T/\eta$, and we set, $M = L/2$, initially. Second, we computed the temperature distribution using equations (VI-13) and (VI-14) for the index range: $1 \leq m \leq K$, where $K = M + 10$. Then, we computed the spatial derivative $\partial u / \partial \eta$ and found index J such that $M \leq J \leq K$ and $|(\partial u / \partial \eta)_J| < 10^{-8}$. We updated the value of index M to J on the new time step. This procedure was repeated until index M reached the value of $L - 10$. When this happened the grid size was doubled and a cubic spline fit was applied to compute the temperature distribution corresponding to the new grid.

The dynamics of the mean bubble radius was then computed using the fourth-order Adams' extrapolation scheme. When solution for the average bubble radius was found, we computed the current bubble radius by superposition of the third-order solution for the mean bubble radius and the linear solution for the fast oscillating part:

$$a(t) = a_0(\tau) (1 + \epsilon \operatorname{Re}(a_{11} e^{i\omega t})). \quad (\text{VI-15})$$

3. Analytical Solutions

The analytical solutions were used mostly for investigation of the parameter space. Computation of the complex amplitudes of oscillation were performed analytically for the case of a pure vapor bubble and numerically, using LU-decomposition, for vapor-gas bubbles. The results for vapor-gas bubbles were verified by comparing the limiting case of pure vapor bubble with the case of vapor bubbles and with physical interpretation of the computed patterns. The results for vapor bubbles including the first-order and the second-order approximations were validated against limiting cases obtained earlier [2] when the surface tension, liquid viscosity and compressibility were neglected. To plot the phase portraits of the autonomous systems of type (V-18) were used and integrated with the Runge-Kutta 4th-order method.

For computation of the mean radius evolution in the third-order approximation nonlinear integro-differential equation (IV-63) was integrated using a Runge-Kutta 4th-order scheme with computation of the right hand side using an iterative scheme and evaluation of integrals based on a Gauss-type quadrature for modified Chebychev polynomials $C_n(x)$ (polynomials orthogonal on $[0,1]$, not $[-1,1]$):

$$\int_0^1 \frac{C_n(x)C_m(x)}{\sqrt{1-x^2}} dx = \delta_{nm}. \quad (\text{VI-16})$$

The weights and nodes of the Chebychev polynomials were found using standard procedures of

orthogonalization (e.g., [71]). In most cases 10 weights and nodes provided sufficient accuracy (tested by comparison with exact solutions for relative error below 10^{-6}).

After determination of the mean radius evolution, the current bubble radius was found by superposition of the first-order linear oscillation and the mean bubble radius according (VI-15).

4. Comparisons of Bubble Dynamics Computed by Various Methods

For validation of the numerical methods, we compared them with each other and with published computational results on vapor bubble dynamics in acoustic fields from Hao & Prosperetti (1999) [35], who used a straight-forward pseudospectral numerical method. The model used in Ref. [35] ignores the nonequilibrium phase transitions and is applicable for a low frequency field. To obtain a 'quasiequilibrium' scheme in our model, we set $\beta = 10^6$ (for the computed case of 1 kHz acoustic field and millimeter size bubbles the difference between computations with $\beta = 1$ and $\beta = 10^6$ were very small). Comparisons between all methods are shown in Figures VI-2 and VI-3.

The straight-forward numerical computations fall on top of the cited results [35]. The other two methods give results within 10% of relative error for maximum deviation with the straight-forward computations. Note that much smaller error (about 2%) was obtained for the mean bubble radius computed using the numerical-analytical method and the straight-forward methods. This is related to the use of formula (VI-15) which neglects the second and the higher harmonics of oscillations, and may be improved by inclusion of the second and the third-order terms in (VI-15). The lower curve presented in Fig. VI-2 was obtained using initially nonuniform (quasisteady, or hyperbolic) temperature profile in the liquid, which demonstrates the importance of selection of proper initial conditions.

Figures VI-4 and VI-5 show that agreement between the results obtained using the numerical-analytical method, the analytical solution and the straight-forward method is good.

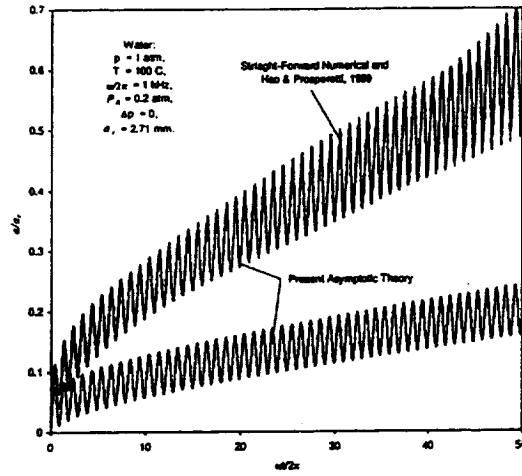


Figure VI-2: Comparison between computations based on the asymptotic theory with the initial quasisteady temperature profile in the liquid (the lower solid curve), initial uniform temperature profile in the liquid (the upper solid curve), and the numerical results of Hao & Prosperetti (1999) (the dashed curve), which are on top of our results using the purely numerical method and quasi-equilibrium scheme of phase transitions. The bubble radius is normalized with the primary resonance radius, 2.71 mm. The initial mean radius in the computations using the present theory is 0.1 mm.

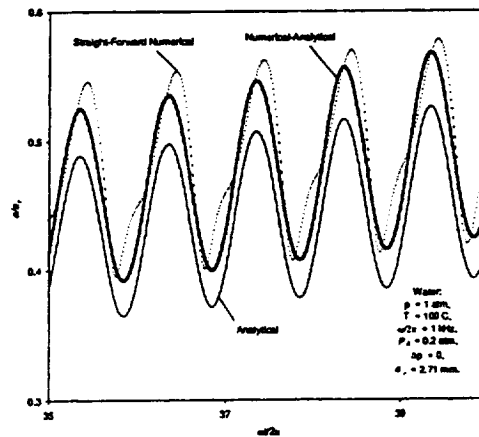


Figure VI-3: Comparisons of computations using the purely numerical method (the dashed curve), numerical-analytical method (the thick solid curve), and the third-order analytical solution (the thin solid curve).

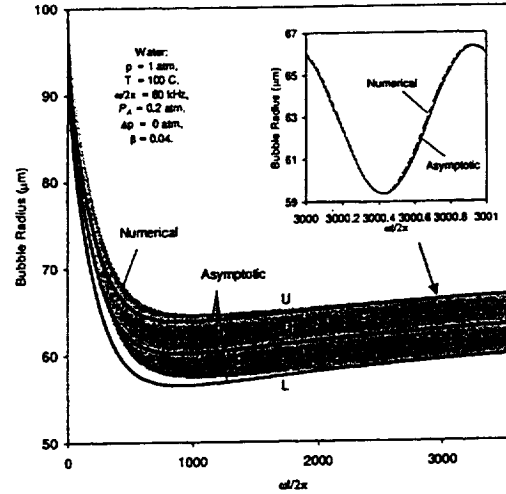


Figure VI-4: Comparison between computations using the third order asymptotic theory with the initial temperature jump ($\Phi_{200} = \Phi_{20}(a_{in})$, $a_{in} = 98 \mu\text{m}$; the solid curves) and purely numerical simulations with the initial bubble radius $100 \mu\text{m}$ using the detailed equations (the gray region and the dashed curve). Letters L, M, and U near the curves relates to the lower, mean, and upper slowly changing bubble radius. The curves L and U were computed by addition and subtraction of the amplitude of bubble oscillation predicted by the linear theory. The numerical-analytical method gives results close to the straight-forward computations.

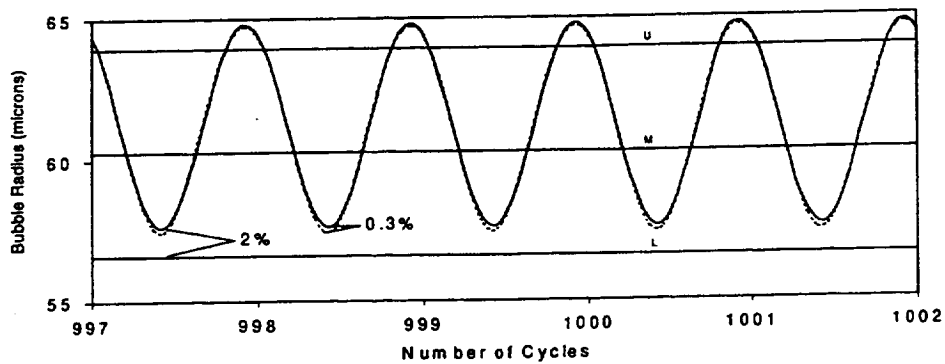


Figure VI-5: Comparison between the purely (the dashed curve) and the numerical-analytical method (the solid curve). The other notations and computation parameters correspond to the case shown in the previous figure.

Chapter VII.

Analysis of Linear Bubble Dynamics in Acoustic Fields

1. Vapor Bubbles

Computations for water and helium of vapor bubble dynamics in acoustic fields were carried out for a range of bubble sizes, frequencies, and amplitudes appropriate for the present theory. Since water and helium vapors deviate from perfect gas behavior (particularly true for helium at low temperatures) the property values given in Table 1 were utilized in computations. Other quantities, such as the gas constant and the specific heat ratio, were derived using the perfect gas relations.

Table 1. Properties of water and helium used in computations

Parameter	Unit	Water	Helium
T_{∞}	K	373	4.2
$p_s(T_{\infty})$	kPa	101	100
$\rho_{v\infty}$	kg/m ³	0.597	16.3
ρ_l	kg/m ³	958	125
c_{pv}	kJ/(kg·K)	2.03	2.2
c_l	kJ/(kg·K)	4.22	6.76
λ_v	mW/(m·K)	24.8	2.3
λ_l	mW/(m·K)	680	27.1
μ_l	$\mu\text{N}\cdot\text{s}/\text{m}^2$	279	3.57
C	km/s	1.54	0.18
l	km ² /s ²	2.26	0.0209
σ	mN/m	58.9	0.1

Figures VII-1 and VII-2 demonstrate typical dependences of the amplitude, $|a_{11}|$, and phase, $\arg(a_{11})$, of bubble radius oscillations on the average bubble radius, a_0 . Computations were performed using (IV-46) and (IV-47) for water at 1 atm and an acoustic frequency of 60 kHz. Qualitatively the dependence is the same for water at different pressures and frequencies or for other

liquids. Two limiting cases exist: the case of equilibrium (or more precisely quasi-equilibrium) phase transitions where we assume that the vapor pressure is equal to the saturation pressure at the interface temperature, and the case of the absence of phase transitions where $\beta = 0$. The equilibrium case can be formally obtained if we set $\beta = \infty$ despite the actual value of β cannot exceed 1. The computed curves show that the linear response of the vapor bubble to acoustic excitation strongly depends on β . The two limiting cases determine two resonances. For $\beta = 0$ we have only the primary resonance due to the liquid inertia and the vapor elasticity typical for gas bubbles. In the case of equilibrium phase transitions an additional low-frequency ("second") resonance due to phase transition and surface tension takes place. For water vapor bubbles at moderate β the amplitude of oscillation at the primary resonance is smaller than at the second resonance. For small β the bubble response curves show strong primary resonance. Note that at $\beta = 0$ formally there exists the "second" resonance at $a \approx 2\sigma/(3p_s)$. However to reach this resonance we need to have $\Delta p = -3p_s$ which corresponds to negative liquid pressure. This fact was discussed earlier by Khabeev [30]. Moreover, results for small bubble sizes below the theory limit line in Figures VII-1 and VII-2 violate assumption (III-37) and are not justified by the present theory.

To obtain more insight into the nature of the vapor bubble resonances, it is convenient to represent the bubble oscillator in the form:

$$\ddot{a}' + \mu \dot{a}' + \omega_n^2 a' = -p', \quad (\text{VII-1})$$

where μ is the dissipation coefficient, ω_n is the bubble natural frequency, and a' and p' are the nondimensional bubble radius and driving pressure. μ and ω_n depend on the mean bubble size, a_0 , the driving frequency, the accommodation coefficient and other properties of the liquid and its vapor. The natural frequency ω_n can be found from equation (VII-1) by substituting there the expression for the driving pressure and the linear solution for the bubble radius. Fig. VII-3 shows $\omega_n(a_0; \beta)$. It is seen that the natural frequency of vapor bubbles is very different from that of gas bubbles, and it is strongly influenced by β . At very small β a vapor bubble behaves similar to a gas bubble, while at relatively large β (in the computed case $\beta \gtrsim 0.1$) the bubble natural frequency is below the driving frequency for any bubble size, and there are no resonant sizes at all (for smaller acoustic frequencies there are two resonant sizes for large β also). For bubbles smaller than some critical size, we have $\omega_n^2 < 0$ which is an effect of surface tension specific for bubbles with phase transitions. Such bubbles are exponentially unstable in the absence of external forcing, while they can be stabilized by an acoustic field and behave similar to the bubbles of resonant frequencies much smaller than the driving frequency.

Figure VII-4 illustrates the temperature profiles inside and outside the bubble at a fixed moment of time ($t_0 = 2\pi n$). Computations were made for 50 μm bubbles using analytical solutions (IV-23) and (IV-23). All parameters were the same for all plotted curves, except for the value of the accommodation coefficient. It is seen that in the illustrated cases, β substantially influences the temperature distribution in the vapor. The influence of β on the temperature in the liquid is less, and there is no visible difference between computations with $\beta = 0.04$ and $\beta = \infty$. At smaller β , the temperature gradients in the vapor are much higher than those predicted by the quasi-equilibrium theory, and the heat flux in the vapor can be comparable with the heat flux in the liquid. This affects the interface temperature and the temperature profiles in the liquid.

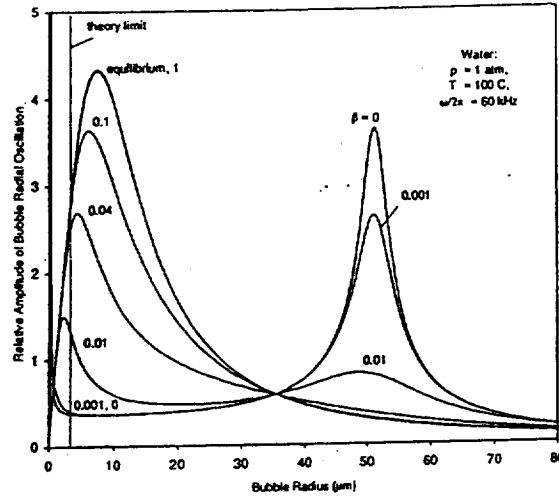


Figure VII-1: Relative amplitude of the forced vapor bubble radial oscillation in a 60 kHz acoustic field. The numbers near the curves show the values of the accommodation coefficient, β . The curve marked as "equilibrium" is computed using the quasi-equilibrium scheme of phase transition.

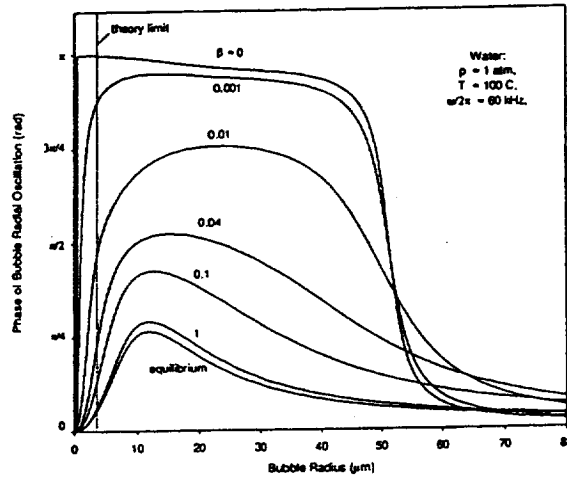


Figure VII-2: Phase shift between the driving pressure and forced radial bubble oscillation. Notations are the same as in the previous figure.

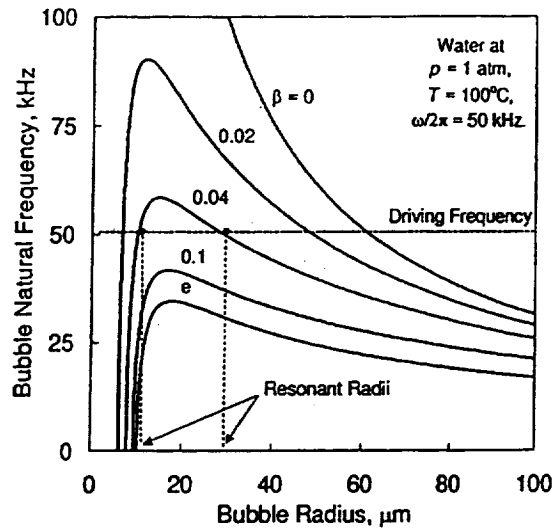


Figure VII-3: The vapor bubble natural frequency vs the bubble mean radius in an acoustic field at various values of the accommodation coefficient. The curve 'e' corresponds to the quasi-equilibrium scheme of phase transitions.

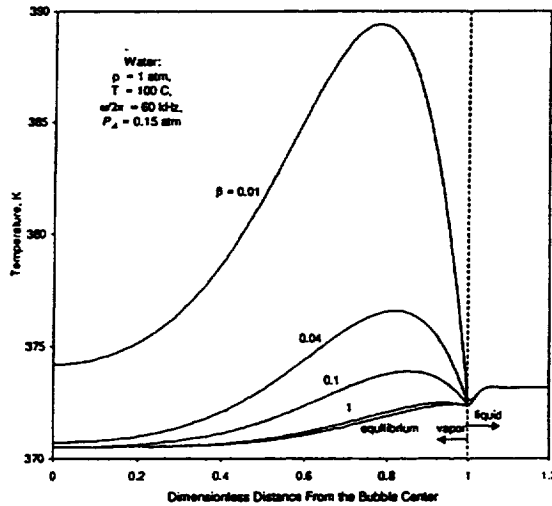


Figure VII-4: Temperature profiles predicted by the linear theory at various values of the accommodation coefficient shown near the curves and the quasi-equilibrium phase transition, marked as "equilibrium". Profiles are computed for a vapor bubble of radius $50\mu\text{m}$ at the phase of oscillation corresponding to $t = 0$.

2. Vapor-Gas Bubbles

Computations of the complex amplitudes of forced bubble oscillation were performed for a water-air system at atmospheric pressure and temperatures close to the water boiling point. Parameters varied include the frequency of the acoustic field, bubble size, concentration of the inert gas inside the bubble, concentration of the dissolved gas, vapor and inert gas accommodation coefficients, and the thermal diffusion coefficient. The basic properties of the system are given in the Table 2 below. All other properties were derived using relations for perfect gas mixtures. The values of C_{pg} at different concentrations were found by linear interpolation between limiting values for pure components. The values of κ_g and λ_g were assumed constant, since for the given system these quantities experience relatively small variations at changing concentration.

Table 2. Properties of water-air system used in computations
(The empty cells correspond to the values automatically computed or not in use)

Parameter	Unit	Liquid	Vapor	Air	Vapor-Air	Interface
T_∞	K	373	373	373	373	373
$p_s(T_\infty)$	kPa					101
D_l, D_g	mm ² /s	0.011			37.8	
κ_l, κ_g	mm ² /s	0.168			20.4	
λ_l, λ_g	mW/(m·K)	680			24.8	
R_v, R_i	kJ/(kg·K)		0.455	0.29		
c_{pv}, c_{pi}	kJ/(kg·K)		2.03	1.01		
ρ_l	kg/m ³	958				
μ_l	μN·s/m ²	279				
C	km/s	1.54				
l_v	km ² /s ²					2.26
l_i	km ² /s ²					0
H	GPa					6.73
dH/dT	GPa/K					0
σ	mN/m					58.9
$d\sigma/dT$	mN/(m·K)					0

Figures VII-5 and VII-6 demonstrate the frequency dependence of the normalized amplitude and phase of the bubble radius oscillation. Various curves in the figure correspond to various concentrations of the inert gas inside the bubble with other fixed parameters (the coefficients k_c and k_T vary since they depend on the content of the gaseous phase). The case of $c_{i0} = 1$ corresponds to the case of a pure gas bubble, and $c_{i0} = 0$ to the case of a pure vapor bubble. The latter limiting case was verified for consistency with the previous computational results. At $c_{i0} = 1$ strong primary resonance is observed. The amplitude of the bubble oscillation at the primary resonance frequency decreases at decreasing concentration of the inert gas. In the range of inert gas concentrations between 1 and 10% an interesting effect of low-frequency resonance (or, rather, instability) is observed. As can be seen in the figure, the amplitude of a 10 μm bubble oscillation drastically increases at $c_{i0} = 0.04$ and frequencies of order 1 kHz. This resonance is controlled by the surface tension and the two-component nature of the bubble content.

This resonance was first reported by Nagiev & Khabeev [65]. They explained it by the qualitative difference between the low-frequency response of the vapor bubble, which oscillates in phase with the forcing pressure (due to the effects of surface tension and evaporation-condensation maintaining the vapor pressure on the saturation line), and the bubble of non-condensable gas, which oscillates in anti-phase to the forcing pressure (due to stiffness of constant mass gas). The bubbles containing a mixture of non-condensable gas and vapor can oscillate in any phase in between 0 and π with the external low-frequency field depending on the concentration. At some critical concentration [65] (in our case $c_{i0} \approx 0.04$) a switch occurs between these two qualitatively different cases which causes the type of resonance behavior shown in the figure. This mechanism is different from the condensation-evaporation 'second' resonance for pure vapor bubbles [32, 34, 35].

Note that at very low frequencies the gas-vapor bubble will oscillate in phase with the forcing pressure due to dissolution of the inert gas. Theories which neglect gas diffusion in the liquid [65, 66] provide different low-frequency limits for the phase and amplitude of the bubble oscillation. We compared our computations with published results of other authors [65] and found qualitative agreement for the range of frequencies over which diffusion in the liquid is negligible. We also found some quantitative differences, which can be explained by the differences in the models used.

Figures VII-7 - VII-10 show the dependencies of the amplitude and phase of the bubble radius oscillation on the mean bubble size for a fixed frequency. Computations were performed for different contents of the gaseous phase. In all cases the 'second' resonance is observed in addition to a strong primary resonance. Generally, the second resonance is caused by the effects of surface tension and phase transitions. In the limiting cases of $c_{i0} = 1$ and $c_{i0} = 0$, phase transitions are due to dissolution and condensation-evaporation of one-component gas (or vapor). The phase transitions of a two-component mixture are more complex and lead to anomalous behavior of the 'second' resonance as discussed above. The characteristic times of condensation are controlled by the liquid thermal diffusivity and times of dissolution are controlled by the liquid mass diffusivity which are usually of different orders of magnitude (Lewis numbers of liquid are usually large, $Le_l \gg 1$). This creates two distinct size/frequency scales: 1) $a_0 \lesssim Le_l^{-1/2} L_{Ti}$ and 2) $a_0 \gg Le_l^{-1/2} L_{Ti}$, where the inert gas can be considered as soluble or non-soluble, respectively.

Effects related to gas dissolution can be important in the low-frequency/small-radius range $a_0 \lesssim Le_l^{-1/2} L_{Ti}$. In range $a_0 \gg Le_l^{-1/2} L_{Ti}$ we do not expect such parameters as the inert gas accommodation coefficient, the Henry constant, and the concentration of the dissolved gas to influence bubble oscillations. To demonstrate this point we performed computations at different β_i and H with other parameters fixed for different frequencies (see Figures VII-11 and VII-12). First, we found that the effect of non-equilibrium dissolution of the gas can be observed only at extremely low β_i . Already $\beta_i = 10^{-6}$ produces results close to the quasi-equilibrium phase transition of the inert gas (this case formally correspond to $\beta_i = \infty$). However, the models of non-soluble gas and soluble gas show a difference in the low frequency range $a_0 \lesssim Le_l^{-1/2} L_{Ti}$. If the values of β_i below 10^{-6} (which means that less than one-millionth part of gas molecules hitting the interface experience phase transition) are not of interest, within the frequency range $a_0 \lesssim Le_l^{-1/2} L_{Ti}$ (and therefore everywhere) the quasi-equilibrium scheme of phase transition for the inert gas is acceptable. The effect of the Henry constant on the bubble oscillations is appreciable in frequency range $a_0 \lesssim Le_l^{-1/2} L_{Ti}$ and negligible for frequencies of range $a_0 \gg Le_l^{-1/2} L_{Ti}$. Note that for 10 μm bubbles the effects of gas dissolution are negligible at frequencies of the order 100

Hz. The same is true for larger bubbles and higher frequencies. Therefore a simplified model neglecting the effects of gas diffusion in the liquid and dissolution is applicable for a wide range of bubble sizes and frequencies. For slow processes, such as rectified diffusion, the diffusion and phase transitions of the inert gas are important in slow time scales, but can be neglected in the fast time scale that is inversely related to the frequency of the field.

While the effect of nonequilibrium phase transition for the inert gas is negligible, the effect of the nonequilibrium phase transitions for the vapor component is strong in high frequency acoustic fields. Similarly, for a gas-vapor bubble with appreciable vapor component, the vapor accommodation coefficient influences the bubble dynamics (Figure VII-13-VII-14). Although the value of the accommodation coefficient cannot exceed 1, we made computations using very high values of this coefficient to determine if the scheme of quasi-equilibrium phase transitions (the bubble interface temperature is equal to the saturation temperature) is applicable. It is seen that such computations indicated as 'equilibrium' are close to the computations with $\beta_v = 1$. Curves for $\beta_v = 0.1$ substantially differ from the equilibrium curves. Therefore the quasi-equilibrium scheme of phase transitions is applicable if β_v is about unity. For very small radii, the effects of the inert gas dissolution create a resonance discussed above. Such influence of the vapor accommodation coefficient on the character of forced vapor-gas bubble oscillations suggests that measurements of this coefficient can be performed not only with pure vapor bubbles, but with vapor-gas bubbles with substantial inert gas content.

It is generally accepted that the nonequilibrium character of condensation/evaporation should be taken into account only for high frequency fields (e.g.[35]). This also depends on the bubble size, and, as we found, on the concentration of the inert component. As an example we show in Figures VII-15 and VII-16 computations of a 10 μm bubble response to acoustic perturbations over a wide range of frequencies with concentrations of the inert gas near the critical value ($c_{i0} = 0.05$). It is seen that the second resonance frequency and the bubble complex amplitude at frequencies of about 1 kHz depend substantially on the value of the vapor accommodation coefficient for $\beta_v \lesssim 0.1$.

The dependence of the amplitude and phase of vapor-gas bubble oscillation on the accommodation coefficient can be used for determination of the value of β_v . For efficient diagnostic procedures the bubble size, the frequency of the acoustic field, and the concentration of the inert component should be selected from the range corresponding to the highest sensitivity of bubble dynamics to the value of this coefficient. An example shown in Figures VII-17 and VII-18 demonstrates dependencies of the amplitude and phase of forced bubble oscillations on β_v at different concentrations of the dissolved gas, which can be selected arbitrary for a nonequilibrium vapor-gas bubble. It is seen that for $\beta_v \lesssim 0.1$ the parameters of oscillations strongly depend on β_v for small and moderate c_{i0} . Larger β_v can be determined from the bubble dynamics at relatively small c_{i0} since at higher c_{i0} the parameters of oscillations are not influenced by the value of β_v . It is interesting that the maximum slope of the curves for the amplitude of oscillation at $\beta_v \sim 1$ is realized at intermediate values of c_{i0} (in our case $c_{i0} \approx 0.1$), which indicates that addition of 10% of inert gas can be beneficial for diagnostics of β_v .

If $\beta_v \lesssim 0.1$, then its detection can be performed using the dynamics of bubbles of various sizes. However, for detection of larger values of β_v smaller sizes provide better resolution. The curves shown in Figure VII-19 and ?? demonstrate that in the specified range of parameters, the detection of β_v for water can be problematic for bubbles of radius 30 μm and higher if $\beta_v \gtrsim 0.4$.

Figures VII-21 and VII-22 show that for the best resolution in determination of relatively large β_v , the frequency of the acoustic field should be properly selected. Both high frequency and low frequency curves show a weak dependence on β_v in region $\beta_v \gtrsim 0.1$, while intermediate frequencies of the order 50 kHz provide the highest sensitivity to the value of the accommodation coefficient.

The influence of the Soret-Dufour, or thermodiffusion, effect on bubble forced oscillations in an acoustic field can be determined by variation of the thermal diffusion ratio, k_T , or related thermodiffusion coefficient k_c (III-12). Figures VII-23 and VII-24 display dependencies of the amplitude and phase of bubble radius oscillation on the mean bubble radius computed at different values of k_c . From (III-13) we have $k_c = 1.37$. Variation of k_c over a moderate range (limiting case $k_c = 0$ corresponds to the absence of the Soret-Dufour effect) shows its appreciable influence on the vapor-gas bubble response, especially for sizes near the primary resonance value. One possible applications of this observation is measurement of the thermodiffusion coefficient using vapor-gas bubble dynamics.

To demonstrate the Soret-Dufour effect the dimensionless temperature and concentration profiles realized inside an oscillating bubble at times $\omega t = 2\pi n$ are shown in Figures VII-25 and VII-26. The bubble size is selected to be close to the primary resonance at the given frequency. The computations were performed for different values of k_c . The results show that larger gradients of temperature and concentration inside the bubble are realized due to the Soret-Dufour effect. The amplitude of concentration oscillation near the bubble surface increases with k_c . This may explain the increase of the amplitude of bubble oscillation because larger amounts of inert gas near the surface make phase transition more difficult and increase the stiffness of the bubble.

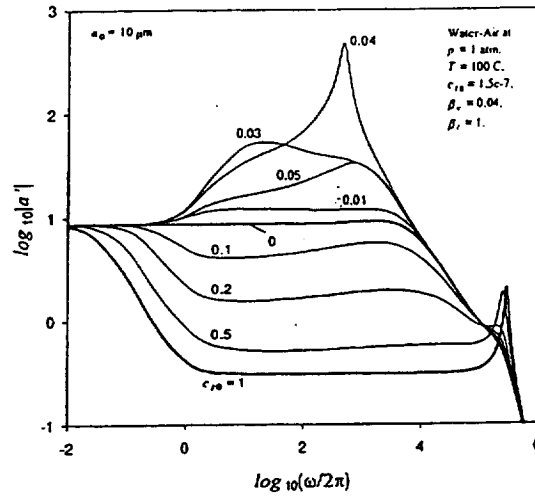


Figure VII-5: Relative amplitude of the forced vapor-gas bubble radial oscillation for $10\text{ }\mu\text{m}$ bubble in water as a function of the acoustic frequency. The numbers near the curves show the value of the inert gas concentration inside the bubble.

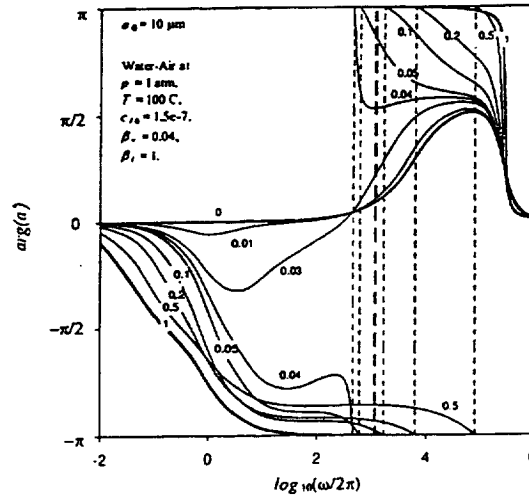


Figure VII-6: Phase shift between the driving pressure and the forced vapor-gas bubble radial oscillation for $10\text{ }\mu\text{m}$ bubble in water as a function of the acoustic frequency. The numbers near the curves show the value of the inert gas concentration inside the bubble.

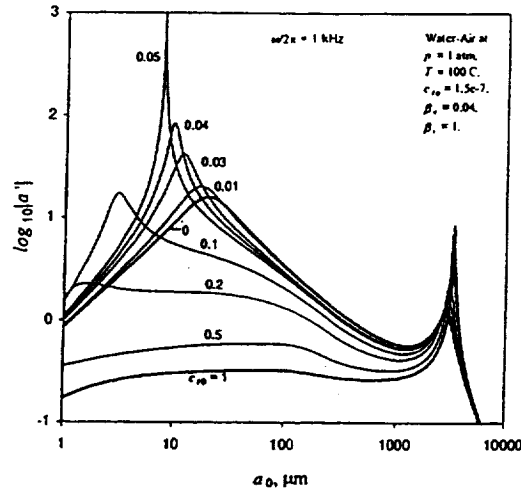


Figure VII-7: Relative amplitude of the forced vapor-gas bubble radial oscillation in 1 kHz acoustic field as a function of the bubble radius. The numbers near the curves show the value of the inert gas concentration inside the bubble.

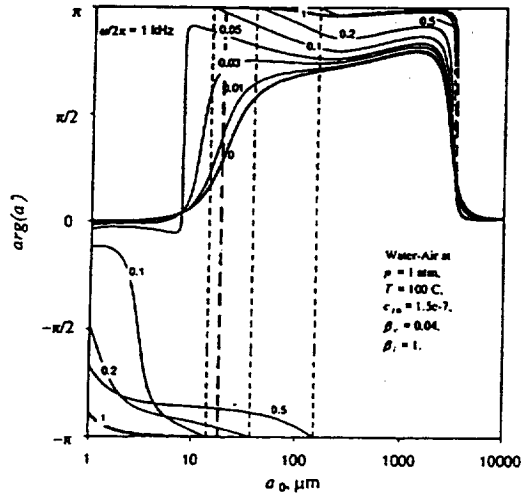


Figure VII-8: Phase shift between the driving pressure and the forced vapor-gas bubble radial oscillation in 1 kHz acoustic field as a function of the bubble radius. The numbers near the curves show the value of the inert gas concentration inside the bubble.

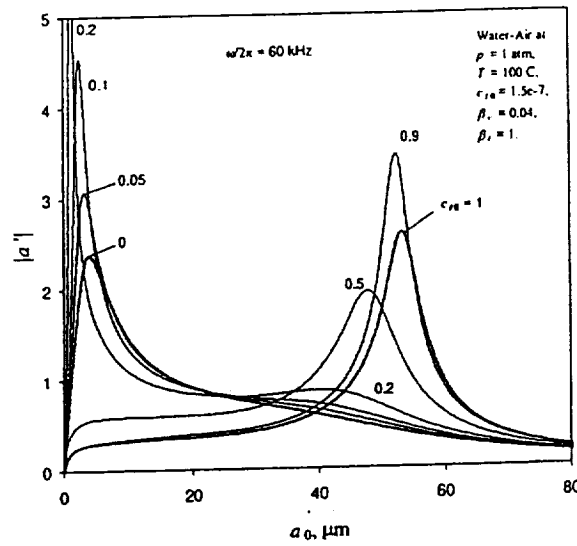


Figure VII-9: Relative amplitude of the forced vapor-gas bubble radial oscillation in 60 kHz acoustic field as a function of the bubble radius. The numbers near the curves show the value of the inert gas concentration inside the bubble.

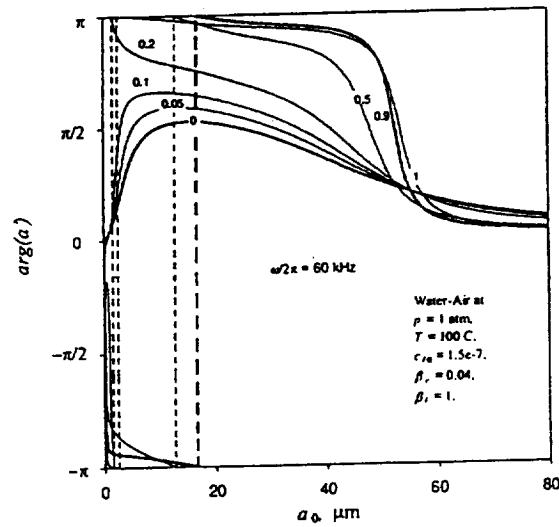


Figure VII-10: Phase shift between the driving pressure and the forced vapor-gas bubble radial oscillation in 60 kHz acoustic field as a function of the bubble radius. The numbers near the curves show the value of the inert gas concentration inside the bubble.

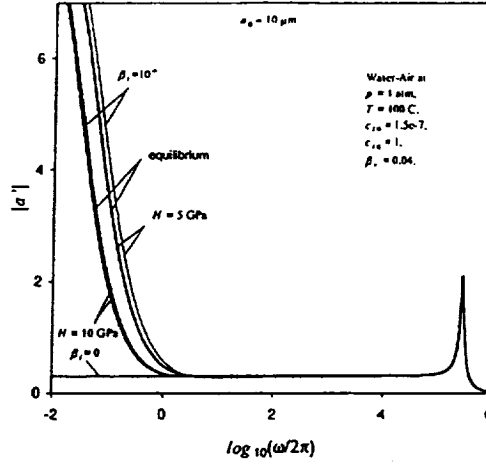


Figure VII-11: Relative amplitude of the forced vapor-gas bubble radial oscillation for 10 μm bubble in water as a function of the acoustic frequency. Computations are performed for different values of the inert gas accommodation coefficient, β_i , and the Henry constant, H (the values are shown near the curves). The thick curves marked 'equilibrium' correspond to quasi-equilibrium phase transition of the inert component.

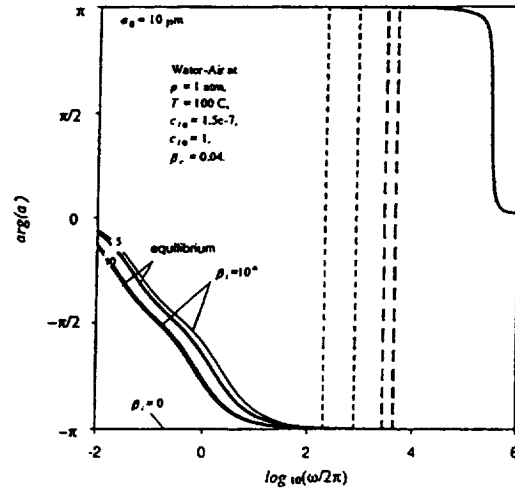


Figure VII-12: Phase shift between the driving pressure and the forced vapor-gas bubble radial oscillation for 10 μm bubble in water as a function of the acoustic frequency. Computations are performed for different values of the inert gas accommodation coefficient, β_i , and the Henry constant, H (the values are shown near the curves). The thick curves marked 'equilibrium' correspond to quasi-equilibrium phase transition of the inert component.

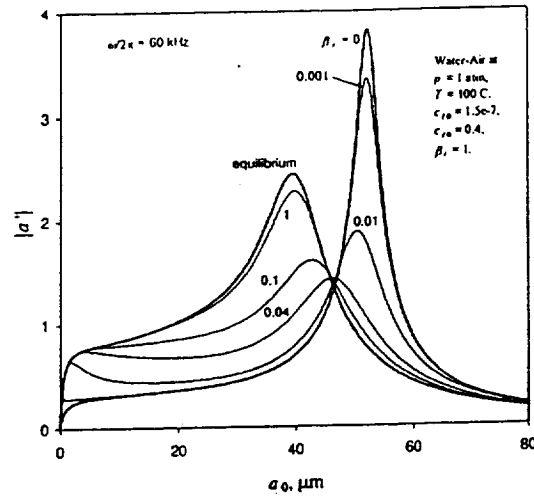


Figure VII-13: Relative amplitude of the forced vapor-gas bubble radial oscillation in 60 kHz acoustic field as a function of the bubble radius. The numbers near the curves show the value of the vapor accommodation coefficient, β_v . The curves marked 'equilibrium' correspond to quasi-equilibrium phase transition of the vapor.

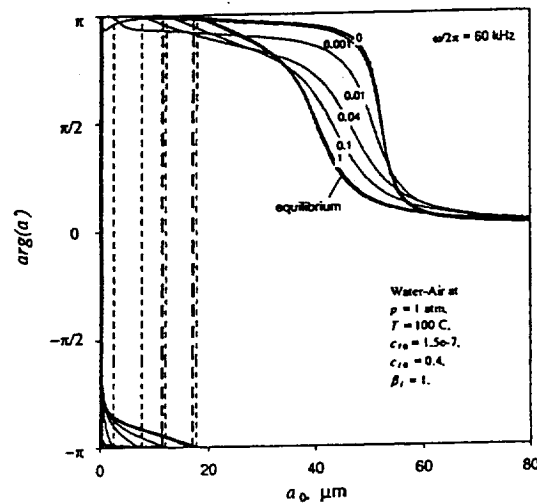


Figure VII-14: Phase shift between the driving pressure and the forced vapor-gas bubble radial oscillation in 60 kHz acoustic field as a function of the bubble radius. The numbers near the curves show the value of the vapor accommodation coefficient, β_v . The curves marked 'equilibrium' correspond to quasi-equilibrium phase transition of the vapor.

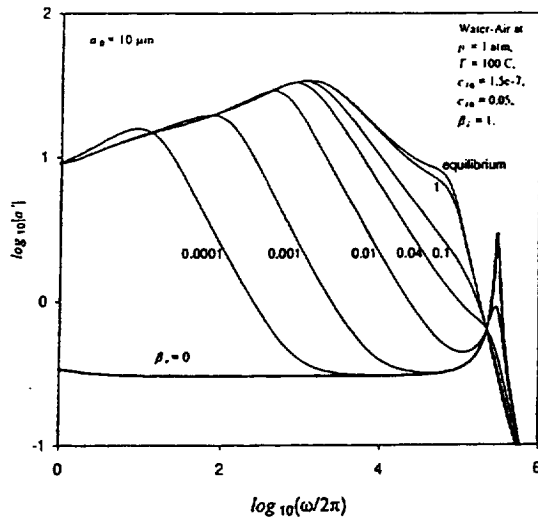


Figure VII-15: Relative amplitude of the forced vapor-gas bubble radial oscillation for 10 μm bubble in water as a function of the bubble radius. The numbers near the curves show the value of the vapor accommodation coefficient, β_v . The curves marked 'equilibrium' correspond to quasi-equilibrium phase transition of the vapor.

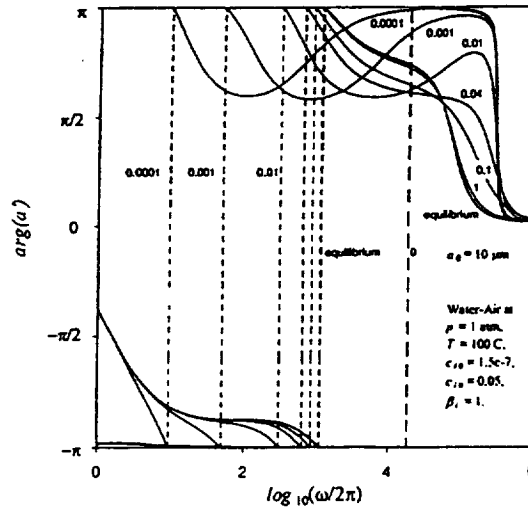


Figure VII-16: Phase shift between the driving pressure and the forced vapor-gas bubble radial oscillation for 10 μm bubble in water as functions of the bubble radius. The numbers near the curves show the value of the vapor accommodation coefficient, β_v . The curves marked 'equilibrium' correspond to quasi-equilibrium phase transition of the vapor.

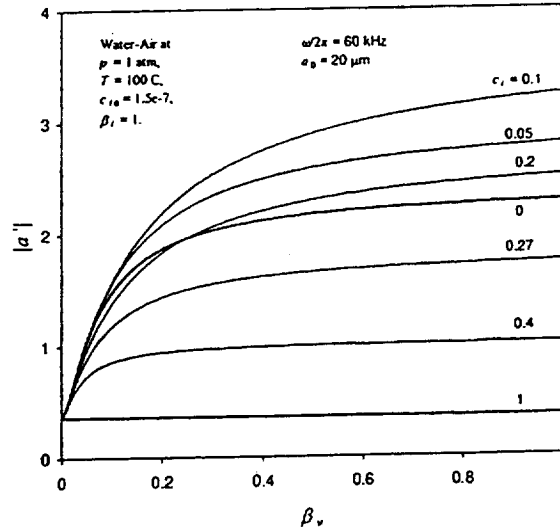


Figure VII-17: Relative amplitude of the forced vapor-gas bubble radial oscillation for $20 \mu\text{m}$ bubble in 60 kHz acoustic field as a function of the vapor accommodation coefficient. The numbers near the curves show the value of the inert gas concentration.

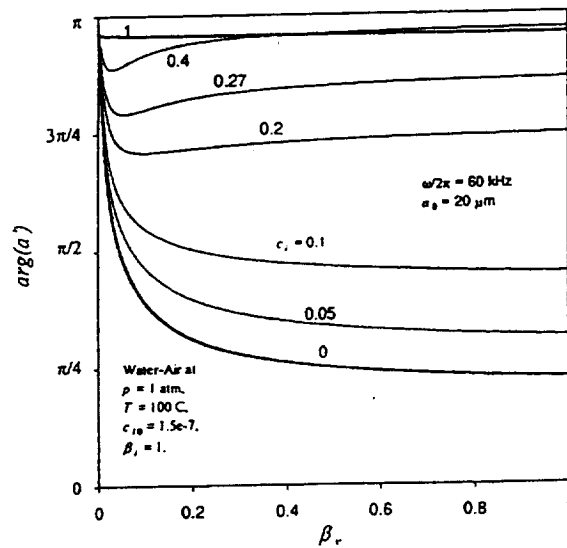


Figure VII-18: Phase shift between the driving pressure and the forced vapor-gas bubble radial oscillation for $20 \mu\text{m}$ bubble in 60 kHz acoustic field as functions of the vapor accommodation coefficient. The numbers near the curves show the value of the inert gas concentration.

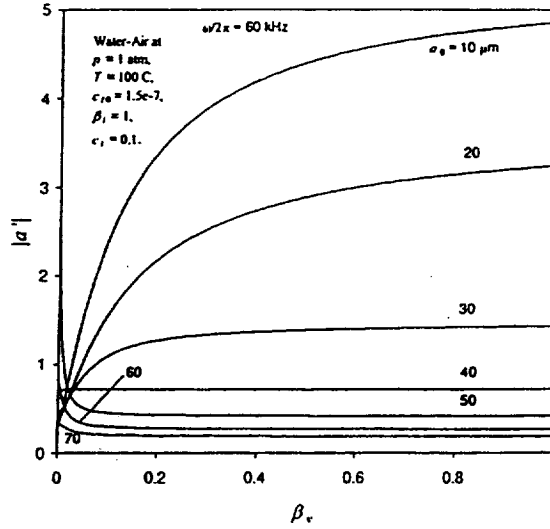


Figure VII-19: Relative amplitude of the forced vapor-gas bubble radial oscillation in 60 kHz acoustic field as functions of the vapor accommodation coefficient. The numbers near the curves show the mean bubble radius.

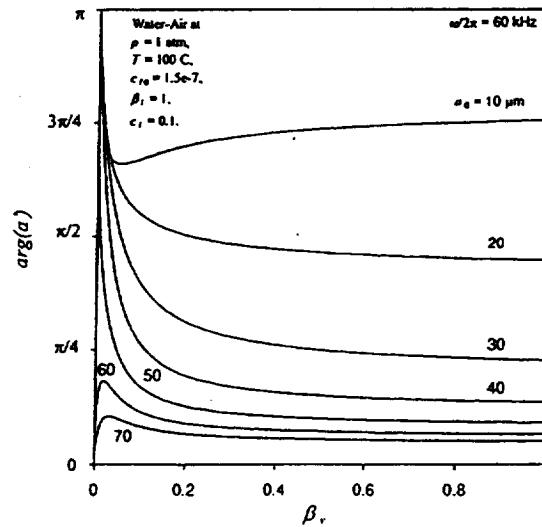


Figure VII-20: Phase shift between the driving pressure and the forced vapor-gas bubble radial oscillation in 60 kHz acoustic field as functions of the vapor accommodation coefficient. The numbers near the curves show the mean bubble radius.

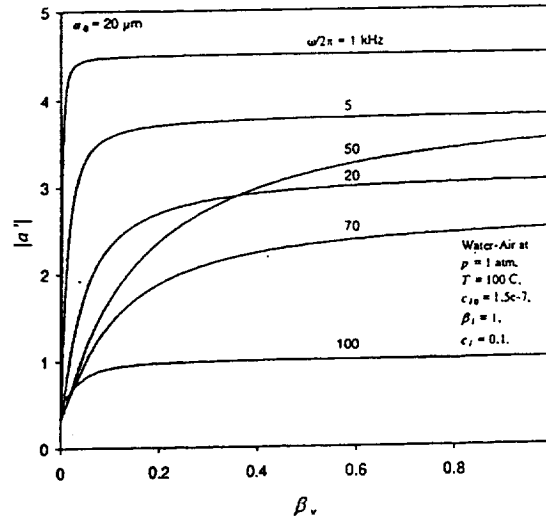


Figure VII-21: Relative amplitude of the forced vapor-gas bubble radial oscillation for $20 \mu\text{m}$ bubble as a function of the vapor accommodation coefficient. The numbers near the curves show the frequency of the acoustic field.

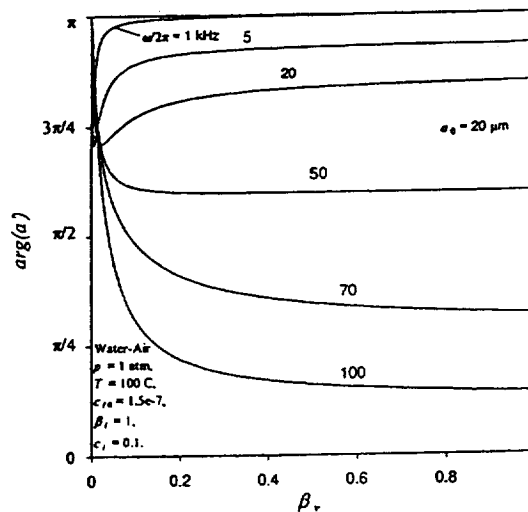


Figure VII-22: Phase shift between the driving pressure and the forced vapor-gas bubble radial oscillation for $20 \mu\text{m}$ bubble as a function of the vapor accommodation coefficient. The numbers near the curves show the frequency of the acoustic field.

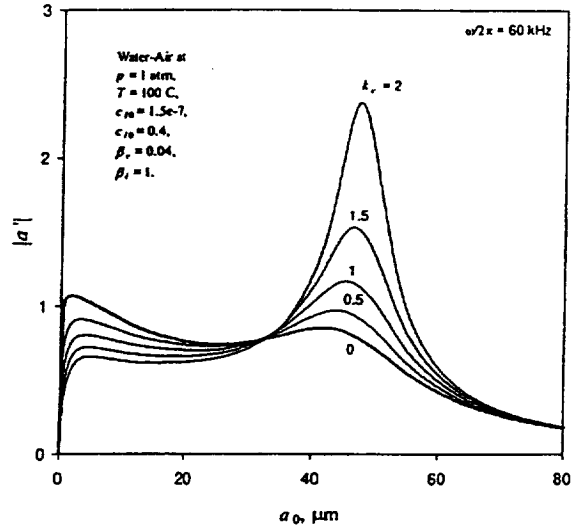


Figure VII-23: Relative amplitude of the forced vapor-gas bubble radial oscillation in 60 kHz acoustic field as a function of the bubble radius. The numbers near the curves show the value of the thermodiffusion coefficient k_c .

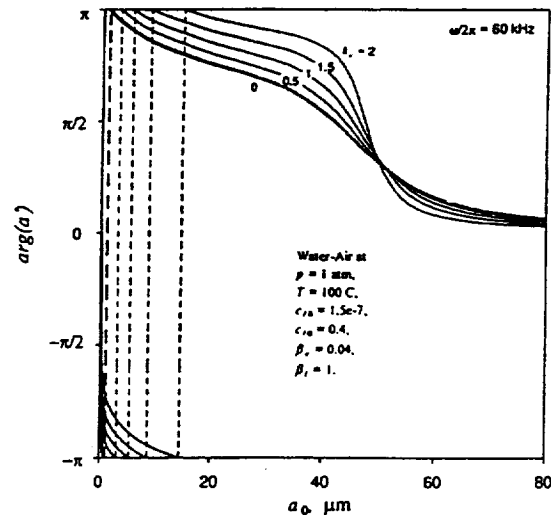


Figure VII-24: Phase shift between the driving pressure and the forced vapor-gas bubble radial oscillation in 60 kHz acoustic field as a function of the bubble radius. The numbers near the curves show the value of the thermodiffusion coefficient k_c .

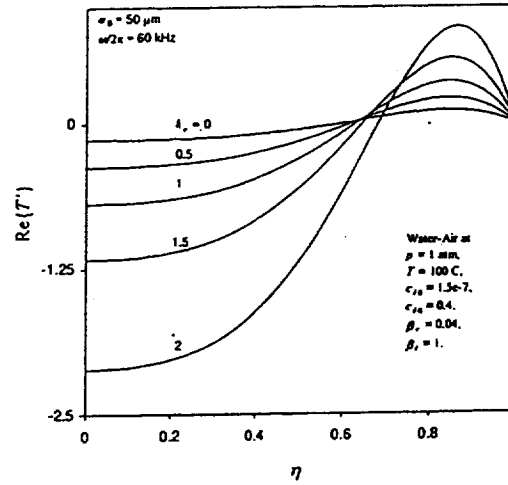


Figure VII-25: Dimensionless perturbations of temperature profiles inside $50\ \mu\text{m}$ vapor-gas bubble oscillating in 60 kHz acoustic field. Profiles correspond to times $\omega t = 2\pi n$. The numbers near the curves show the value of the thermodiffusion coefficient k_c .

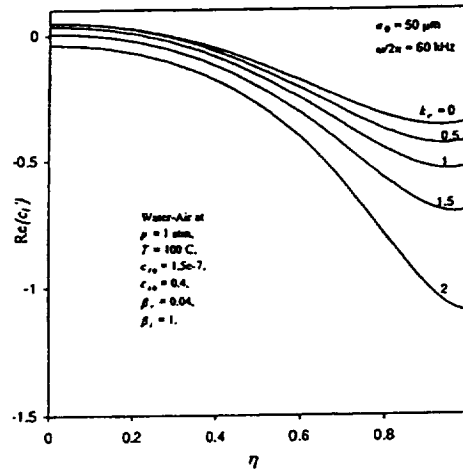


Figure VII-26: Dimensionless perturbations of inert gas concentration profiles inside $50\ \mu\text{m}$ vapor-gas bubble oscillating in 60 kHz acoustic field. Profiles correspond to times $\omega t = 2\pi n$. The numbers near the curves show the value of the thermodiffusion coefficient k_c .

Chapter VIII.

Analysis of Nonlinear Bubble Dynamics in Isotropic Acoustic Fields

1. The Equilibrium Radius and Its Stability

There exists a possibility of stabilization of the vapor bubble radius in an acoustic field. Complete stability analysis cannot be performed based on asymptotic theory, since the residual terms, such as in equation (IV-63) can cause a growth or decay of bubble radius in slower time scales than that taken into account (secular terms). However, if the steady radius exists, then it is stable in any slow time scale. If it does not exist then there is no stable radius in low order approximations. That is why low order approximations can provide valuable information on the bubble stability. Everywhere below when we speak about stability we mean stability within the framework of the third-order theory, which can potentially be violated in slower time scales.

Let us define the steady radius, a_* , as a zero of function W_2 :

$$W_2(a_*) = 0. \quad (\text{VIII-1})$$

Consider a small perturbation of a_0 near this radius:

$$\alpha = a_0 - a_*. \quad (\text{VIII-2})$$

Linearizing (IV-63) near $a_0 = a_*$ we find:

$$\begin{aligned} \frac{\partial \alpha}{\partial \tau} &= W'_* \alpha - \frac{\epsilon L_\beta V_*}{\sqrt{\pi}} \left[\frac{\Phi_{200}}{\sqrt{\tau}} + \Phi'_{20*} \int_0^\tau \frac{\partial \alpha(\zeta)}{\partial \zeta} \frac{d\zeta}{\sqrt{\tau - \zeta}} \right] \\ W'_* &= \left. \frac{dW_2(a_0)}{da_0} \right|_{a_0=a_*}, \quad \Phi'_{20*} = \left. \frac{d\Phi_{20}(a_0)}{da_0} \right|_{a_0=a_*}, \quad V_* = V(a_*). \end{aligned}$$

Solution of this equation can be obtained using the forward and inverse Laplace transforms and can be represented in the form:

$$\alpha(\tau) = b_1 e^{z_1^2 \tau} \operatorname{erfc}(-z_1 \sqrt{\tau}) + b_2 e^{z_2^2 \tau} \operatorname{erfc}(-z_2 \sqrt{\tau}), \quad (\text{VIII-3})$$

where b_1 and b_2 are constants depending on initial conditions, while $z_{1,2}$ are the roots of the characteristic equation:

$$z_{1,2} = -\frac{1}{2}\epsilon L_\beta V_* \Phi'_{20*} \pm \sqrt{\frac{1}{4}\epsilon^2 L_\beta^2 V_*^2 \Phi'^2_{20*} + W'_*}. \quad (\text{VIII-4})$$

If $W'_* > 0$, then both roots z_1 and z_2 are real and have opposite signs. Since the function $e^{z^2} \text{erfc}(-z)$ exponentially grows for real positive $z \rightarrow \infty$, the steady radius a_* is unstable. This conclusion is consistent with the result of the second-order theory (if we set $\epsilon = 0$ in (VIII-3)). If $W'_* < 0$ the second-order theory shows that a_* is stable. In the third-order theory the stability criterion is $W'_* < -\frac{1}{2}\epsilon^2 L_\beta^2 V_*^2 \Phi'^2_{20*}$. This provides $|\arg z_{1,2}| > \frac{\pi}{4}$, necessary for exponential decay of $\alpha(\tau)$. In the case $-\frac{1}{2}\epsilon^2 L_\beta^2 V_*^2 \Phi'^2_{20*} < W'_* < 0$, one can check using the criterion $|\arg z_{1,2}| > \frac{\pi}{4}$ that a_* is stable at $\Phi'_{20*} > 0$, and a_* is unstable at $\Phi'_{20*} < 0$.

The third-order approximation provides the following asymptotic expansion near the stable radius at large times:

$$a_0(\tau) = a_* + \frac{\epsilon L_\beta V_* \Phi_{20*}}{W'_* \sqrt{\tau}} + \left(\frac{V'_*}{V_*} - \frac{1}{2} \frac{W''_*}{W'_*} \right) \left(\frac{\epsilon L_\beta V_* \Phi_{20*}}{W'_*} \right)^2 \frac{1}{\tau} + O(\tau^{-3/2}). \quad (\text{VIII-5})$$

2. Results of Computations

Even for a fixed substance and ambient conditions, such as for water at 1 atm ambient pressure and 100°C, classification of the vapor bubble behavior in acoustic fields is difficult, since three parameters of the pressure field ω , P_A , and Δp , the initial radius of the bubble introduced into the field, a_{in} , and the unknown β form a 5-dimensional parameter space. First we consider $\Delta p = 0$. It is known from previous studies and computations [67, 38] that in this case there exist two equilibrium average radii of the vapor bubble, a_* .

The lower equilibrium radius is unstable and is known as the threshold radius, a_{th} , since bubbles with initial size $a_{in} < a_{th}$ collapse, while bubbles with $a_{in} > a_{th}$ grow in the acoustic field. The upper equilibrium radius, a_{st} , is stable if the stability criterion obtained in the previous section holds, and for bubbles with $a_{in} > a_{th}$ their radii tend to a_{st} at large times. This is seen from the phase portrait of Equation (IV-49) plotted in Figure VIII-1. The growth rate, $da_0/dt = \epsilon^2 \partial a_0 / \partial \tau$, is zero at $a_0 = a_*$. In the illustrated case the maximum growth rate is realized at small and high (of order 1) values of β .

In the case of small β the growth rate has a sharp peak due to the phase shift and a high amplitude of the resonance bubble oscillations (see Figures VII-1 and VII-2) producing non-linear effects. However, for $\beta = 0$ the rate of evaporation/condensation is zero and the growth rate is zero. That is why the growth rate at very small values of the accommodation coefficient, such as $\beta = 0.0001$ in Figure VIII-1 is smaller than for $\beta = 0.001$. Such a non-monotonic dependence of the growth rate on the value of the accommodation coefficient was noticed earlier [2]. The case of high β demonstrates that the threshold and stable radius can be substantially smaller than the primary resonance radius, since they are determined by the second resonance (see Figure VII-1). For an acoustic frequency of 60 kHz and β from 0.01 to 0.1 the maximum of the growth rate is located between the two resonance bubble sizes.

It is interesting that nonequilibrium phase transitions may influence the rectified heat transfer at surprisingly low frequencies (kilohertz range, see Fig. VIII-2). The effect is sufficiently strong near the bubble resonant sizes. However, it should be studied more carefully near the second bubble resonance because the present weakly nonlinear theory does not cover that range and only the neighborhood of the primary resonance is plotted in the figure.

Figure VIII-3 shows the relation between a_* and the sound amplitude at the bubble location for various β . For each β there exists a minimum of the plotted dependence which determines the amplitude threshold of vapor cavitation $P_A^{(\min)}$. For low intensity sound with $P_A < P_A^{(\min)}$ any bubble will collapse due to the effect of surface tension. For $P_A > P_A^{(\min)}$ two equilibrium radii: unstable, a_{th} (plotted by thin lines) and stable, a_{st} (plotted by thick lines), can be found from Figure VIII-3. Here and everywhere below stability of the equilibrium radius was determined using the stability criterion in the third order approximation. However we should notice that in the computed cases this criterion gives practically the same results as the stability criterion in the second order approximation, and the transition from stable to unstable radius occurs in very close vicinity of the extrema of the curves.

Figure VIII-4 shows the same dependence, but for three different frequencies. Note that although the present theory can be applied to high frequency ultrasonic fields it is limited by relatively small amplitudes (weakly non-linear approximation, $\epsilon \ll 1$). For water at atmospheric pressure and $\Delta p = 0$ the theory is limited to frequencies of order 100 kHz and less. For other substances such as cryogenic liquids the weakly non-linear approximation is valid for much higher frequencies. Figure VIII-5 shows that for liquid helium near the boiling point at atmospheric pressure, frequencies of 10 MHz and higher can be described by the present theory. Computations for liquid helium using the equilibrium scheme of phase transitions and the non-equilibrium scheme with $\beta = 1$ recommended at temperatures above the lambda-point [17] did not show a noticeable difference for frequencies up to 10 MHz.

The curve for the equilibrium radius at 1 kHz plotted in Figure VIII-4 shows that the stable radius of vapor bubble for $P_A \sim 0.1$ atm is of order 10 cm and larger for higher P_A . This explains why in the numerical simulations of Hao and Prosperetti [35] performed for frequencies of about 1 kHz, the stable radius was not achieved. The computations were carried out for millimeter bubbles which are much smaller than the stable size and should grow (even at very slow growth rates). As it is clear from Figure VIII-4 for higher frequencies stable oscillations can be reached for millimeter bubble sizes for 10 kHz fields and submillimeter bubbles for higher frequencies.

Positive values of Δp correspond to subcooled liquids. As seen in Figure VIII-5 for higher Δp higher intensity acoustic fields are required for acoustic vapor cavitation. For high β additional roots of the function $W_2(a_0)$ can appear, which corresponds to two unstable and two stable radii related to the primary and to the second resonances [38]. This is illustrated in Figure VIII-6 where the plotted horizontal line intersects the curve for $\beta = 1$ four times. In the illustrated case for β smaller than 0.1 only one stable radius corresponding to the primary resonance is realized.

Negative values of Δp correspond to superheated liquids. In such liquids bubbles with radii $a_{in} > a_e$, where a_e is determined by (III-36) grow in the absence of an acoustic field. As shown in Figure VIII-7 acoustic fields of relatively low frequency shift the threshold of bubble growth toward lower sizes. In the illustrated case of 10 kHz for water at atmospheric pressure and $\Delta p = -0.01$ atm ($a_e = 116 \mu m$) there is no equilibrium radius, and bubbles grow indefinitely if they exceed

the vapor cavitation threshold. It is interesting that for higher frequencies at the same conditions there can appear three equilibrium radii (one stable radius and two thresholds) in the range $a < a_e$. In the case of 60 kHz driving frequency illustrated in Figure VIII-8, curves computed at various values of β show local minima and maxima at $a < a_e$.

Figure VIII-8 shows that there exists a qualitative difference between the bubble dynamics at low, moderate, and high β . For example for an acoustic amplitude $P_A = 0.15$ atm indicated by the dashed line at $\beta = 0.04$ bubbles with radii $a_{in} > 29 \mu\text{m}$ will unlimitedly grow, while for $\beta = 0.1$ bubbles with initial radii $27 \mu\text{m} < a_{in} < 82 \mu\text{m}$ will stabilize near $a_{st} = 51 \mu\text{m}$ and only bubbles with $a_{in} > 82 \mu\text{m}$ will grow unlimitedly. The same situation takes place for $\beta = 0.01$, but with threshold radii, $a_{th}^{(1)} = 32 \mu\text{m}$ and $a_{th}^{(2)} = 98 \mu\text{m}$, and the stable radius $a_{st} = 89 \mu\text{m}$. Such influence of the accommodation coefficient on the threshold and stable radii of vapor bubbles in acoustic fields can be exploited for measurement of β .

This is supported by Figures (VIII-9) - (VIII-10) which demonstrate the bubble dynamics at different values of the accommodation coefficient with other conditions constant. Computations of these curves were performed using the second order approximation for the mean bubble radius and the first order approximation for the amplitude of oscillation. Substantially different signatures of the bubble dynamics created by different amplitudes of oscillation, growth and collapse rates, thresholds, and stable average radii can be used for evaluation of β .

Figures VIII-11-VIII-16 demonstrate the influence of initial conditions on the vapor bubble dynamics in acoustic fields. In all cases computations were performed using the third order approximation for the mean radius and the first order approximation for the oscillatory part. The second order approximation (IV-49) provided the same results as the third order approximation (IV-63) where $\Phi_{200} = 0$ was assumed. Condition $\Phi_{200} = 0$ as well as the second order approximation corresponds to the quasi-steady initial temperature profiles in the liquid. If the bubble is placed into the liquid of uniform temperature several initial bubble pulsations cause increase or decrease of the averaged bubble wall temperature which is treated by the present theory as a jump at $t_2 = 0$. Condition $\Phi_{200} \neq 0$ describes this jump and can substantially influence rectified heat transfer. Due to the initial jump of the non-oscillatory component of temperature the mean bubble size starts to grow or decay proportional to \sqrt{t} . This is determined by the sign of the function $\Phi_{20}(a_0)$ which can be negative or positive depending on a_0, β, ω , and other parameters (see Figure VIII-11).

Fig. VIII-12 shows the influence of nonequilibrium phase transitions on the vapor bubble dynamics in a 5 kHz acoustic field. All computations were made using the numerical-analytical method with the same (50 μm) initial bubble radius with the only difference in β . Computed average bubble radius was superposed with high-frequency oscillations obtained from the linear theory. It is seen that the bubble growth rates and amplitudes of oscillation strongly depend on β . The maximum rates are observed near the bubble resonant radii which also are functions of β .

Computations presented in Figure VIII-13 and VIII-14 show non-monotonic curves for the mean bubble radius for the case $\Phi_{200} = \Phi_{20}(a_{in})$ while for the case $\Phi_{200} = 0$ which coincides with the second-order approximation computations with the same initial radius, a monotonic increase or decrease of the mean bubble size was obtained. It is also noteworthy that the time required to achieve the stable bubble size ($a_{st} = 71 \mu\text{m}$) in the illustrated case substantially differs for the two different initial temperature profiles in the liquid. However, the time required to reach the

state independent of initial bubble size is approximately the same for different initial temperature profiles (of order $\omega t/2\pi \sim 10^3 - 10^4$). We found that after reaching this state efficient computations for $\Phi_{200} \neq 0$ can be performed using large-time asymptotic expression (VIII-5). Figures VIII-13 and VIII-14 demonstrates that the stable bubble size can be achieved for very large times (10^7 cycles, or about 3 minutes). However, we cannot prove this result mathematically strictly within the present theory (due to unknown structure of the residual terms. We show it because of a good agreement with straightforward computations at large times. Note that Hao & Prosperetti [35] reported that the bubble radius did not show stabilization at $\omega t/2\pi \sim 10^4$.

This is an interesting effect since estimations of the characteristic time of establishment of the quasisteady temperature profile in the liquid are of the order $t_{stab} \sim a_0^2/\kappa_l \sim 0.1$ s, or 10^4 cycles. The explanation can be found if we repeat calculations with the initial quasisteady temperature profile (decaying as $1/r$ at infinity, which is also an assumption underlying the second-order theory with respect to ϵ). In this case the times of stabilization agree well with estimations of t_{stab} , after which the average temperature exponentially reaches the steady distribution. For a bubble starting to oscillate in a uniform temperature field the unsteady average heat flux due to the initial temperature jump at the bubble surface decays as $t^{-1/2}$ which is determined by far field solution for a point heat source. Asymptotes corresponding to the principal unsteady term (VIII-5) are plotted in Fig. VIII-14 and they agree well with numerical results at $t \gg t_{stab}$.

The temperature profiles in the liquid corresponding to the case plotted in Fig. VIII-14 ($\beta = 0.04$) are shown in Fig. VIII-15. The dimensionless thickness of the 'fast' temperature sublayer, in the computed case was of order $L_{T1}/a_0 \sim 10^{-2}$. It is interesting to note that the matching boundary condition, $\Psi = T_{20} + E_{20}$ (see (IV-67)), shows a nonmonotonic behavior – first it increases and then decreases. This is related to a non-monotonic behavior of the mean bubble radius (see Fig. VIII-14) and a competition of the first (quasisteady) and the second (memory-type) terms in the right hand side of equation (IV-69). Fig. VIII-15 shows that even at times of order 10^6 periods of oscillation there exist some difference between the steady and unsteady average temperature profiles.

The possibility for the existence of steady bubble oscillations near the low-frequency resonance was discussed in [40, 34] and suggested as an explanation of the observed small stable bubbles in liquid helium. The present theory does not predict stable bubbles at 4.2 K and atmospheric pressure for 52 kHz acoustic field in the range of $15 \mu m$. However computations showed that at the parameters of the experiment the unstable threshold radius, a_{th} , of order $15 \mu m$ can be realized. Although this radius is unstable, the times of the instability development can reach several seconds, or hundreds of thousands of periods of oscillation (see Figure VIII-16; the thick and thin lines correspond to $\Phi_{200} = \Phi_{20}(a_{in})$ and $\Phi_{200} = 0$, respectively) which is of the same order of magnitude as the times observed in the experiments. In the experimental photographs some patterns of bubbles in standing waves were seen. Pattern formation in the liquid with vapor bubbles is a result of strong acoustic field/bubble interaction leading to self-organization of the bubbles [68, 69, 70]. Such interaction as well as the bubble drift to the nodes or antinodes of the standing wave can also provide stabilization of bubbles of a certain size.

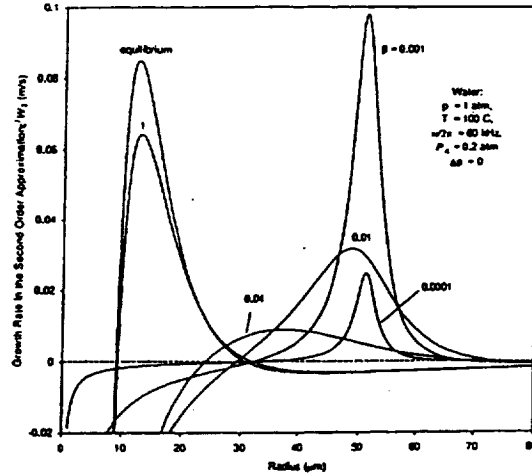


Figure VIII-1: Dependence of the growth rate of the vapor bubble on its radius for saturated water. The numbers near the curves show the values of the accommodation coefficient, β . The curve marked as “equilibrium” is computed using the quasiequilibrium scheme of phase transition.

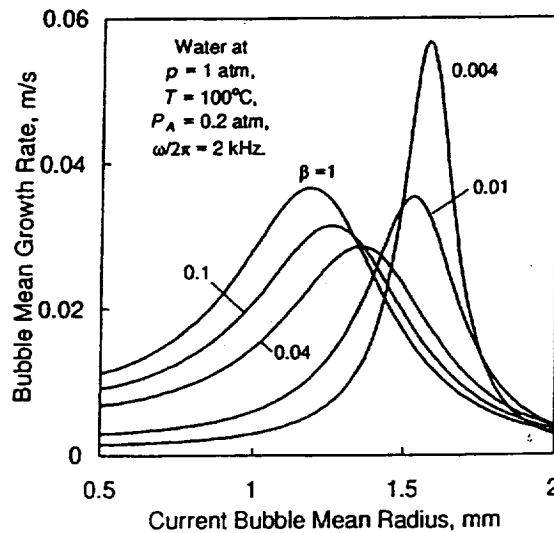


Figure VIII-2: The vapor bubble mean growth rate in an acoustic field as a function of the bubble current mean radius at various values of the accommodation coefficient (the second order theory).

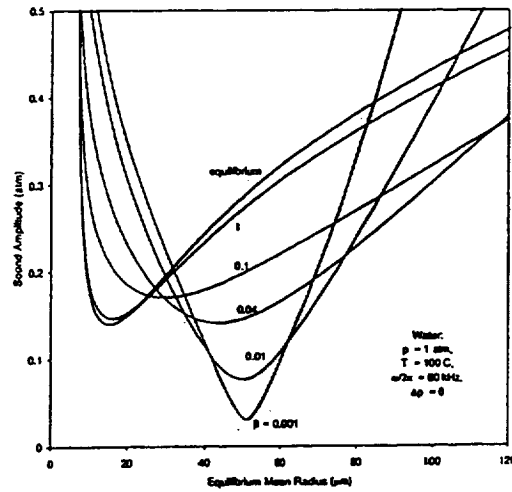


Figure VIII-3: Relation between the pressure amplitude and the equilibrium mean radius a_e for saturated water. The numbers near the curves show the values of the accommodation coefficient, β . The curve marked as "equilibrium" is computed using the quasi-equilibrium scheme of phase transition.

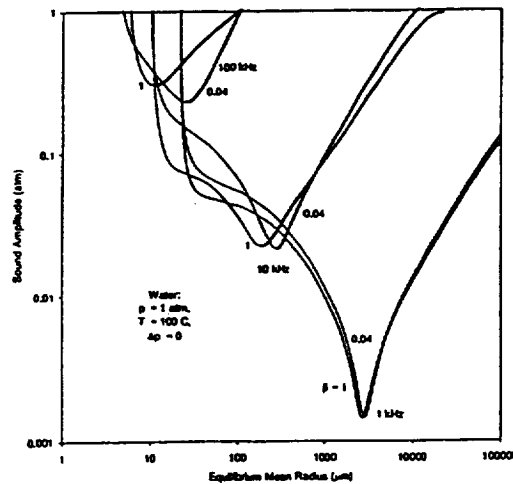


Figure VIII-4: Relation between the pressure amplitude and the equilibrium mean radius a_e for saturated water for 1 kHz, 10 kHz, and 100 kHz acoustic fields and for two values of the accommodation coefficient shown near the curves.

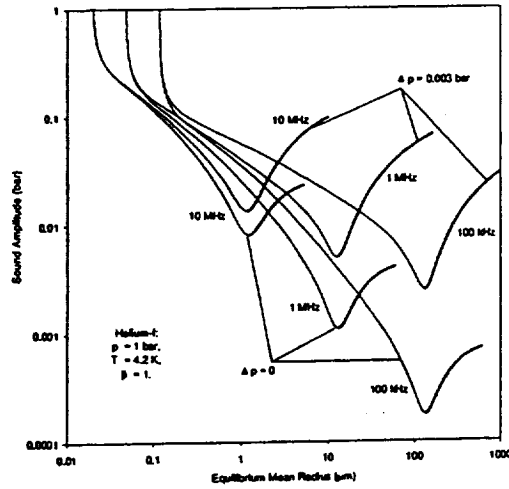


Figure VIII-5: Relation between the pressure amplitude and the steady radius a_* for saturated ($\Delta p = 0$) and subcooled ($\Delta p = 0.003$ bar) liquid helium for 100 kHz, 1 MHz, and 10 MHz acoustic fields.

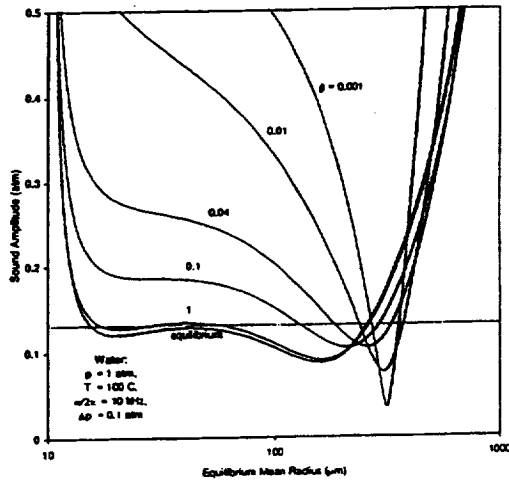


Figure VIII-6: Relation between the pressure amplitude and the equilibrium mean radius a_* for subcooled water. The numbers near the curves show the values of the accommodation coefficient, β . The curve marked as "equilibrium" is computed using the quasi-equilibrium scheme of phase transition. The thick lines correspond to the stable equilibrium mean radius while the thin lines show the unstable (threshold) equilibrium mean radius. The dotted line ($P_A = 0.12$ atm) intersects each plotted curve at 2 points, except the curve for $\beta = 1$, which is intersected at 4 points.

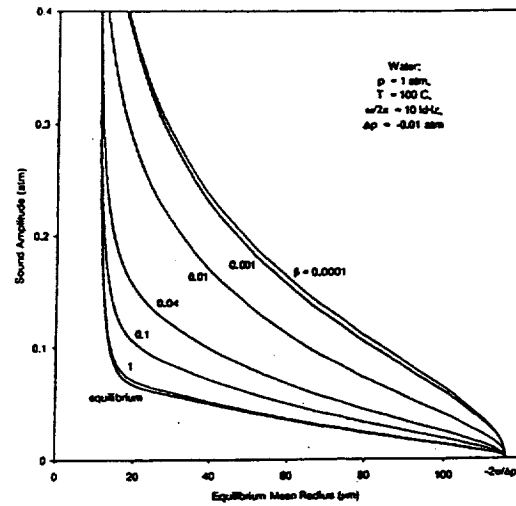


Figure VIII-7: Relation between the pressure amplitude and the equilibrium mean radius a_* for superheated water. The numbers near the curves show the values of the accommodation coefficient, β . The curve marked as "equilibrium" is computed using the quasi-equilibrium scheme of phase transition.

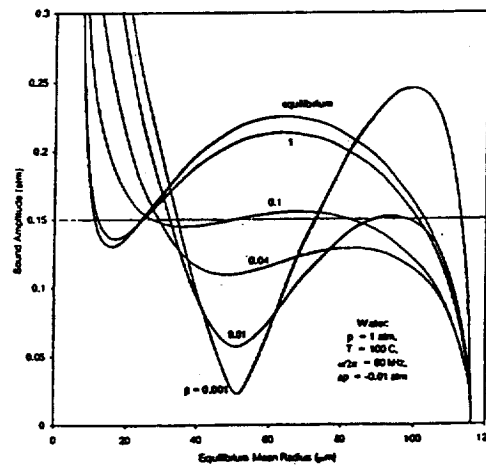


Figure VIII-8: Relation between the pressure amplitude and the equilibrium mean radius a_* for superheated water. The numbers near the curves show the values of the accommodation coefficient, β . The curve marked as "equilibrium" is computed using the quasi-equilibrium scheme of phase transition. The thick lines correspond to the stable equilibrium mean radius while the thin lines show the unstable (threshold) equilibrium mean radius. The dotted line ($P_A = 0.15$ atm) intersects each plotted curve at 3 points, except of the curve for $\beta = 0.04$, which is intersected at 1 point.

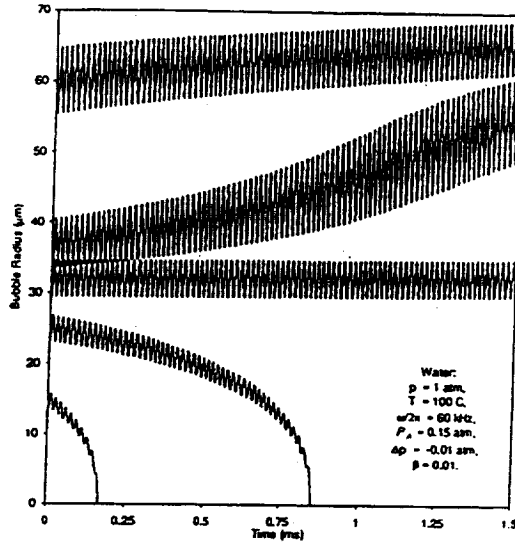


Figure VIII-9: Dynamics of bubbles of various initial radii in superheated water at $\beta = 0.01$. The second order theory.

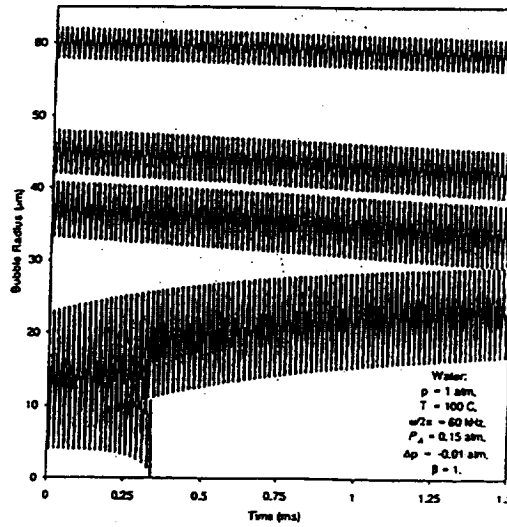


Figure VIII-10: Dynamics of bubbles of various initial radii in superheated water at $\beta = 1$. The second order theory.

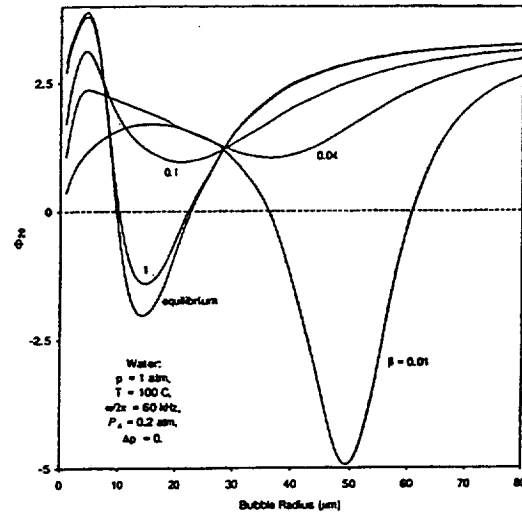


Figure VIII-11: Function $\Phi_{20}(a_0)$ describing initial conditions for the rate of the mean bubble radius growth in the third order approximation at various values of the accommodation coefficient indicated near the curves.

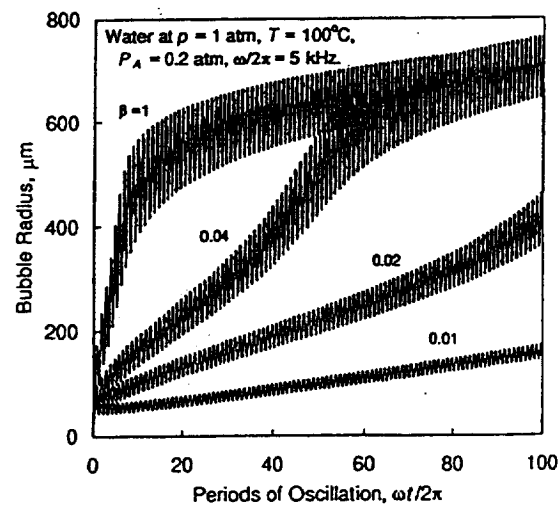


Figure VIII-12: The vapor bubble dynamics in an acoustic field at various values of the accommodation coefficient (the third-order theory). The initial radius in all cases was $50 \mu\text{m}$.

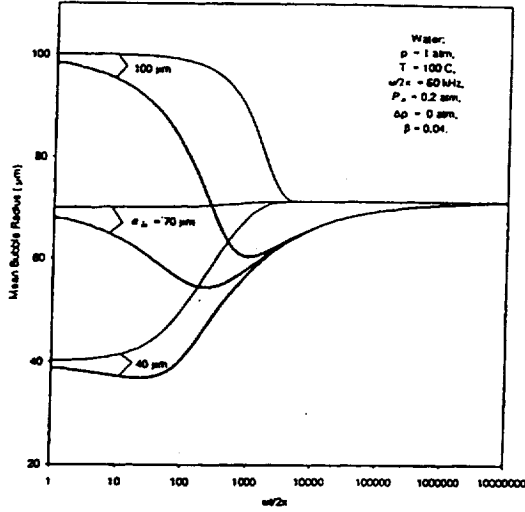


Figure VIII-13: Dynamics of the mean vapor bubble radius in water with different initial temperature profiles near the bubble, Φ_{200} , and different initial radii, a_{in} , shown near the curves. The thick lines correspond to the temperature jump at $t = 0$ ($\Phi_{200} = \Phi_{20}(a_{in})$) while the thin lines correspond to the initial quasi-steady temperature profiles near the bubble ($\Phi_{200} = 0$).

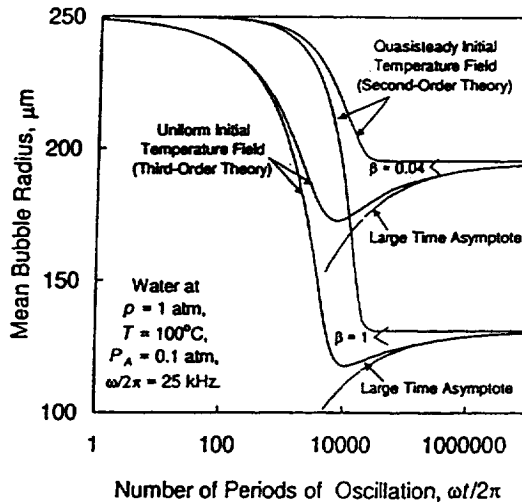


Figure VIII-14: The dynamics of the mean (period-averaged) vapor bubble radius in an acoustic field at various values of the accommodation coefficient and initial temperature profiles in the liquid. The third order theory for initial quasisteady temperature fields provide the same curves as the second order theory. The asymptotes show a two-term asymptotic expansion near the equilibrium mean radius.

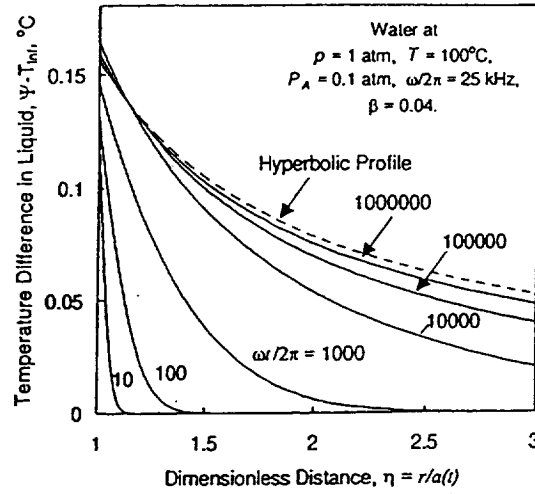


Figure VIII-15: Temperature profiles in the liquid during rectified heat transfer (third-order theory, numerical results). The numbers near the curves correspond to the number of cycles of bubble oscillation. The dashed curve shows a hyperbolic profile $(\Psi(a_0) - T_\infty)/\eta$ for $\Psi(a_0)$ at the millionth period of oscillation.

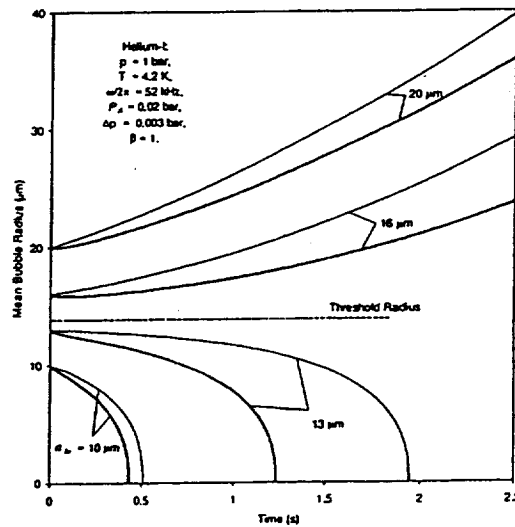


Figure VIII-16: Dynamics of the mean vapor bubble radius in liquid helium with different initial temperature profiles near the bubble, Φ_{200} , and different initial radii, a_{in} , shown near the curves. The thick lines correspond to the temperature jump at $t = 0$ ($\Phi_{200} = \Phi_{20}(a_{in})$) while the thin lines correspond to the initial quasi-steady temperature profiles near the bubble ($\Phi_{200} = 0$).

Chapter IX.

Analysis of Nonlinear Bubble Dynamics in Standing Acoustic Waves

A two-dimensional autonomous system (V-18) is convenient for qualitative analysis. In the present model for fixed temperature (say water at 100°C), the degree of subcooling/superheating, Δp , the frequency and amplitude of the acoustic field, ω and P_A , and the initial bubble radius and position, a_{00} and x_{00} , can be arbitrarily varied. The value of the accommodation coefficient, β , frequently is not well known for the system under consideration (since it is sensitive to trace impurities), and it can be considered as an unknown parameter. Finally, the value of g , can be varied over a wide range. These independent parameters form a 7-dimensional parametric space, which complicates a parametric analysis. The drag coefficient could also be varied. However, in the present analysis we kept it constant $K_\mu = 3$, which corresponds to the drag coefficient of a spherical bubble at high Reynolds numbers.

1. Zero Gravity Conditions

We start our analysis by consideration of the vapor bubble stability in zero-gravity conditions, when we can formally set $g_r = 0$. In this case the function $V_2(a_0, x_0)$ has zeros at nodes and antinodes of the acoustic pressure, $\sin x_0 \cos x_0 = 0$. These zeros correspond to stable and unstable equilibrium positions of the bubble in the standing acoustic wave. The bubble is attracted to the pressure antinodes, $x_0 = \frac{\pi}{2} + \pi n$ ($n = 0, 1, \dots$), when $v_{22}(a_0) > 0$, and to the pressure nodes $x_0 = \pi n$, when $v_{22}(a_0) < 0$. We will call the bubble 'A-stable' if it is attracted to the pressure *antinode* and 'N-stable' if it is attracted to the pressure *node*. We also define the bubble as 'V-stable' if its average *volume* (or a_0) is stable in an acoustic field. It is clear that for overall bubble stability both positional and volume stability should be achieved. Note that the N-stable bubble will grow or collapse since the local acoustic pressure is zero at the pressure node and the bubble is V-unstable in the absence of the acoustic field. This is consistent with Eq.(V-19) that gives $W_2(a_0, \pi n) = w_{20}(a_0)$, where $w_{20}(a_0)$ is a monotonic function. Therefore, only A-stable bubbles corresponding to $W_2(a_0, \frac{\pi}{2} + \pi n) = w_{20}(a_0) + w_{22}(a_0)$ can be V-stable and generally stable.

The function $v_{22}(a_0)$ does not depend on Δp and P_A . Thus, at fixed ambient conditions, and known drag coefficient, K_μ , the zeros of this function, a_{pos} , depend only on the acoustic

frequency and the accommodation coefficient, $a_{pos} = a_{pos}(\omega, \beta)$. The function $W_2(a_0, \frac{\pi}{2} + \pi n)$ depends on the same parameters as well as on Δp and P_A . For the zeros of this function we have $a_{vol} = a_{vol}(\omega, \beta, \Delta p, P_A)$. Consider the following three cases showing qualitatively different results about the roots a_{vol} .

a. Saturated Liquids

In this case the ambient pressure corresponds to the saturation line, and $\Delta p = 0$. Two roots of equation $W_2(a_0, \frac{\pi}{2} + \pi n) = 0$ appear only if the amplitude of the acoustic field exceeds the threshold of vapor cavitation $P_A > P_{A*}(\omega, \beta)$ (Figure IX-1). The value of $P_{A*}(\omega, \beta)$ can be found by excluding a_0 from the simultaneous conditions:

$$W_2(a_0, \frac{\pi}{2} + \pi n; P_A, \omega, \beta) = 0, \quad \frac{\partial P_A(a_0, \omega, \beta)}{\partial a_0} = 0. \quad (\text{IX-1})$$

Curves $a_0 = a_{vol}(\omega, \beta, 0, P_{A*}(\omega, \beta))$ determine a region where stable bubble volume oscillation can exist. Projection of this regions onto the (a, ω) plane for water for the value $\beta = 0.04$ is shown in Figure IX-2a. It is interesting to note that the regions of A-stability and V-stability in the computed cases do not intersect. In other words, for $\Delta p = 0$, water vapor bubbles at 100°C are unstable in any acoustic field. Unfortunately we cannot prove this observation for other substances or for water in other conditions because of the high dimension of the parametric space.

Figure IX-3 demonstrates phase trajectories of the dynamical system (V-18) computed at $P_A > P_{A*}(\omega, \beta)$. The phase portrait is periodic with the period equal to half the acoustic wavelength. The figure plots only one period. All trajectories end at $a_0 = 0$, despite the existence of regions of bubble growth. However, all growing bubbles finally move toward the pressure node, where the acoustic field cannot support the bubble growth and the bubble collapses. Note that only bubbles exceeding a critical size can grow near the pressure antinode.

There exists a possibility for bubble average radius oscillations (spiral trajectories). The mechanism of such oscillations is the following. A bubble growing near the pressure antinode is forced to move towards the pressure node. There, the local amplitude of acoustic pressure is lower and it collapses. At smaller sizes the direction of the acoustic radiation force changes and the bubble moves back toward the pressure antinode where it can grow again and repeat the cycle. However, our analysis shows that these oscillations are unstable and the bubble will always collapse. Note that such oscillations can occur in both superheated and subcooled liquids. An example of the oscillating average bubble size behavior is shown in Figure IX-6.

b. Superheated Liquids

This case corresponds to $\Delta p < 0$. Any bubble exceeding the critical size a_c , Eq.(III-36), will grow even in the absence of the acoustic field. In contrast to the previous case, now three roots of equation $W_2(a_0, \frac{\pi}{2} + \pi n) = 0$ can exist (see Figure IX-1b). This determines two branches of the curve $a_0 = a_{vol}(\omega, \beta, \Delta p, P_{A*}(\omega, \beta, \Delta p))$ bounding the region of V-stability. Threshold values for $P_{A*}(\omega, \beta, \Delta p)$ are determined by Eq.(IX-1). Projection of this region onto (a, ω) plane for water at $\Delta p = -0.01$ atm and $\beta = 0.04$ is shown in Figure IX-2b. As in the previous case the regions

of A-stability and V-stability for water vapor bubbles at 100°C do not intersect and, therefore, bubbles are unstable in superheated liquids in any acoustic field.

Figure IX-4 displays the phase trajectories of the dynamical system (V-18). All trajectories either end at $a_0 = 0$, or grow unlimitedly corresponding to bubble growth due to the liquid superheat. Figure IX-7 illustrates the dynamics of two bubbles with the same initial position in the wave, but slightly different initial sizes near the critical size a_e . Both of them move relatively quickly towards the pressure antinode (the x-coordinates of the centers in these cases practically coincide). At the antinode the smaller bubble collapses, while the larger bubble grows. This is determined by the bubble size with respect to a_e at the moment of reaching the pressure antinode of the standing wave.

c. Subcooled Liquids

In this case $\Delta p > 0$. The intriguing feature of this case is the possibility of existence of four roots of the equation $W_2(a_0, \frac{\pi}{2} + \pi n) = 0$ (Figure IX-1a). This determines three branches of curve $a_0 = a_{vol}(\omega, \beta, \Delta p, P_{A*}(\omega, \beta, \Delta p))$ bounding two regions of V-stability. Projections of these regions onto the (a, ω) plane for water at $\Delta p = 0.02$ atm and $\beta = 0.04$ and $\beta = 1$ are shown in Figure IX-2c. It is seen that an intersection of the regions of stability exists, which provides both A- and V-stability. Therefore, in subcooled liquids vapor bubbles can be stabilized by an acoustic field. However, we should notice that the amplitude of this field is constrained by two similar values of P_{A*} corresponding to the maximum and minimum of the function $P_A(a_0)$. For example, in the case shown in Figure IX-1a at $\Delta p = 0.02$ atm, the bubble can be stabilized in a narrow range of amplitudes $0.0885 \text{ atm} < P_A < 0.0892 \text{ atm}$. The range can be wider at different ambient conditions or for substances other than water.

The region of stability occurs at relatively low frequencies, when the primary resonance radius and the condensation-evaporation (or 'second'; Marston, 1979; Hao and Prosperetti, 1999) resonance radius are substantially separated. The stabilization occurs near the second resonance. Note that Marston and Greene (1978) observed stable bubble oscillations in subcooled liquid helium and explained them as an effect of the second resonance.

Figure IX-5 shows phase trajectories of the dynamical system (V-18) in the neighborhood of the stable state. All trajectories from the attraction region end at the point corresponding to the stable state. Note that this region is limited and is relatively wide for bubble size and relatively narrow for bubble position. Therefore, to obtain stable oscillations the bubble should be initially situated close to the pressure antinode of the acoustic wave. The process of stabilization of bubble size and position is shown in Figure IX-8 for two bubbles with initial sizes smaller and larger than the stable radius and the same initial position. An interesting feature is that the bubble of the larger initial size contracts below the stable radius and then expands. This is consistent with the phase trajectories of Figure IX-5.

2. Effects of Gravity

According to Eq.(V-18), gravity influences the bubble growth rate and the average translational velocity. However, the effect of gravity on bubble growth rate is rather small (if it is taken into

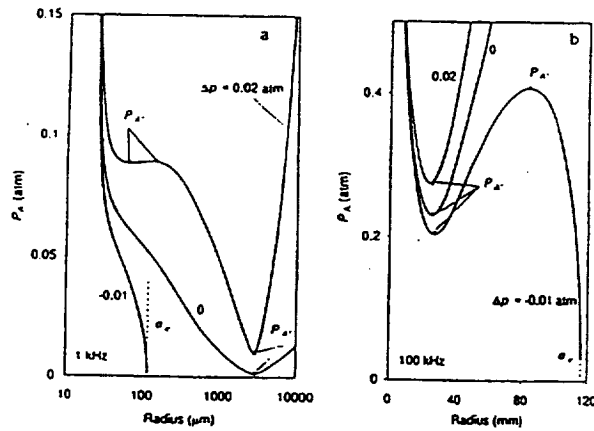


Figure IX-1: The amplitudes of 1 kHz and 100 kHz isotropic acoustic fields at which a bubble can experience steady (stable or unstable) oscillations for water at $\beta = 0.04$ and $T = 373$ K.

account just in the last term of Eq.(III-4)). The most important effect is destabilization of the bubble position.

As an example of destabilization, Figures IX-9-IX-10 show phase trajectories of system (V-18) at various levels of gravity. In zero gravity conditions the system has a stable state (Figure IX-5). If some level of gravity is imposed the equilibrium position shifts from the pressure antinode. The larger gravity is, the larger is this shift. This takes place until some threshold value of gravity corresponding to reaching the boundary of the attracting region. For gravity higher than this threshold, the steady state solution longer exist. Figure IX-11 demonstrates the bubble dynamics in subcooled liquids.

It is interesting that gravity can turn unstable oscillations of average bubble size and position into stable oscillations. In zero gravity the system has unstable equilibrium points (see Figure IX-2a). For increasing magnitude of gravity (Figures IX-12-IX-14), the two illustrated equilibrium points are not symmetric, and a limit cycle appears near the left equilibrium point. However, further increase of gravity up to one g destabilizes this limit cycle. Figure IX-15 demonstrates the bubble dynamics in saturated liquids. The stable oscillations of the average bubble radius and coordinate of the center can also be observed in subcooled and superheated liquids.

Figures IX-16-IX-17 present computations of the mean bubble radius and position for different values of the accommodation coefficient and different levels of gravity for all other parameters fixed. It is seen that the measurements of the accommodation coefficient can be performed at zero gravity, reduced gravity, and normal gravity conditions. However, for each level of gravity there exist specific patterns or regimes of bubble dynamics which should be taken into account in selection of optimal conditions for measurement of the accommodation coefficient.

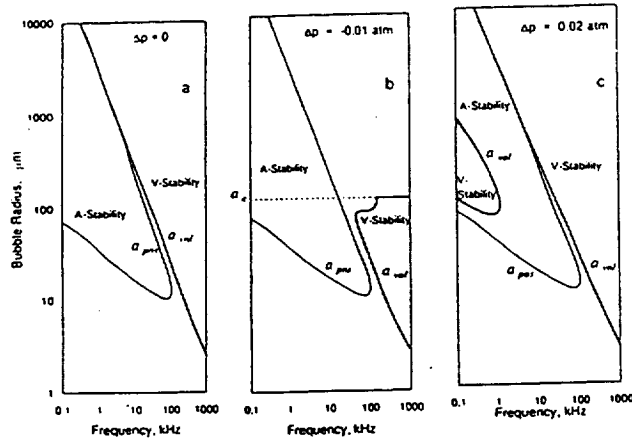


Figure IX-2: The regions of A- and V-stability of bubbles at zero gravity for saturated, superheated, and subcooled water at $\beta = 0.04$ and $T = 373$ K.

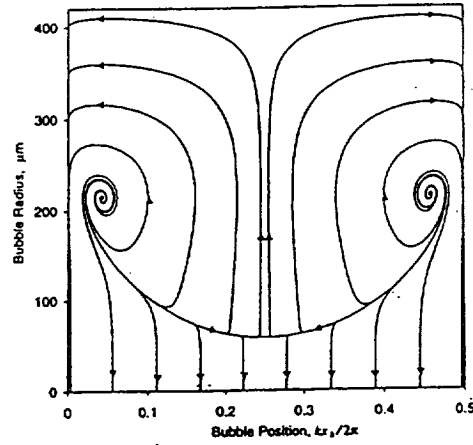


Figure IX-3: The phase trajectories for saturated water at 0g, $\beta = 0.04$ and $T = 373$ K. 10 kHz acoustic field, $\epsilon = 0.099$.

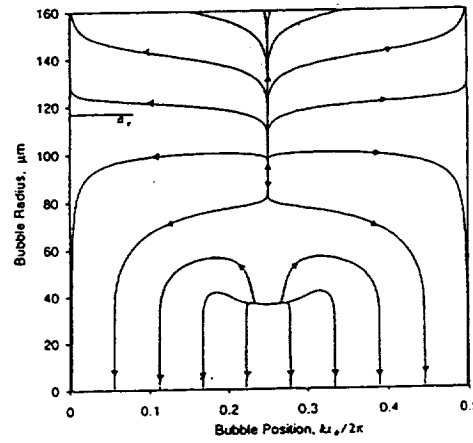


Figure IX-4: The phase trajectories for superheated water at 0g, $\Delta p = -0.01$ atm, $\beta = 0.04$ and $T = 373$ K. 60 kHz acoustic field, $\epsilon = 0.123$.

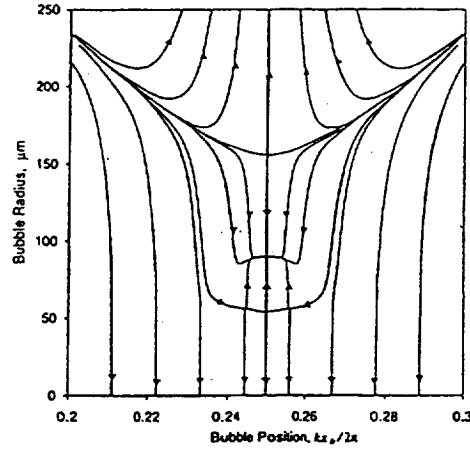


Figure IX-5: The phase trajectories for subcooled water at $0g$, $\Delta p = 0.02$ atm, $\beta = 0.04$ and $T = 373$ K. 1 kHz acoustic field, $\epsilon = 0.088$.

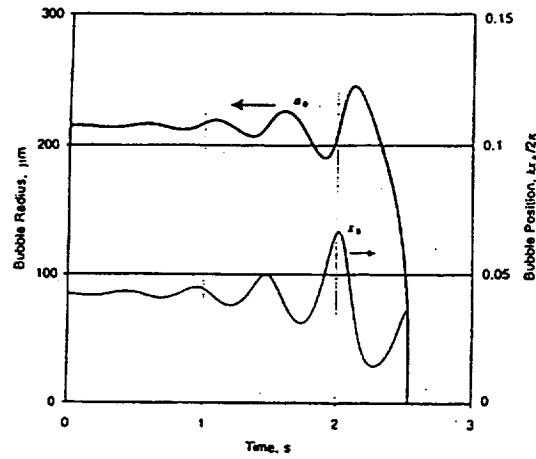


Figure IX-6: The bubble dynamics corresponding to a phase trajectory from Figure 3.

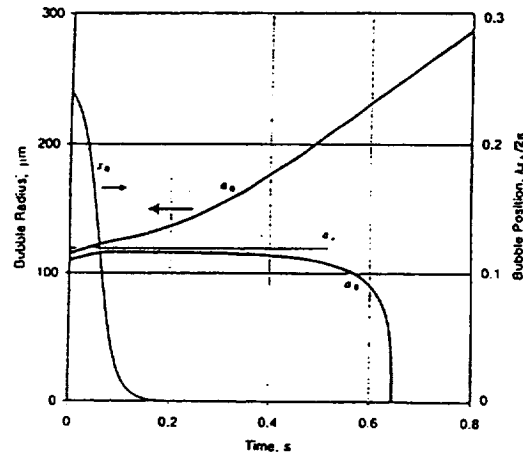


Figure IX-7: The bubble dynamics corresponding to phase trajectories from Figure 4.

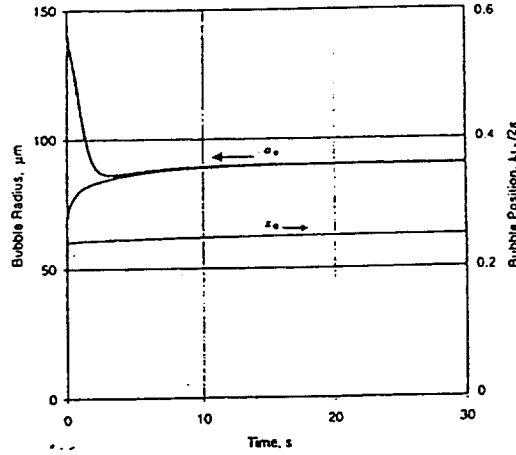


Figure IX-8: The bubble dynamics corresponding to phase trajectories from Figure 5.

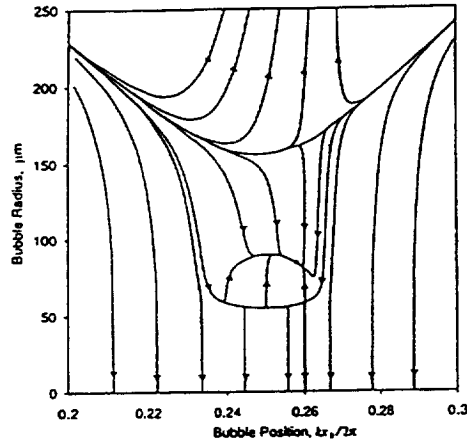


Figure IX-9: The phase trajectories for subcooled water at 0.05g, $\Delta p = 0.02$ atm, $\beta = 0.04$ and $T = 373$ K. 1 kHz acoustic field, $\epsilon = 0.088$.

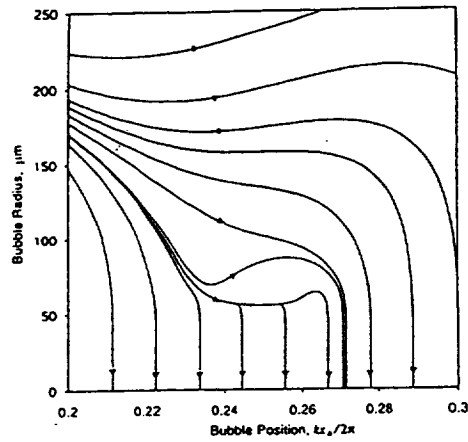


Figure IX-10: The phase trajectories for subcooled water at 1g, $\Delta p = 0.02$ atm, $\beta = 0.04$ and $T = 373$ K. 1 kHz acoustic field, $\epsilon = 0.088$.

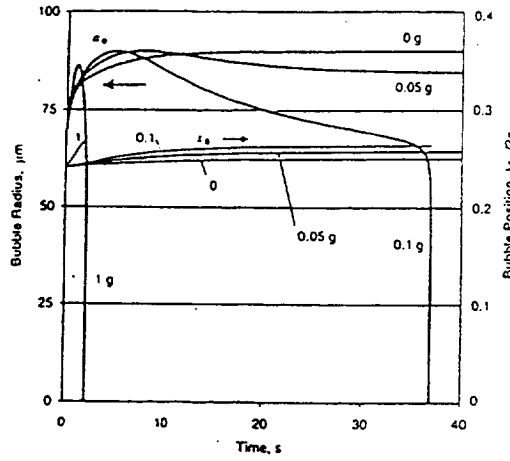


Figure IX-11: The bubble dynamics in subcooled water at various levels of gravity $\Delta p = 0.02$ atm, $\beta = 0.04$ and $T = 373$ K. 1 kHz acoustic field, $\epsilon = 0.088$.

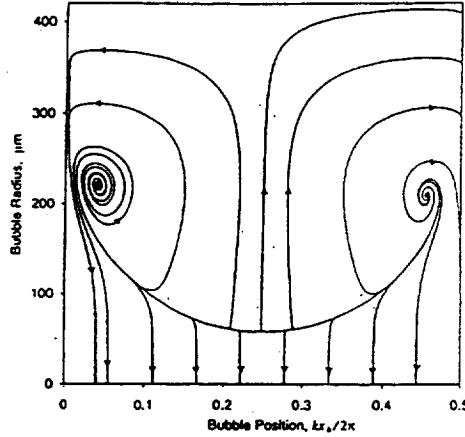


Figure IX-12: The phase trajectories for saturated water at 0.05g, $\beta = 0.04$ and $T = 373$ K. 10 kHz acoustic field, $\epsilon = 0.099$.

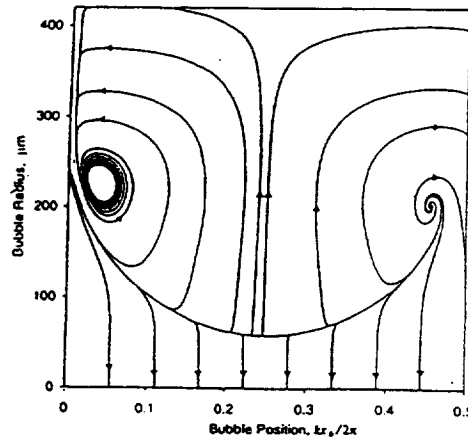


Figure IX-13: The phase trajectories for saturated water at 0.1g, $\beta = 0.04$ and $T = 373$ K. 10 kHz acoustic field, $\epsilon = 0.099$.

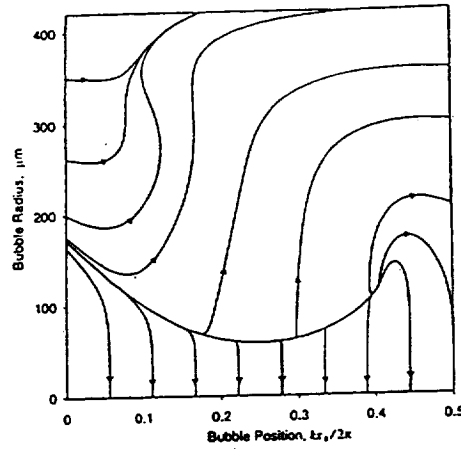


Figure IX-14: The phase trajectories for saturated water at $1g$, $\beta = 0.04$ and $T = 373$ K. 10 kHz acoustic field, $\epsilon = 0.099$.

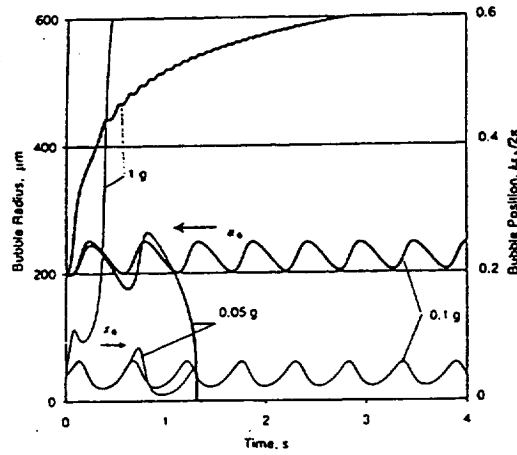


Figure IX-15: The bubble dynamics in saturated water at various levels of gravity, $\beta = 0.04$ and $T = 373$ K. 1 kHz acoustic field, $\epsilon = 0.088$.

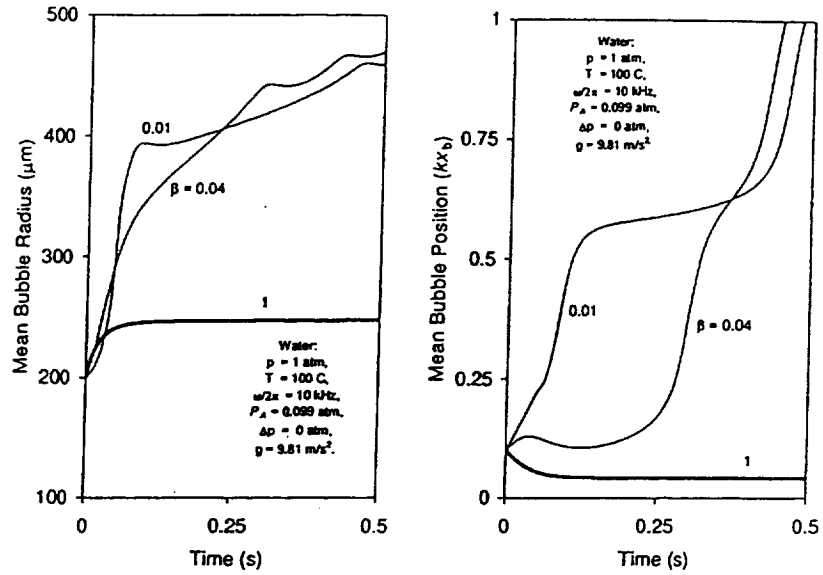


Figure IX-16: Dynamics of a vapor bubble in a standing acoustic wave at different values of the accommodation coefficient and normal gravity conditions.

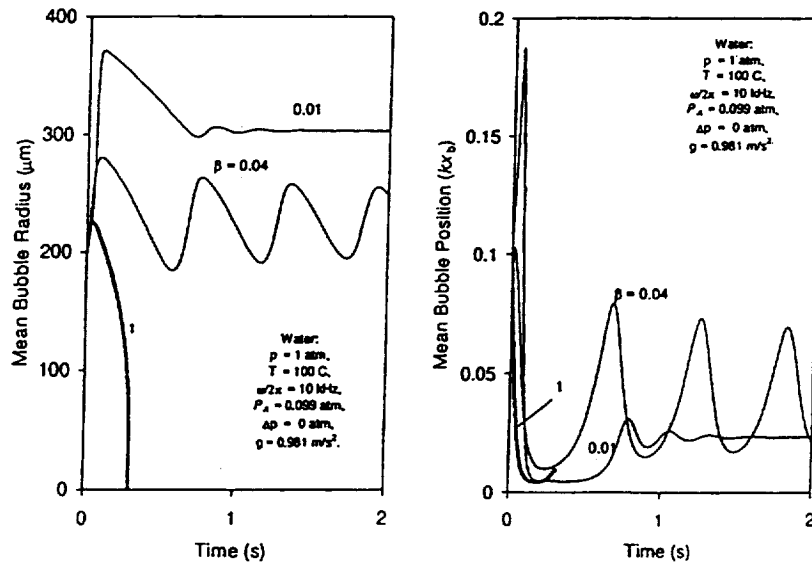


Figure IX-17: Dynamics of a vapor bubble in a standing acoustic wave at different values of the accommodation coefficient and reduced gravity conditions.

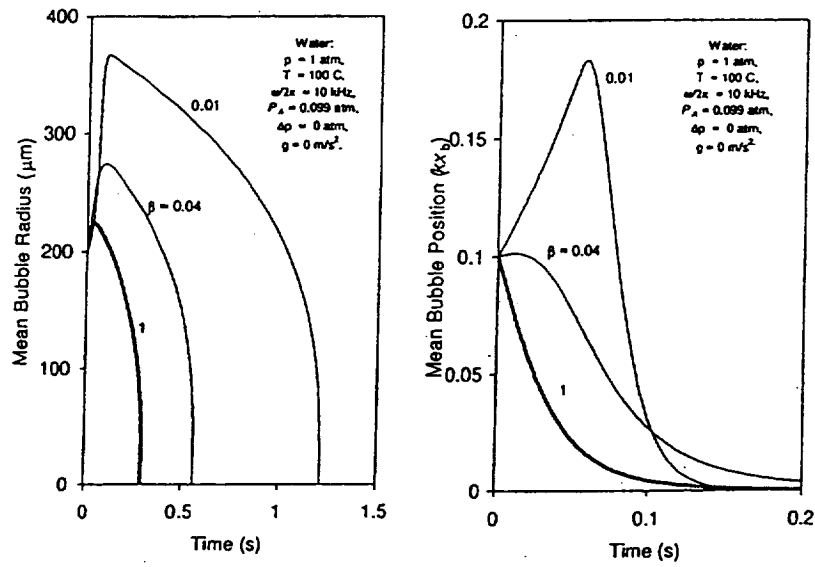


Figure IX-18: Dynamics of a vapor bubble in a standing acoustic wave at different values of the accommodation coefficient and zero gravity conditions.

Chapter X.

Conclusions

Our study conducted using analytical and numerical methods shows that the kinetics of phase transitions can affect the dynamics of vapor and vapor-gas bubbles over a broad range of frequencies and bubble sizes. For water at atmospheric pressure, the frequency range 1-100 kHz and the bubble size range $10\text{ }\mu\text{m}$ - 10 mm were investigated. During the study several important physical effects were uncovered, including

- Strong influence of the kinetics of phase transitions on the vapor temperature,
- Influence of the kinetics of phase transitions on the dynamics of vapor-gas bubbles with substantial inert gas content,
- Influence of the Soret-Dufour effect on bubble resonance oscillations,
- Memory-type thermal effects in the liquid during rectified heat transfer,
- Effects of slow bubble mean radius/position oscillation and stabilization in standing wave.

These effects can be exploited for proper design of experiments. Such experiments would be performed prior to finalizing the design of an instrument to investigate practical issues. We found that there exist optimal superheats, concentrations, frequencies, and mean bubble sizes which provide the highest sensitivity of the bubble dynamics to the value of the accommodation coefficient. This sensitivity can be substantially reduced in conditions that are far from optimal. The experimental setup should allow for variation and control of the liquid temperature and the pressure in the cell. It is also important to select appropriate methods of bubble generation and measurement of bubble size and position. Depending on the methods employed the optimal ranges of bubble sizes and acoustic frequencies can be determined for measurement of the accommodation coefficient. The characteristic acoustic frequency will determine the size of the setup (Helmholtz resonator for standing waves), which is also should influenced by the methods of bubble size and position measurement and bubble generation. The experimental design also account for variation in the optimal sensitivity of the bubble dynamics with the order of magnitude of the accommodation coefficient. If β is to be measured over a broad range of expected values (say 0.001-1 for water), then this range can be subdivided into several bands (say 0.001-0.01, 0.01-0.1, and 0.1-1). For each band, an optimal set of conditions can be found.

Bibliography

- [1] M. VOLMER, *Kinetik der Phasebildung*, Dresden-Leipzig: Steinkopff, 1939. (in German)
- [2] N.A. GUMEROV, Weakly non-linear oscillations of the radius of a vapour bubble in an acoustic field, *J. Appl. Maths Mechs*, **55**, 205-211, 1991.
- [3] V.A. AKULICHEV, Acoustic cavitation in cryogenic and boiling liquids. In: *L. van Wijngaarden (ed.) Mechanics and Physics of Bubbles in Liquids*, Martinus Nijhoff, the Netherlands, 1982.
- [4] N.A. GUMEROV, Determination of the accommodation coefficient using gas/vapor bubble dynamics in an acoustic field, *Proceedings of the 4th Microgravity Fluid Physics and Transport Phenomena Conference*, NASA LeRC, Cleveland, OH, 340-345, 1998.
- [5] N.A. GUMEROV, Dynamics of vapor bubbles with nonequilibrium phase transitions in isotropic acoustic fields, *Physics of Fluids*, **12**(1), 71-88, 2000.
- [6] N.A. GUMEROV, Rectified heat transfer to vapor bubbles in standing acoustic waves, *UEF Conference "Microgravity Fluid Physics and Heat Transfer"*, HI, USA, September 1999.
- [7] N.A. GUMEROV, Linear oscillations of vapor-gas bubbles with nonequilibrium phase transitions, *J. Acoust. Soc. Am.* (submitted February 2000).
- [8] K.C. HICKMAN, Maximum evaporation coefficient of water, *Chem. Engng Sci.*, **18**, 1442, 1954.
- [9] A.F. MILLS & R.A. SEBAN, The condensation coefficient of water, *Intl. J. Heat and Mass Transfer*, **37**, 1815-1827, 1967.
- [10] N. CHODES, J. WARNER & A. GAGIN, A determination of the condensation coefficient of water from the growth rate of small cloud droplets, *J. Atmospheric Sci.*, **31**, 1351-1357, 1974.
- [11] D.E. HAGEN, J. SCHMITT, M. TRUEBLOOD, J. CARSTENS, D.R. WHITE, AND D.J. ALOFS, Condensation coefficient measurement for water in the UMR cloud simulation chamber, *J. Atmospheric Sci.*, **46** (6), 803-816, 1989.
- [12] N.A. GUMEROV, A.I. IVANDAIEV & R.I. NIGMATULIN, Sound waves in monodisperse gas-particle or vapour-droplet mixtures, *J. Fluid Mech.*, **193**, 53-74, 1988.
- [13] R. DURAISWAMI & A. PROSPERETTI, Linear pressure waves in fogs, *J. Fluid Mech.*, **299**, 187-215, 1995.
- [14] N.A. GUMEROV, The weak non-linear fluctuations in the radius of a condensed drop in an acoustic field, *PMM U.S.S.R.*, **53** (2), 203-211, 1989.

- [15] V.V. KORNEEV, Possibility of determining the coefficient of condensation of water from experiments involving laser vaporization, *High Temperature*, **28** (3), 406, 1990.
- [16] G. PICKER & J. STRAUB, Interfacial mass transfer studies on vapor bubbles in microgravity, *UEF Conference "Microgravity Fluid Physics and Heat Transfer"*, HI, USA, September 1999.
- [17] V.A. AKULICHEV, V.N. ALEKSEEV & V.A. BULANOV, *Periodical Phase Transformations in Liquids*, Moscow: Nauka, 1986. (in Russian).
- [18] H. HERTZ, Über die Verdunstung der Flüssigkeiten, Insbesondere des Quecksilbers, im lufteren Raume, *Ann. Phys.* **17**, 177, 1882.
- [19] M. KNUDSEN, Maximum rate of vaporization of mercury, *Ann. Phys.*, **47**, 697, 1915.
- [20] T. ALTY & C.A. MACKAY, The accommodation and evaporation coefficient of water, *Proc.R. Soc.*, **A149**, 104, 1935.
- [21] U. NARASAWA & G.S. SPRINGER, Measurements of evaporation rates of water, *J. Colloid Interface Sci.*, **50**, 392-395, 1975.
- [22] R.C.A. BROWN, H.J. HILKE, AND A.H. ROGERS, Ultrasonic helium bubble chamber, *Nature*, **220** (5174), 1177-1178, 1968.
- [23] V.A. AKULICHEV, V.N. ALEKSEEV, AND K.A. NAUGOLNYKH, Dynamics of vapor bubbles in liquid-hydrogen ultrasonic bubble chambers, *Sov. Phys. Acoust.* **17**, 302-310, 1972.
- [24] R.D. FINCH, R. KAGIWADA, M. BARMATZ, AND I. RUDNICK, Cavitation in liquid helium, *Phys. Rev.*, **134**, A1425-A1428, 1964.
- [25] E.A. NEPPIRAS & R.D. FINCH, Acoustic cavitation in helium, nitrogen, and water at 10 kHz. *J. Acoust. Soc. Am.*, **52**, 335-343, 1972.
- [26] P.L. MARSTON, Tensile strength and visible ultrasonic cavitation in superfluid ^4He , *J. Low Temp. Phys.*, **25**, 383-407, 1976.
- [27] A. PROSPERETTI & H.N. OĞUZ, Acoustic behavior of vapor bubbles, *Proceedings of the 3rd Microgravity Fluid Physics Conference*, NASA LeRC, Cleveland, OH, 159-164, 1996.
- [28] V. HARIK, Y. HAO, H.N. OĞUZ, AND A. PROSPERETTI, Pressure-radiation forces on vapor bubbles, *Proceedings of the 4th Microgravity Fluid Physics and Transport Phenomena Conference*, NASA LeRC, Cleveland, OH, 484-489, 1998.
- [29] T. WANG, Effects of evaporation and diffusion on an oscillating bubble, *Phys. Fluids*, **17**, 1121-1126, 1974.
- [30] N.S. KHABEEV, Heat transfer and phase transition effects in the oscillation of vapor bubbles, *Sov. Phys. Acoust.*, **21**, 501-505, 1976.
- [31] M. FANELLI, A. PROSPERETTI & M. REALI, Radial oscillations of gas-vapor bubbles in liquids. Part I: Mathematical formulation, *Acustica*, **47**(4), 253-265, 1981.
- [32] R.D. FINCH & E.A. NEPPIRAS, Vapor bubble dynamics, *J. Acoust. Soc. Am.*, **53**, 1402-1410, 1973.
- [33] D.-Y. HSIEH, On oscillation of vapor bubbles, *J. Acoust. Soc. Am.*, **66**, 1514-1515, 1979.

- [34] P.L. MARSTON, Evaporation-condensation resonance frequency of oscillating vapor bubbles, *J. Acoust. Soc. Am.*, **66**, 1516-1521, 1979.
- [35] Y. HAO & A. PROSPERETTI, The dynamics of vapor bubbles in acoustic pressure fields, *Physics of Fluids*, **11**(8), 2008-2019, 1999.
- [36] T.G. WANG, Rectified heat transfer, *J. Acoust. Soc. Am.*, **56**, 1131-1143, 1974.
- [37] V.N. ALEKSEEV, Nonsteady behavior of a vapor bubble in an ultrasonic field, *Sov. Phys. Acoust.*, **22**, 104-107, 1976.
- [38] V.A. AKULICHEV, V.N. ALEKSEEV, AND V.P. YUSHIN, Growth of vapor bubbles in an ultrasonic field, *Sov. Phys. Acoust.*, **25**, 453-457, 1979.
- [39] G.M. PATEL, R.E. NICHOLAS, AND R.D. FINCH, Rectified heat transfer in vapor bubbles, *J. Acoust. Soc. Am.*, **78**, 2122-2131, 1985.
- [40] P.L. MARSTON & D.B. GREENE, Stable microscopic bubbles in helium-I and evaporation-condensation resonance, *J. Acoust. Soc. Am.*, **64**, 319-321, 1978.
- [41] N.A. GUMEROV, The heat and mass transfer of a vapor bubble with translatory motion at high Nusselt numbers, *Int. J. Multiphase Flow.*, **22** (2), 259-272, 1996.
- [42] D. LEGENDRE, J. BOREE & J. MAGNAUDET, Thermal and dynamic evolution of a spherical bubble moving steadily in a superheated or subcooled liquid, *Fluid Physics*, **10** (6), 1256-1272, 1998.
- [43] G.L. CHAHINE & H.L. LIU, Theory of the growth of a bubble cluster in a superheated liquid, *J. Fluid Mech.* **156**, 257-279, 1985.
- [44] K. OHSAKA & E.H. TRINH, A two-frequency acoustic technique for bubble resonant oscillation studies, *J. Acoust. Soc. Am.* **107**(3), 1346-1351, 2000.
- [45] Z.C. FENG & L.G. LEAL, Bifurcation and chaos in shape and volume oscillations of a periodically driven bubble with two-to-one internal resonance, *J. Fluid Mech.*, **266**, 209-242, 1994.
- [46] N.A. GUMEROV, Effect of acoustic radiation on the stability of spherical bubble oscillations, *Physics of Fluids*, **10**(7), 1767-1768, 1998.
- [47] Y. HAO & A. PROSPERETTI, The effect of viscosity on the spherical stability of oscillating gas bubbles, *Physics of Fluids*, **11**(6), 1309-1317, 1999.
- [48] E.H. TRINH, D.B. THIESSEN, AND R.G. HOLT, Driven and freely decaying nonlinear shape oscillations of drops and bubbles immersed in a liquid: experimental results, *J. Fluid Mech.*, **364**, 253-272, 1998.
- [49] D.V. LYUBIMOV, A.A. CHEREPANOV, T.P. LYUBIMOVA & B. ROUX, Deformation of gas or drop inclusion in high frequency vibrational field, *Microgravity Quarterly*, **6**(2-3), 69-73, 1996.
- [50] D.V. LYUBIMOV, A.A. CHEREPANOV, T.P. LYUBIMOVA, D. BEYSENS, B. ROUX & S. MERADJI, Behavior of isolated bubble (or drop) in oscillating liquid, *Proceedings of the 3rd International Conference on Multiphase Flow*, Lyon, France, June 1998.

- [51] L.A. CRUM, Bjerknes forces on bubbles in a stationary sound field, *J. Acoust. Soc. Am.*, **57**, 1363-1370, 1975.
- [52] J.S. SITTER, T.J. SNYDER, J.N. CHUNG, AND P.L. MARSTON, Acoustic field interaction with a boiling system under terrestrial gravity and microgravity, *J. Acoust. Soc. Am.*, **104**, 2561-2569, 1998.
- [53] T.J. ASAKI, P.L. MARSTON, AND E.H. TRINH, Shape oscillations of bubbles in water driven by modulated ultrasonic radiation pressure: Observations and detection with scattered laser light, *J. Acoust. Soc. Am.*, **93**, 706-713, 1993.
- [54] I. AKHATOV, R. METTIN, C.D. OHL, U. PARLITZ, AND W. LAUTERBORN, Bjerknes force threshold for stable single bubble sonoluminescence, *Physical Rev. E*, **55**, 3747-3750, 1997.
- [55] R.G. HOLT & L.A. CRUM, Acoustically forced oscillations of air-bubbles in water: Experimental results, *J. Acoust. Soc. Am.*, **91**, 1924-1932, 1992.
- [56] L.D. LANDAU & E.M. LIFSHITZ, *Fluid Mechanics*, Pergamon Press, New-York, 1986.
- [57] A. PROSPERETTI, The thermal behaviour of oscillating gas bubbles, *J. Fluid Mech.* **222**, 587-616, 1991.
- [58] L.I. SEDOV, *Mechanics of Continuous Media*, Nauka, Moscow, 1976.
- [59] R.I. NIGMATULIN, *Dynamics of Multiphase Media*, Vol. 1., Hemisphere, Washington, 1991.
- [60] S. SOCHARD, A.M. WILHELM, AND H. DELMAS, Bubble dynamics in an acoustic pressure field including gas-vapour interdiffusion, phase changes and Van der Waals equation, *Proceedings of the 3rd International Conference on Multiphase Flow, ICMF'98*, Lyon, France, 1998.
- [61] R.H. PERRY, D.W. GREEN, AND J.O. MALONEY (EDS.), *Perry's Chemical Engineers' Handbook*. 6th ed., p. 17-69, McGraw-Hill, New York, 1984.
- [62] S. CHAPMAN & T.G. COWLING, *The Mathematical Theory of Non-Uniform Gases*, Cambridge University Press, Cambridge, 1970.
- [63] R.I. NIGMATULIN & N.S. KHABEEV, Heat exchange between a gas bubble and a liquid, *Fluid Dyn.* **9**, 759-764, 1974.
- [64] M.M. FYRILLAS & A.J. SZERI, Dissolution or growth of soluble spherical oscillating bubbles, *J. Fluid Mech.*, **277**, 381-407, 1994.
- [65] F.B. NAGIEV & N.S. KHABEEV, Heat-transfer and phase-transition effects associated with oscillations of vapor-gas bubbles, *Sov. Phys. Acoust.*, **25**(2), 148-152, 1979.
- [66] R.I. NIGMATULIN, N.S. KHABEEV, AND F.B. NAGIEV, Dynamics, heat and mass transfer of vapour-gas bubbles in a liquid, *Int. J. Heat Mass Transfer*, **24**(6), 1033-1044, 1981.
- [67] L.G. TKACHEV & V.D. SHESTAKOV, Effect of an ultrasonic field on the behaviour of a vapor bubble in liquid hydrogen, *Sov. Phys. Acoust.* **18**, 362-368, 1972.
- [68] I. AKHATOV, U. PARLITZ, AND W. LAUTERBORN, Pattern formation in acoustic cavitation. *J. Acoust. Soc. Am.*, **96**, 3627-3635, 1994.

- [69] N.A. GUMEROV, On waves of the self-induced acoustic transparency in mixtures of liquid and vapor bubbles. *S. Morioka & L. van Wijngaarden (eds.), IUTAM Symposium on Waves in Liquid/Gas and Liquid/Vapour Two-Phase Systems*, Kluwer, the Netherlands, 77-86, 1995.
- [70] N.A. GUMEROV, On self-organization of voids in acoustic cavitation. *Proceedings of the 3rd International Conference on Multiphase Flow, ICMF'98*, Lyon, France, 1998.
- [71] W.H. PRESS, S.A. TEUKOLSKY, W.T. VETTERLING, AND B.P. FLANNERY, *Numerical Recipes in FORTRAN: the Art of Scientific Computing*, 2nd ed. Cambridge University Press, Cambridge, 1992.

REPORT DOCUMENTATION PAGE			Form Approved OMB No. 0704-0188	
Public reporting burden for this collection of information is estimated to average 1 hour per response, including the time for reviewing instructions, searching existing data sources, gathering and maintaining the data needed, and completing and reviewing the collection of information. Send comments regarding this burden estimate or any other aspect of this collection of information, including suggestions for reducing this burden, to Washington Headquarters Services, Directorate for Information Operations and Reports, 1215 Jefferson Davis Highway, Suite 1204, Arlington, VA 22202-4302, and to the Office of Management and Budget, Paperwork Reduction Project (0704-0188), Washington, DC 20503.				
1. AGENCY USE ONLY (Leave blank)		2. REPORT DATE January 2001		3. REPORT TYPE AND DATES COVERED Final Contractor Report
4. TITLE AND SUBTITLE Determination of the Accommodation Coefficient Using Vapor/Gas Bubble Dynamics in an Acoustic Field			5. FUNDING NUMBERS WU-101-13-0A-00 NAS3-98094	
6. AUTHOR(S) Nail A. Gumerov, Chao-Tsung Hsiao, and Alexei G. Goumilevski				
7. PERFORMING ORGANIZATION NAME(S) AND ADDRESS(ES) DYNAFLOW, Inc. 7210 Pindell School Road Fulton, Maryland 20759			8. PERFORMING ORGANIZATION REPORT NUMBER E-12538	
9. SPONSORING/MONITORING AGENCY NAME(S) AND ADDRESS(ES) National Aeronautics and Space Administration Washington, DC 20546-0001			10. SPONSORING/MONITORING AGENCY REPORT NUMBER NASA CR-2001-210572 Technical Report 98001	
11. SUPPLEMENTARY NOTES Project Manager, Dr. Fran Chiaramonte, Microgravity Science Division, NASA Glenn Research Center, organization code 6712, 216-433-8040; and Technical Monitor, Jeff Allen, Microgravity Science Division, NASA Glenn Research Center, organization code 6712, 216-433-3087.				
12a. DISTRIBUTION/AVAILABILITY STATEMENT Unclassified - Unlimited Subject Categories: 34, 77, and 64 Available electronically at http://gltrs.grc.nasa.gov/GLTRS This publication is available from the NASA Center for AeroSpace Information, 301-621-0390.			12b. DISTRIBUTION CODE	
13. ABSTRACT (Maximum 200 words) Nonequilibrium liquid/vapor phase transformations can occur in superheated or subcooled liquids in fast processes such as in evaporation in a vacuum. The rate at which such a phase transformation occurs depends on the "condensation" or "accommodation" coefficient, β , which is a property of the interface. Existing measurement techniques for β are complex and expensive. The development of a relatively inexpensive and reliable technique for measurement of β for a wide range of substances and temperatures is of great practical importance. The dynamics of a bubble in an acoustic field strongly depends on the value of β . It is known that near the saturation temperature, small vapor bubbles grow under the action of an acoustic field due to "rectified heat transfer." This finding can be used as the basis for an effective measurement technique of β . We developed a theory of vapor bubble behavior in an isotropic acoustic wave and in a plane standing acoustic wave. A numerical code was developed which enables simulation of a variety of experimental situations and accurately takes into account slowly evolving temperature. A parametric study showed that the measurement of β can be made over a broad range of frequencies and bubble sizes. We found several interesting regimes and conditions which can be efficiently used for measurements of β . Measurements of β can be performed in both reduced and normal gravity environments.				
14. SUBJECT TERMS Accommodation coefficient; Acoustic exciting bubbles; Vapor pressure; Microgravity; Liquid-vapor interface			15. NUMBER OF PAGES 123	
			16. PRICE CODE A06	
17. SECURITY CLASSIFICATION OF REPORT Unclassified	18. SECURITY CLASSIFICATION OF THIS PAGE Unclassified	19. SECURITY CLASSIFICATION OF ABSTRACT Unclassified	20. LIMITATION OF ABSTRACT	

